# Indirect measurement of reactor fuel temperature

by

Elbrecht Oswald

Thesis presented in partial fulfilment of the requirements for the degree Master of Science in Mechanical and Mechatronic Engineering at the University of Stellenbosch
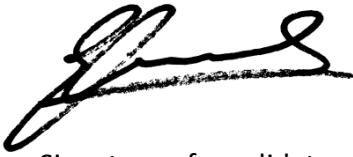
Supervisor: R. T. Dobson

Department of Mechanical and Mechatronic Engineering

University of Stellenbosch

South Africa

Pectora roborant cultus recti
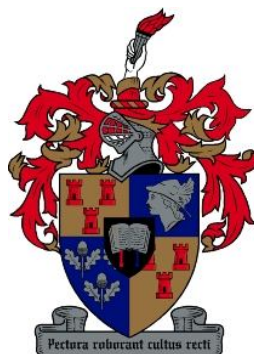
March 2010

Declaration

I, Elbrecht Oswald, hereby declare that the work contained in this thesis is my own original work and has not previously, in its entirety or in part, been submitted at any university for a degree. It is being submitted for the degree Master of Science in Mechanical and Mechatronic Engineering at the University of Stellenbosch.

Signature of candidate

Signed on 10 December 2009

Abstract

Regulators and designers of nuclear reactors regard knowledge of the pebble fuel temperature as important, due to the role that it plays in maintaining structural integrity and the production of neutrons. By using special fuel assemblies fitted with measuring equipment it is possible to measure the fuel temperature in stationary fuel reactors. This, however, is not possible in the pebble bed modular reactor due to its dynamic core. Designers of the pebble bed modular reactor have reserved special inspection channel borings inside the center reflector for fuel temperature measurement. By means of optical fibers and interferometry, the temperature can be measured inside such a channel. Currently the only way to control the fuel surface and core temperature is by measuring the gas inlet and outlet temperatures.

This thesis attempts to determine the pebble temperature by measuring the temperature in a reflector channel. This is done by constructing an electrically heated pebble bed experimental setup simulating a cutout section of a pebble bed modular reactor core. An additional computational fluid dynamics simulation of the experimental setup was also performed. This thesis also attempts to determine if there is a measureable temperature peak that can indicate where a pebble was in contact with the reflector surface. This could then be used in future studies to determine the pebble fuel velocity as it moves down the reactor core.

The computational fluid dynamics results were validated by experimental measurements. In the computational fluid dynamics model and experimental setup, it was found that there was indeed a measureable temperature difference on the temperature gradient along the reflector wall. The heat being conducted away from the pebble through the contact area can explain this. These differences were only observed when the channel was moved closer to the

pebbles and it is therefore advised that some redesigning of the channel should be done if the in-core temperature is to be accurately interpreted by the designers at PBMR (Pty) Ltd.

Opsomming

Reguleerders en ontwerpers van kern reaktore beskou die kennis van die korrel brandstof temperatuur as belangrik. Dit is weens die rol wat die brandstof temperatuur speel met die behoud van strukturele integriteit en die produksie van neutrone binne-in die reaktor. Met behulp van spesiale brandstof montasies toegerus met die meetings instrumentasie, is dit moontlik om die brandstof temperatuur in stilstaande brandstof reaktore te meet. Dit is egter nie moontlik in die korrel bed modulêre reaktor nie, as gevolg van sy dinamiese kern. Ontwerpers van die korrel bed modulêre reaktor het spesiale kanale in die binnekant van die middel reflektor vir brandstof temperatuur meeting gereseveer. Deur middel van optiese vesel en interferometrie, kan die temperatuur binne so 'n kanaal gemeet word. Tans is die enigste manier om die brandstof-oppervlak temperatuur te berekern, net moontlik deur gebruik te maak van die gemete gas inlaat-en uitlaat temperature van die reaktor.

Hierdie tesis poog om vas te stel of die korrel brandstof temperatuur deur die meet van die oppervlak temperatuur in 'n reflektor-kanaal bepaal kan word. Dit word gedoen deur 'n elektriese verhitte korrel bed eksperimentele opstelling te bou wat 'n gedeelte van 'n korrel bed modulêre reaktor simuleer. 'n Bykomende numeriese simulasie van die eksperimentele opstelling was ook uitgevoer. Hierdie werk het ook probeer om vas te stel of daar 'n meetbare temperatuur piek op die temperatuur profiel aandui kan word waar 'n korrel in kontak is met die reflektor se oppervlak. Dit kan dan in toekomstige studies gebruik word om te bepaal wat die korrel brandstof spoed was soos dit in die reaktor beweeg.

Die numerise simulasie uitslae was deur eksperimentele metings bevestig. In die numerise simulasie model en die eksperimentele opstelling, is daar gevind dat daar inderdaad 'n meetbare temperatuur verskil op die temperatuurgradiënt teen die reflektor oppervlak is. Dit kan verduidelik word as gevolg van die hitte

wat weg van die korrel gelei word deur middel van die kontak area. Hierdie verskille was slegs waargeneem wanneer die kanaal nader aan die korrels geskuif is en dit word as n aanbeveling aan PBMR (Pty) Ltd gemaak om sommige herontwerpe aan die kanaal te doen indien die in-kerntemperatuur gemeet wil word en akkuraat geinterpreteer wil word.

Acknowledgements

I would like to express my sincere gratitude towards the following people who contributed to making this study a success.

Table of contents

List of figures

List of tables

Nomenclature

General nomenclature

a Specific surface area, m^{-1}

A Area, m^2

A Ampere, A

C Coefficient of discharge

C_p Specific heat at constant pressure, $J/kg \cdot {}^{o}C$

C_v Specific heat at constant volume, $J/kg \cdot {}^{o}C$

d Diameter, m

d Differential

E Energy, J

$\dot{E}$ Electrical power, W

F Force, N

H Height, m

h_c Contact coefficient, W/m^2

i Internal energy, J

I Intensity of radiation

I_b Blackbody intensity (Planck function)

k Spring stiffness, N/m

k Thermal conductivity, $W/m {}^{o}C$

k Turbulent frequency, rad/s

L Length, m

L_g Void space thickness, m

$\dot{m}$ Mass flow rate, kg/s

M Moment, N/m

$\hat{\mathbf{n}}$ Unit surface normal

P	Pressure, Pa
P	Distance between two points, m
P_k	Rate of production of turbulent kinetic energy, J/kg
$\dot{Q}$	Heat transfer rate, W
q	Heat flux, W/m^2
$\mathbf{r}$	Position vector, m
R	Radius, m
R	Gas constant, J/kg $\cdot$ $^\circ$C
s	Geometric path length, m
$\hat{\mathbf{s}}$	Unit vector into a given direction
S	Source function
t	Time, s
T	Temperature, $^\circ$C or K
u	Velocity in x-direction, m/s
v	Velocity in y-direction, m/s
V	Velocity, m/s
V	Volt, V
w	Velocity in z-direction
w_i	Quadrature weights
x	Distance, m
Y	Approach velocity factor

Greek symbols

α	Thermal diffusivity, m^2/s
α	Absorptivity
β	Line overlap parameter
δ	Distance, m

δ_{ij}	Kronecker delta
ε	Void fraction of total volume
ε	Emissivity
ε	Rate of viscous dissipation of turbulence kinetic energy, J/kg
κ	Absorptivity coefficient
μ	Dynamic viscosity, kg/ms
μ_t	Eddy viscosity, Pa/s
v	Kinematic viscosity, m^2/s
ρ	Density, kg/m^3
ρ	Geographical latitude, degrees
ρ	Reflectivity
σ_s	Scattering coefficient
τ	Shear stress, N/m^2
ϕ	Expansion factor
ϕ	General variable
Φ	Dissipation function
Φ	Scattering phase function, sr^{-1}
Γ	Diffusion coefficient
ω	Turbulent frequency, s^{-1}
Ω	Solid angle, sr

Dimensionless groups

Re	Reynolds number, $\rho VL/\mu$
Pr	Prandtl number, $\mu C_p/k$

Subscripts

atm	Atmosphere
b	Blackbody

c   Cross-section

c   Contact

CFD   Computational fluid dynamics

ch   Channel

e   Electricity

exp   Experiment

f   Fluid

g   Gas

g   Gap

H   Height

Hg   Mercury

i   Incoming or dummy counter

in   Into

loss   Loss to the environment

Ms   Mercury station

n   Nozzle

out   Out off

p   Particle

peb   Pebble

ss   Stainless steel

t   Temperature

tus   In between

v   Void

w   Wall

Superscripts

'   Directional values

^   Unit vector

Abbreviations

AVR	Arbeitsgemeinschaft Versuchsreaktor
ABB	A SEA Brown Boveri
BCC	Body Centered Cubic
BSM	Hottinger Baldwin Messtechnik
CFD	Computational Fluid Dynamics
DES	Detached-Eddy Simulation
DO	Discrete Ordinates
FCC	Face Centered Cubic
GEN	Generator
HPC	High-pressure Compressor
HPTU	High Pressure Test Unit
HTR	High Temperature Reactor
HV	High Voltage
ICS	Inventory Control System
LES	Large Eddy Simulation
LEU-TRISO	Low-Enriched Uranium Triple Coated Isotropic
LP	Low pressure
LPC	Low-pressure Compressor
NWU	North-West University
PBMR	Pebble Bed Modular Reactor
PT	Power Turbine
RANS	Reynolds-Average Navier-Stokes
RPM	Revolutions Per Minute
SAS	Small Absorber Spheres
SC	Simple Cubic
SSR	Solid State Relay
SST	Shear Stress Turbulence

THTR   Thorium High Temperature Reactor

URANS   Unsteady Reynolds-Average Navier-Stokes

USB   Universal Serial Bus

1. Introduction

This chapter provides the necessary information to inform the reader about nuclear pebble bed reactors and their origins. The aim of this thesis will also be outlined and discussed along with a summary of relevant work done by other researchers. Thereafter a description of the next chapters will give more insight into the rest of this thesis.

1.1. Background

The Pebble Bed Modular Reactor (PBMR) is based on the design developed as part of an extensive High Temperature Reactor (HTR) programme in Germany. The Germans researched HTR's, and built a 15 MWe (40 MWt) AVR (Arbeitsgemeinschaft Versuchsreaktor, German) research reactor at the nuclear research center in Jülich (The pebble bed evolution, 2007). It was planned, constructed, and operated as a reactor experiment on an industrial scale. Originally, a German contribution, it was intended to furnish the development of economic nuclear power based on first-of-a-kind technology. The reactor was operational from 1966 to 1988; thereafter it was decommissioned due to political considerations and because it had fulfilled all planned research experiments.

Design changes made to the AVR resulting from operating experience, were incorporated in the design of the 300 MWe (750 MWt) Thorium High Temperature Reactor (THTR). The THTR, also a German contribution, operated during 1985 and 1988. The THTR was a first-of-a-kind production plant intended to demonstrate the viability of a different subsystem hardware design, with specific emphasis on plant availability and maintainability. To this end, the design concentrated on building a plant with a life expectancy of 40 years and a power generation availability of 80 to 90 percent (The pebble bed evolution, 2007).

Based on the experience gained from the AVR and THTR, two German-based groups further developed pebble bed reactor designs. These designs ranged from high power reactors, mainly developed by ABB (previously A SEA Brown Boveri), to the modular inherently safe Module design of Siemens/Interatom. These two groups later combined to form Hochtemperatur Reaktorbau GmbH.

In 1999, Eskom obtained the right to access the HTR engineering database that includes details of the Siemens/Interatom HTR-Module design. This design can be regarded as the forerunner of the South African PBMR concept. The PBMR core design was made using the same design philosophy that was incorporated in the design of the HTR-Module.

Many components used in the fuel handling and control systems of the PBMR are copies of those used in the THTR programme. They include all the improvements made over the years, thus saving costly development work. The PBMR concept also includes the technological advances made in gas turbine technology since the 1980's. The small plant size and the elimination of a steam cycle both contribute to the achievement of a plant configuration with a very robust safety case.

The PBMR is a helium-cooled, graphite-moderated HTR. It has a 27 m high vertical steel reactor pressure vessel with an inner diameter of 6.2 m. The reactor pressure vessel contains and supports a metallic core barrel. The core barrel, in turn, supports the annular pebble fuel core, which is located in the space between the central and outer graphite reflectors. Vertical borings in these reflectors are provided for the reactivity control elements and measurement instrumentation. Figure 1-1 shows the complete main power system layout.
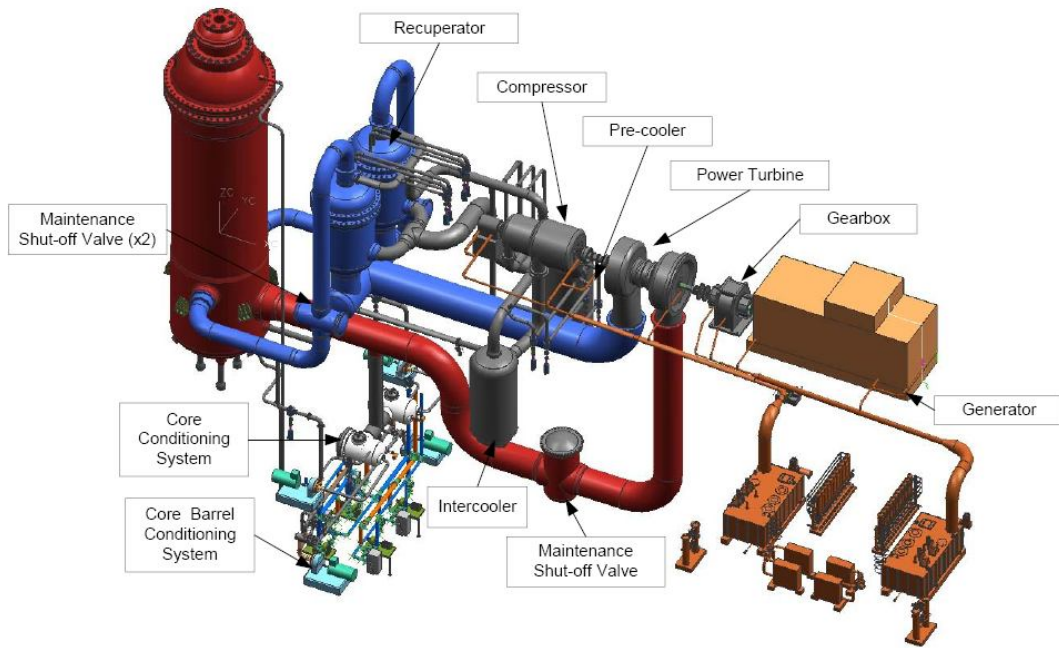
Figure 1-1: Main PBMR power system layout (Slabber *et al.*, 2006)

The PBMR uses fuel pebbles to generate heat energy by means of nuclear fission. Helium is used as the coolant and energy transfer medium, to drive a closed cycle gas turbine-compressor and generator system. When fully loaded the core would contain approximately 450000 fuel pebbles.

The thermodynamic cycle used is a Brayton cycle with a water-cooled pre-cooler and inter-cooler. A highly efficient recuperator is used after the power turbine. The helium, cooled in the recuperator, passes through the pre-cooler, low-pressure compressor, the inter-cooler and high-pressure compressor before being returned to the reactor core.

The energy gained by the helium in the core and the power generated by the power turbine is proportional to the helium mass flow rate for the same temperatures in the system. The total mass of helium in the system depends on the pressure. Thus, the power is adjusted by changing the helium pressure in the system. Figure 1-2 shows the flow diagram of the power conversion unit.
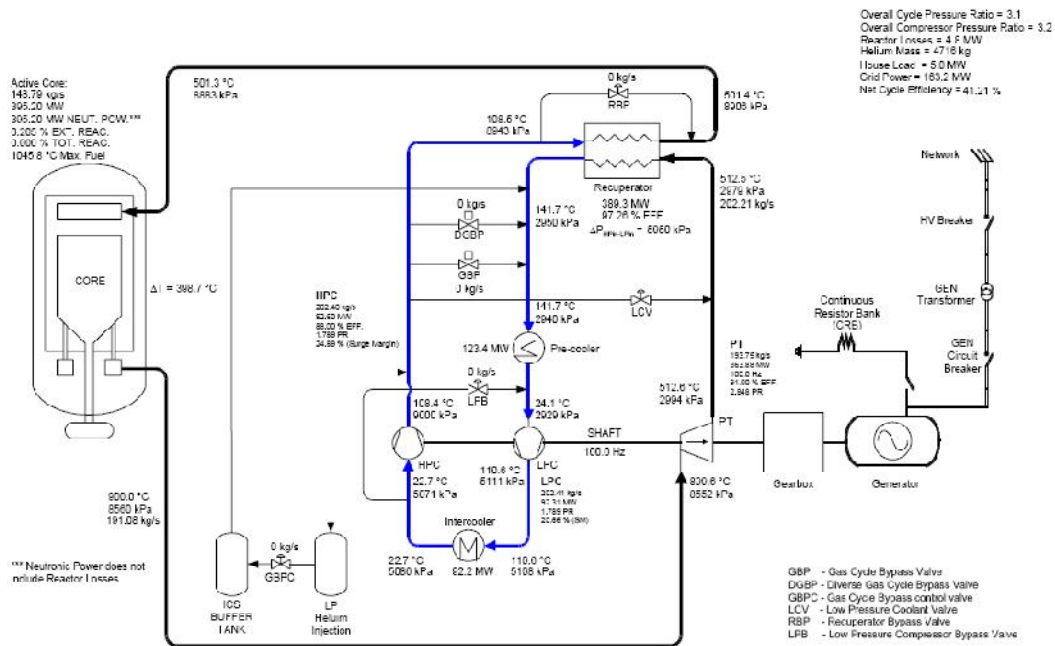
Figure 1-2: Flow diagram of the power conversion unit (Slabber *et al.*, 2006)

The high pressure and high temperature operation of the reactor results in a relativly high thermal efficiency. While a typical light water reactor has a thermal efficiency (electrical power output/thermal heat input) of approximately 33 %, an efficiency of about 41 % is anticipated in the basic PBMR design (How the PBMR works, 2007). A unique ability of this type of reactor is that at a specific core temperature, the whole cycle becomes self-sustaining (How the PBMR works, 2007).

Graphite is used for the two reflectors and other core structures. A central reflector column is located in the centre of the core and an outer reflector on the outside of the core. The fuel core is the annulus between the outer and central reflectors. Figure 1-3 is a cut-away view of the reactor pressure vessel, showing the core structures, outer and central reflectors.
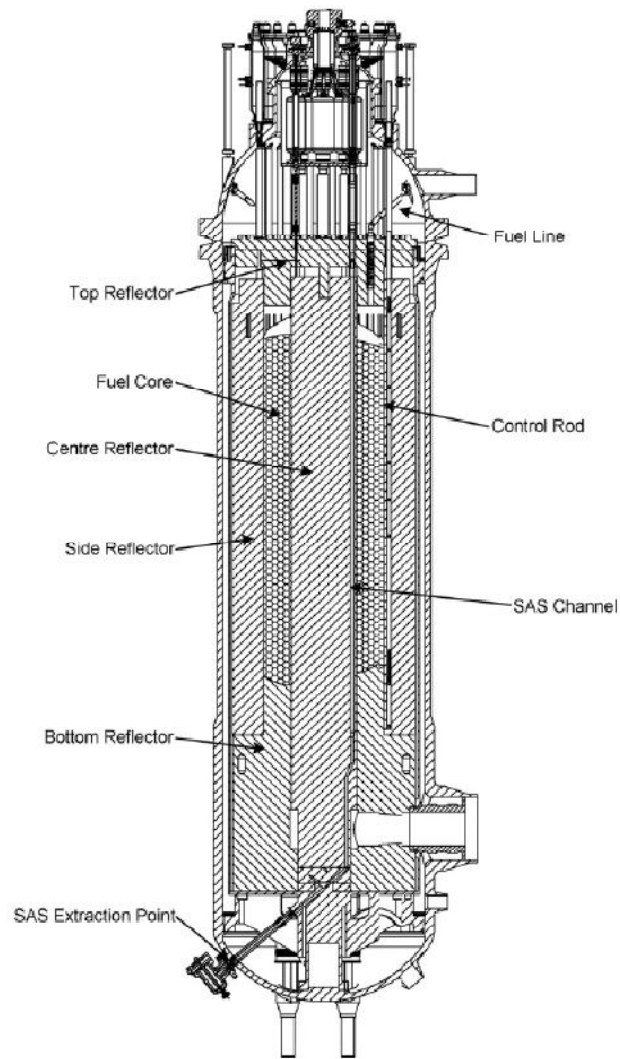
Figure 1-3: Vertical cross-section of the reactor pressure vessel (Mitchell and Polson, 2007)

The central reflector is the only component allowing access for measuring the reactor fuel temperature. Figure 1-4 shows a section through the central reflector. The inspection channels will be used for temperature measurements and other measurement and instrumentation devices.
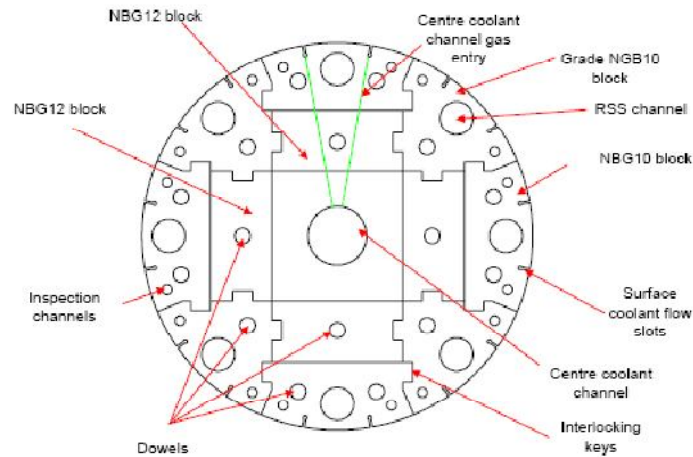
Figure 1-4: Section through center reflector (Slabber *et al.*, 2006)

PBMR fuel is based on a proven, high-quality German fuel design consisting of low enriched uranium triple coated isotropic (LEU-TRISO) particles contained in a moulded graphite pebble. A coated particle consists of a kernel of uranium dioxide surrounded by four coating layers as shown in figure 1-5.
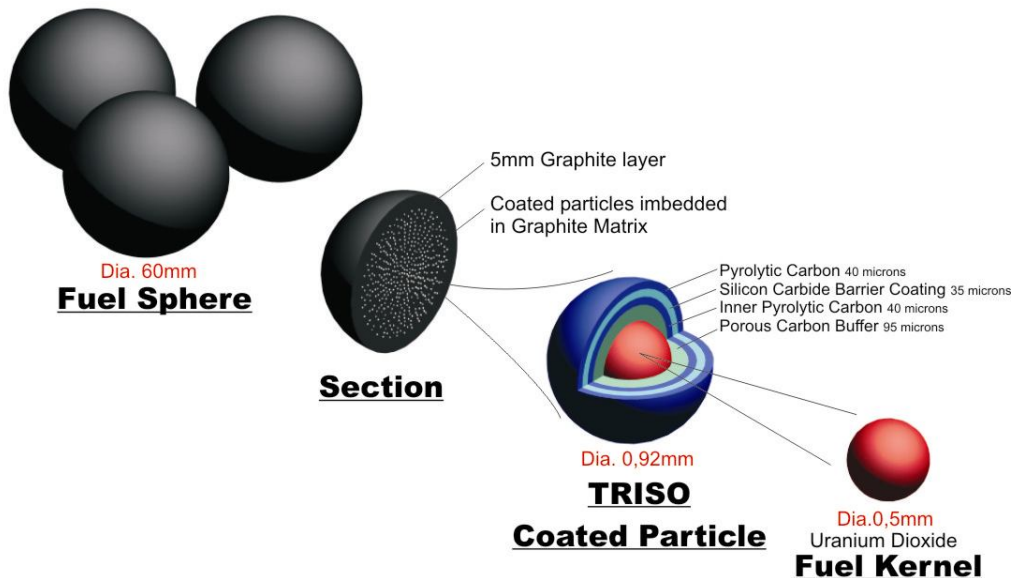
Figure 1-5: PBMR Fuel pebble design (Slabber *et al.*, 2006)

In the fabrication process, a solution of uranyl nitrate is dropped from small nozzles to form microspheres. The microspheres are then gelled and calcined to produce uranium oxide fuel kernels. The kernels are then passed through a chemical vapour deposition furnace in an argon environment at a temperature of 1000 °C. In this process of chemical vapour deposition, the coating layers are added with extreme precision.

For the PBMR fuel, the first layer deposited on the kernels is porous carbon. This is followed by a thin coating of pyrolytic carbon, a layer of silicon carbide, and finally another layer of pyrolytic carbon. The porous carbon accommodates any deformation that the uranium dioxide kernel may undergo during the lifetime of the fuel. This buffer layer also accommodates any gaseous fission products that may diffuse out of the kernel. The silicon carbide layer provides an impenetrable barrier designed to contain the fuel and fission products.

Roughly 15000 of these coated particles, about a millimeter in diameter, are mixed with graphite powder and phenolic resin. This mixture of kernels and graphite powder is then pressed in a 50 mm diameter pebble. A 5 mm thick layer of pure graphite is then added to form a non-fuel zone. The completed pebble is then machined to a uniform diameter of 60 mm, after which it is sintered at 1950 °C and annealed (Slabber *et al.*, 2006).

Each fuel pebble contains about 9 g of uranium, and the total mass of a fuel pebble is 210 g. The total uranium in one fuel load is 4.1 metric tons. A complete list of the fuel pebble characteristics is listed in table 1-1.

Table 1-1: Nominal characteristics for PBMR fuel pebbles (Slabber *et al.*, 2006)

Characteristics	Value	Unit
Fuel Spheres:		
Geometry	Spherical	-
Fuel Sphere Diameter	60	mm
Fuel Region Diameter	50	mm
Fuel-free Region Thickness	5	mm
Heavy Metal Loading	9	g/Fuel Sphere
Uranium Enrichment	9.6 (equilibrium core)	% U^{235}
Coated Particle:		
Kernel Diameter	500	μm
Buffer Layer Thickness	95	μm
Inner Low Temperature Isotropic Layer Thickness	40	μm
SiC Layer Thickness	35	μm
Outer Low Temperature Isotropic Layer Thickness	40	μm

Each pebble passes through the reactor in about 126 days and recycles six times. The pebbles last about three years before they are spent. This means that the reactor will use 15 total fuel loads in its design lifetime of 40 years.

1.2.   Objectives

Regulators and designers of nuclear reactors regard the fuel temperature as an important parameter. By using special fuel assemblies fitted with measuring equipment it is possible to measure the fuel temperature in stationary fuel reactors. This, however, is not possible in the pebble bed reactor due to its dynamic core. Designers of the pebble bed reactor have reserved special inspection channel borings inside the center reflector for fuel temperature measurement. By means of optical fibers and interferometry, the temperature can be determined through dedicated sensor slots or images be obtained through look through apertures inside the channels (Lalk, 2007).

After measuring the temperature profile along the inspection channel, it can then be analyzed and possibly provide the following information:

o The fuel surface, central and maximum temperature.

o The rate of fuel movement through the core.

o The fuel temperature history after any loss of forced cooling (Lalk, 2007).

Currently the only way the fuel surface temperature is calculated, is by measuring the gas inlet and outlet temperature. The fuel temperature determines the fuel element power production, the heat transfer path and properties of the element (Slabber, 2004).

Knowing the exact fuel temperature throughout the core of the reactor will allow for more efficient operation. Fuel can also then run to a closer tolerance to its maximum fuel temperature. It is calculated that with every increase of 50 °C reactor outlet temperature, the efficiency gain in the power conversion unit increases by 1.5 % (Slabber, 2004). Hence, knowing the fuel temperature is critical in improving efficiency while not compromising safety.

The objective of this project is to determine the pebble fuel temperature in contact with the reflector wall using distributed temperature measures inside an inspection channel. In order to achieve this, an electrically heated pebble bed, which resembles a cutout of the central reflector and fuel pebbles will be designed and built. By measuring the pebble temperature in contact with the reflector wall and distributed temperatures inside the inspection channel experimental results was gathered. These experimental results can then be compared to a computational fluid dynamic (CFD) model.

Another objective is to determine if there is a measurable peak in temperature on the temperature profile along the inspection channel caused by the pebble in contact with the reflector surface. If the peak in temperature is measureable

where a pebble is in contact with the reflector wall, it will indicate its position. Therefore, when a pebble's position is allocated it can be monitored over time and thus the distance travelled along with the average velocity can be calculated.

The purpose of the CFD model is to predict the pebble temperatures and temperature profile that would be measured in the inspection channel. To validate the CFD model, temperatures of the fuel pebbles in contact with the reflector wall and temperatures in the inspection channel at various locations will be compared to the experimental measurements.

Once the CFD model verifies the pebble temperatures in the experimental setup, it can be used to test various other thermal conditions and other packing structures. This can therefore improve the validity of the model before being implemented in PBMR simulations. Improvents in the pebble bed simulations that can calculate the pebble temperature throughout the core will improve efficiency and safety.

Practicing safety and enforcing it is an underlying objective of this thesis, as safety measures are incorporated in the design of experiments. This is of critical importance, as experiments will be conducted in atmospheric conditions with materials that could start exothermic reactions due to the presence of oxygen.

1.3.   Literature study

Lee *et al*. (2007) numerically investigated the inter-pebble flow regions of a packed pebble bed. Their studies concluded that the flow regimes and their relevant flow-induced local heat transfer were significantly dependent on the modelling of the inter-pebble region. A sensitivity analysis was conducted where the inter-pebble region was approximated by gaps (2 mm and 1 mm), a point contact, and an area contact (contact diameter 2 mm). The cases of contact showed numerous differences in the results of the flow regime around the

pebbles, as well as in the wake, compared to the cases of the inter-pebble gap. However, they found that there were no large differences regarding flow between the point contact and the area contact.

Bahrami *et al.* (2006) modeled the thermal conductivity of spherical packed beds that included two main analyses, conduction between rough spheres and heat transfer through the interstitial stagnant gas between the solids. Their model accounts for the thermophysical properties of spheres and the gas, load, the rarefaction effects of the interstitial gas, gas temperature and pressure, and sphere diameter, roughness and asperity slope. Different sphere diameters were tested and included 50.4 mm, which is close to the PBMR pebble diameter. Their models were bounded by (Tien and Vafai, 1979) that showed that the face centered cubic (FCC) and simple cubic (SC) packings present upper and lower bounds for the effective thermal conductivity of randomly packed beds filled with a single phase fluid.

Constantinescu *et al.* (2003) numerically simulated the subcritical flow over a sphere. Their aim was to compare the predictions of some of the main physics and flow parameters from solutions of the unsteady Reynolds-averaged Navier-Stokes (URANS) equations, large eddy simulation (LES) and detached-eddy simulation (DES). URANS predictions were obtained using k-ε, k-ω, $\overline{v^2}$-f and Spalart-Allmaras models. They used the dynamic eddy viscosity model in the LES. The DES that was used utilized a hybrid technique in which the closure is a modification to the Spalart-Allmaras model, which reduced to RANS near solid boundaries and LES in the wake. Their simulation results were compared with experimental results and simulations were performed at Re = 100 000 where the laminar boundary-layer separation occurs at approximately 83°. The two layer k-ε, RANS predictions of the streamwise drag were found to agree reasonably well with experimental measurements. DES and LES models performed better in the aft region relating to the pressure and skin friction coefficients of the sphere. All

models predicted similar profiles of the mean velocity and turbulent kinetic energy in the near wake. They found that DES compared well with LES in that both techniques resolved eddies down to grid scale in the wake and are better at capturing unsteady phenomena.

In *et al.* (2008) found that multiple vortices are predicted to occur downstream of the spherical pebbles due to flow separation. In their research, they found that very little work has been done regarding fluid and heat transfer phenomena in a pebble bed core. They made use of a contact area based on the finding of Lee *et al.* (2007). Turbulence models that were used in their study consisted of the Spalart-Allmaras, *k*-ε and SST *k*-ω models with *scalable* wall treatments. They found that the turbulence models predicted no significant differences in the flow pattern. Regarding the streamwise velocity, their work showed that it increased by three fold more than the bulk mean velocity. A significant high local temperature was found near the pebble contact region. A variation of 25 °C was noticed on the pebble surface temperatures.

McLaughlin *et al.* (2008) made use of ANSYS FLUENT to compile all their CFD work. Their numerical models included three Reynold's Averaged Navier-Stokes (RANS) equations and for heat transfer they used the Chilton-Colburn analogy. They present a methodology in the paper for creating a *quality* unstructured mesh with prismatic surface layers on a random arrangement of touching pebbles. In their studies, they investigated the turbulent flow and heat transfer on and around discretely modeled pebbles within a structured lattice arrangement. They also identified that studies done on structured arrangements of pebbles contain a variety of model generation techniques; however, they have identified several issues specifically related to mesh generation. The most persistent problem was generating a computational mesh on a group of pebbles in contact. Due to this, meshing with tetrahedral elements becomes highly skewed around the sharp angled geometry near the contact points.

1.4. Summary of the chapters

Chapter 2 describes specific formulations and explanations of theory relevant to this thesis. The theory explained or developed is used to solve specific problems that were encountered in the course of the project.

Chapter 3 explains all experimental and practical setups that have been conducted. Shortcomings and design improvements are explained as well as the methodology that was followed to construct experiments.

Chapter 4 consists of theory and descriptions of numerical modelling. This covers all the relevant and important information that was used in the computational fluid dynamic simulation software. All the theory, constants and other information that is explained in this chapter is pertinent to the FLUENT R12 CFD package (FLUENT, 2008).

Chapter 5 describes the numerical setup that was used to model the experimental setup. This chapter explains the geometry that was modeled, and how the meshing was performed after which the boundary conditions was applied.

Chapter 6 displays all the important results that have been generated by experimental tests or numerical methods and simulations.

Chapter 7 comments on the findings of this thesis. Conclusions are drawn and discussed.

Chapter 8 gives advice on continuing with the project and how improvements can be made.

2. Theory

Throughout this chapter, theory that was used in this thesis will be presented. This is necessary since the reader might not be aware of the relevant theory or theory have been reformulated to suite certain circumstances better.

2.1. The first law of thermodynamics

For a system undergoing a thermal process, the conservation of energy may be expressed as follows: The net change in energy of the system during a process is equal to the difference of the energy entering and the energy leaving the system during the process (Çengel, 2003), which can be expressed as

$$
\begin{pmatrix} \text{Change in the} \\ \text{total energy} \\ \text{of the system} \end{pmatrix} = \begin{pmatrix} \text{Energy} \\ \text{entering the} \\ \text{system} \end{pmatrix} - \begin{pmatrix} \text{Energy} \\ \text{leaving the} \\ \text{system} \end{pmatrix} \tag{2.1}
$$

The control volume for this project will be analyzed under steady-state operating conditions as displayed in figure 2-1 hence the term energy balance will used from now on. The term steady-state implies that there is no change with time at a specific location. Due to no change in the mass flow rate $\dot{m}$ entering and exiting the system (mass balance) at constant temperature in T_{in} and out T_{out}, the energy balance for the system can be expressed as

$$
0 = \dot{E}_e - \dot{m}\left(C_p T_{out} - C_p T_{in}\right) - \dot{Q}_{loss} \tag{2.2}
$$

where $\dot{E}_e$ is the electrical energy transferred to the fluid and $\dot{Q}_{loss}$ is energy lost through the insulation by conduction and convection and radiation on the side walls.
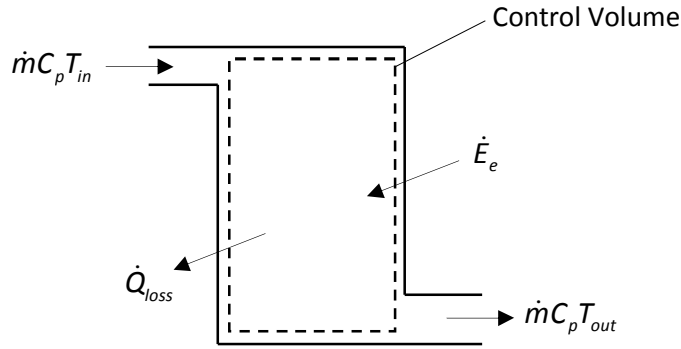
Figure 2-1: Steady flow system with constant control volume

2.2.   Ergun equation

To calculate the pressure drop across the spherical packed bed the Ergun equation (Mills, 1979) is used. The Ergun equation calculates a pressure gradient, which is multiplied by the length of the packed bed to calculate the pressure drop. The Ergun equation consists of three terms and can be expressed as

$$\frac{dP}{dx} = 150 \frac{\mu V}{L^2} + 1.75 \frac{\rho V^2}{L}; \qquad 1 < Re < 10^4 \tag{2.3}$$

where V and L are a characteristic velocity and characteristic length respectively. The first term on the right hand side accounts for the viscous drag. The second term on the right hand side accounts for the form drag. The constants are based on experimental data for many shapes of particles, but the equation is more accurate for spherical particles. The characteristic velocity can be calculated as

$$V = \frac{\dot{m}}{\rho \varepsilon_v A_c} \tag{2.4}$$

where ε_v is the average void fraction in the bulk region of a randomly packed bed and A_c is the cross-sectional area of the packed pebble bed. The characteristic length can be calculated as

$$L = d_p \left(\frac{\varepsilon_v}{1 - \varepsilon_v} \right) \tag{2.5}$$

where d_p is the effective particle diameter, which is defined as the volume divided by the surface area.

2.3. Pebble thermal contact area

The pebble thermal contact area is important as it allows heat to flow from pebble to pebble or from pebble to reflector by means of conduction. Depending on the size of this contact area, the amount of heat transferred by conduction varies. To calculate the pebble contact area more than one method will be used, which will then be evaluated.

A method used by Polson (2009) was to treat the contact region as two springs that compresses together as seen in figure 2-2. The equivalent force F and distance that was compressed 2R-P, was recorded in an experiment to calculate the spring stiffness k. The spring stiffness was calculated by Polson (2009) using equation (2.9) as 15000 kN/m. The pebble thermal contact area can be calculated as follow:

$$A_{contact} = \frac{\pi}{4} d^2_{contact} \qquad (2.6)$$

where

$$d_{contact} = 2\sqrt{P\left(R - \frac{P}{4}\right)} \qquad (2.7)$$

in addition, the combined stiffness is

$$k = \frac{k_1 k_2}{k_1 + k_2} \qquad (2.8)$$

and the pebble penetration is

$$P = F / k \qquad (2.9)$$
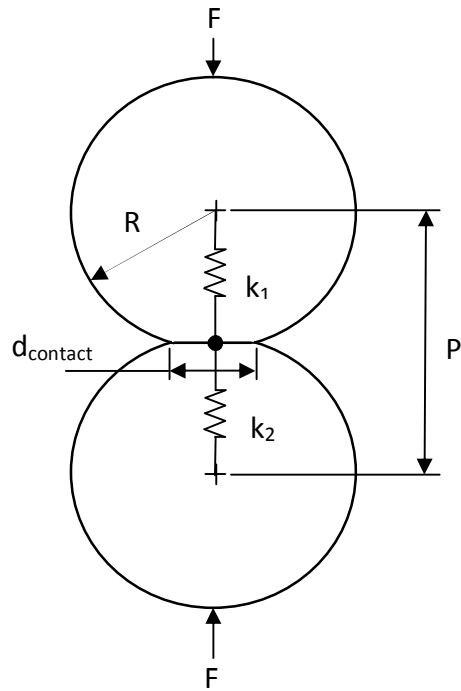
Figure 2-2: Spring representation used for contact stiffness

Using the histogram in figure 2-3, it can be seen that the force of 113 N on the contact between pebbles has the highest occurrence. Applying this force on two PBMR fuel pebbles, compresses the contact region, and thereby creating an area contact. The distance that the pebble has compressed can be calculated using the contact stiffness, which results in a value of 0.015 mm. Using this distance the diameter of the contact area can be calculated with equation (2.7) as 1.34 mm diameter.
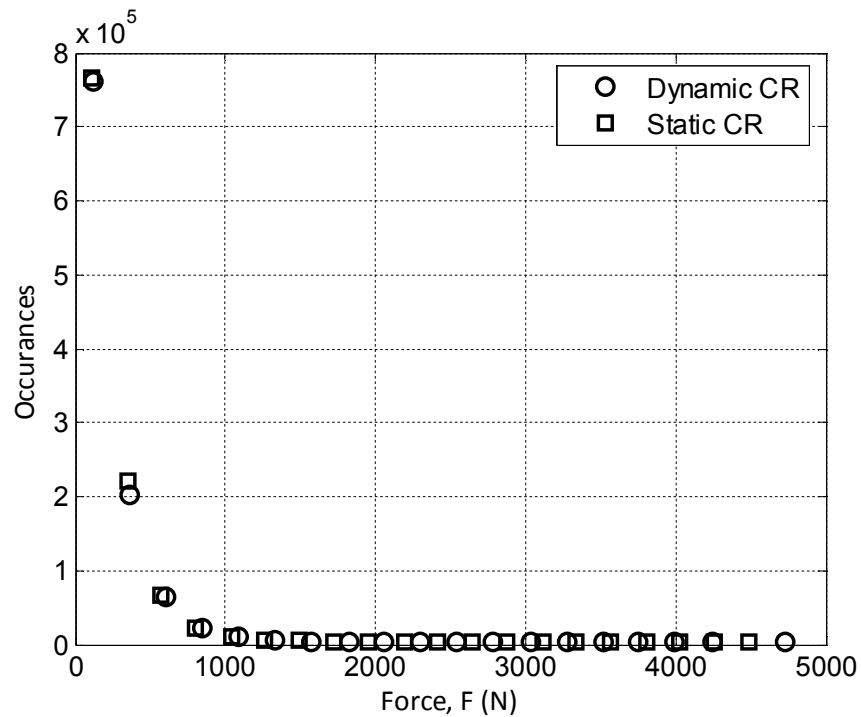
Figure 2-3: Histogram of contact force magnitudes (Polson, 2009)

As a second method based on the work of In *et al.* (2005) and In *et al.* (2006), the pebble thermal contact area diameter of 2 mm was based on the gravitational loads considered in the pebble bed core and the elastic deformation of the graphite layer of the fuel pebble. Although they claim to have used a *conservative approximation*, they feel that the results were realistic in the lower region of the pebble bed core.

These two methods give conflicting results, as the first method calculated the pebble thermal contact area diameter as 1.34 mm and the second method used a 2 mm diameter. To clarify this conflict an additional experiment will be conducted. The experimental test and results for determining the pebble thermal contact area are given in section 3.1 and chapter 6, respectively.

2.4. Effective thermal contact conductivity

Holman (1992) suggest the following method to calculate the thermal contact resistance. Take two insulated rods A and B of different materials as depicted in figure 2-4. Because the two rods are of different materials, they will have different thermal conductivities. This method also works for the case where the rods are of the same material. Next, the two rods are pressed together and insulated in the radial direction, so that the heat flux is only in the axial direction under steady-state conditions.
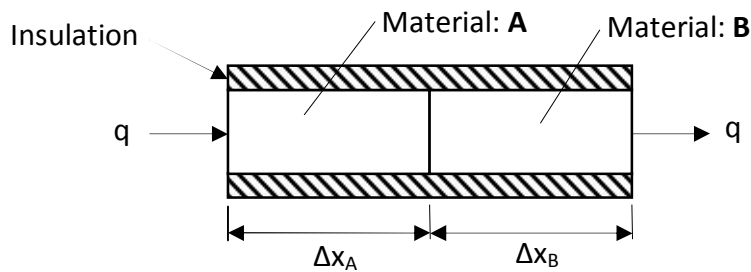
Figure 2-4: Physical situation of two materials in contact (Holman, 1992)

Holman (1992) shows that the temperature profile in the axial direction has a temperature drop at the contact plane, which can be seen in figure 2-5. The temperature drop is the result of the thermal contact resistance.
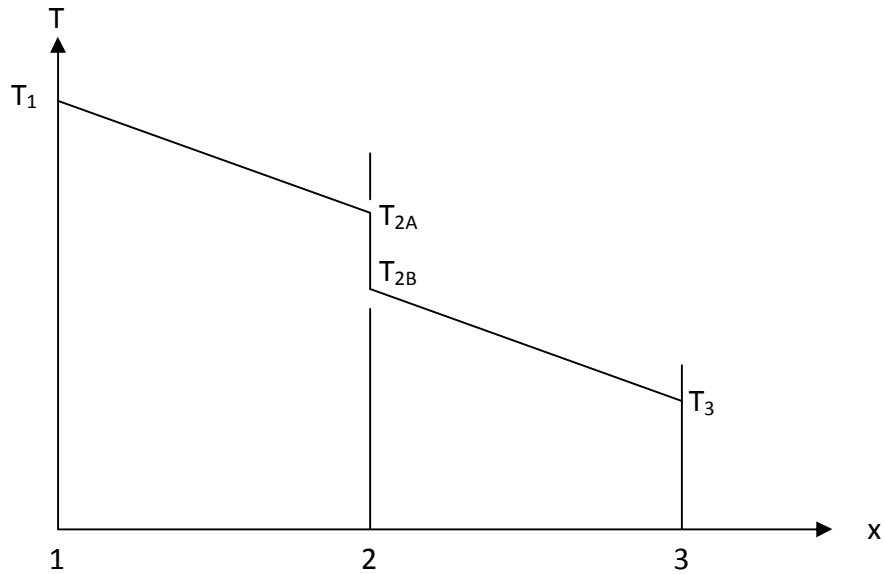
Figure 2-5: Temperature profile of the thermal contact-resistance effect

(Holman, 1992)

Completing an energy balance across the interface, the following equation is obtained

$$q = k_A A \frac{T_1 - T_{2A}}{\Delta x_A} = \frac{T_{2A} - T_{2B}}{1 / h_c A} = k_B A \frac{T_{2B} - T_3}{\Delta x_B} \qquad (2.10)$$

or

$$q = \frac{T_1 - T_3}{\Delta x_A / k_A A + 1 / h_c A + \Delta x_B / k_B A} \qquad (2.11)$$

where $1/h_c A$ is referred to as the thermal contact resistance and h_c is the contact coefficient, using Holman's (1992) terminology.

Examining the contact joint in detail, see figure 2-6, it can be seen that there are two main mechanisms by which heat is transferred across the joint. The first is conduction between the solid-to-solid asperities and the second is conduction through the interstitial gas in the void regions. Rarefied gas effects associated with the entrapped gasses plays a major role in contributing to a high thermal contact resistance relative to the conductivity of the solid materials.

Assigning A_c, as the total contact area between the solids and A_v for the void area we can now rewrite the energy balance on the rods as

$$q = \frac{T_{2A} - T_{2B}}{L_g / 2k_A A_c + L_g / 2k_B A_c} + k_f A_v \frac{T_{2A} - T_{2B}}{L_g} = \frac{T_{2A} - T_{2B}}{1 / h_c A} \qquad (2.12)$$

where L_g is the thickness of the void space, k_f is the thermal conductivity of the entrapped fluid and A is the total cross-sectional area of the rod. Therefore solving for the contact coefficient h_c we obtain

$$h_c = \frac{1}{L_g} \left(\frac{A_c}{A} \frac{2k_A k_B}{k_A + k_B} + \frac{A_v}{A} k_f \right) \qquad (2.13)$$
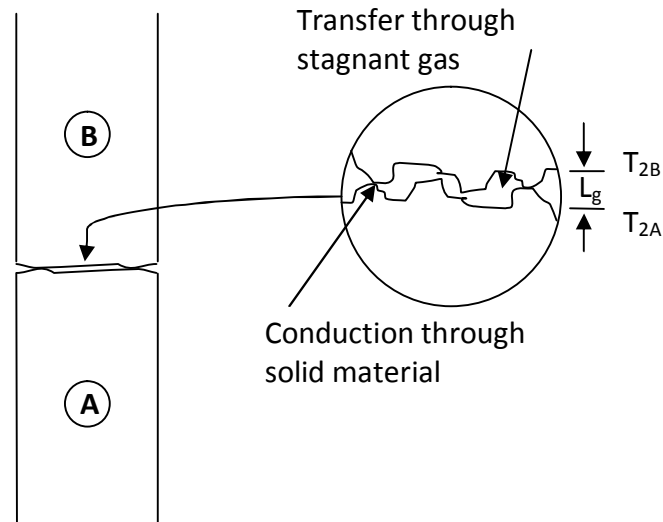
Figure 2-6: Joint roughness model for analysis of thermal contact resistance (Holman, 1992)

According to Holman (1992) the main problem with this model is that it is very difficult to determine the effective values of L_g, A_c and A_v for any two surfaces in contact with each other. Holman (1992) also stated that there are no satisfactory experimental studies that present reliable empirical correlations for all types of engineering materials. There is also no satisfactory theory that can predict the contact resistance. Improvements have, however, been made by Bahrami *et al.* (2006), but their models did not include graphite.

Therefore continuing with the model from Holman (1992), the following method to determine an effective thermal conductivity is suggested. This effective thermal conductivity will be used for the contact volume generated in the numerical model and therefore simulating the effect of contact between pebbles.

The use of contact volumes was implemented by McLaughlin *et al.* (2008), but they, however, only focused on the size of the contact volume and the effect on flow parameters. They did not mesh the graphite spheres or the contact volumes. It is significant to this study to model the contact characteristics, and its contribution to heat transfer in packed beds. It is difficult to apply the contact coefficient to a plane in the numerical model, as one would still be left with the daunting task of creating a mesh in the infinitely small angles between the pebbles. Therefore, to simulate the effect of contact between the pebbles an effective thermal conductivity is needed for the contact volume. This effective thermal conductivity would be lower than that of the material as expected.

To determine the effective thermal conductivity for the contact volume an energy balance is calculated for the case displayed in figure 2-7. The equation follows:

$$q = k_{contact} \frac{A}{L_g} \left(T_{2A} - T_{2B} \right) \tag{2.14}$$
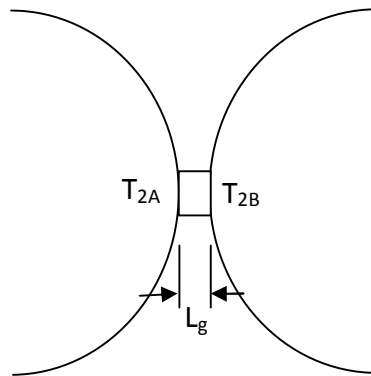
Figure 2-7: Representation of the contact volume between two spheres

Using the model from Holman (1992) this amount of energy transferred must therefore be the same, which leads to

$$q = k_{contact} \frac{A}{L_g} \left(T_{2A} - T_{2B} \right) = h_c A \left(T_{2A} - T_{2B} \right) \tag{2.15}$$

Therefore rewriting equation (2.15), $k_{contact}$ equals

$$k_{contact} = \left(\frac{A_c}{A} \frac{2k_A k_B}{k_A + k_B} + \frac{A_v}{A} k_f \right) \tag{2.16}$$

The cross-sectional area, thickness of void space and temperature difference in both instances are assumed to be the same and therefore cancels out. As far as the ratio A_c / A and A_v / A are concerned, an assumption to use the porosity of graphite is made. Specified by the manufacturer, the porosity for the graphite used was 20 %. This results in $A_c / A = 0.8$ and $A_v / A = 0.2$. The thermal conductivity of both graphite spheres is the same and thus the final equation describing the effective thermal conductivity is

$$k_{contact} = \left(0.8 k_{graphite} + 0.2 k_f \right) \tag{2.17}$$

3. Experimental setup

An experimental setup was built to measure the pebble temperature by using the temperature measured in the inspection channel and to measure a peak in temperature in the temperature profile along the channel. In the following sections, the experimental test setups and their detailed designs are described.

3.1. Pebble thermal contact area experiment

The pebble thermal contact area experiment was done to confirm the findings of Polson (2009) and In *et al.* (2005) given in section 2.3. Two spheres were pressed together and the contact area between them was measured. This test arrangement can be seen in figure 3-1. A Hottinger Baldwin Messtechnik (BSM) S9 force transducer was used to measure the applied force. The force was applied by using a MTS hydraulic press. Data acquisition was done using the MTS Spider 8 and a MTS Transducer Conditioner was connected in-line with the MTS Spider 8.

The contact area diameter was determined by using a piece of paper, which was inserted between the pebbles. Once a force is applied to the pebbles, the graphite leaves an imprint of the area that was in contact. The two pebbles were placed inside a wooden box to ensure that the pebbles are aligned and that the applied force is exerted in the vertical direction.
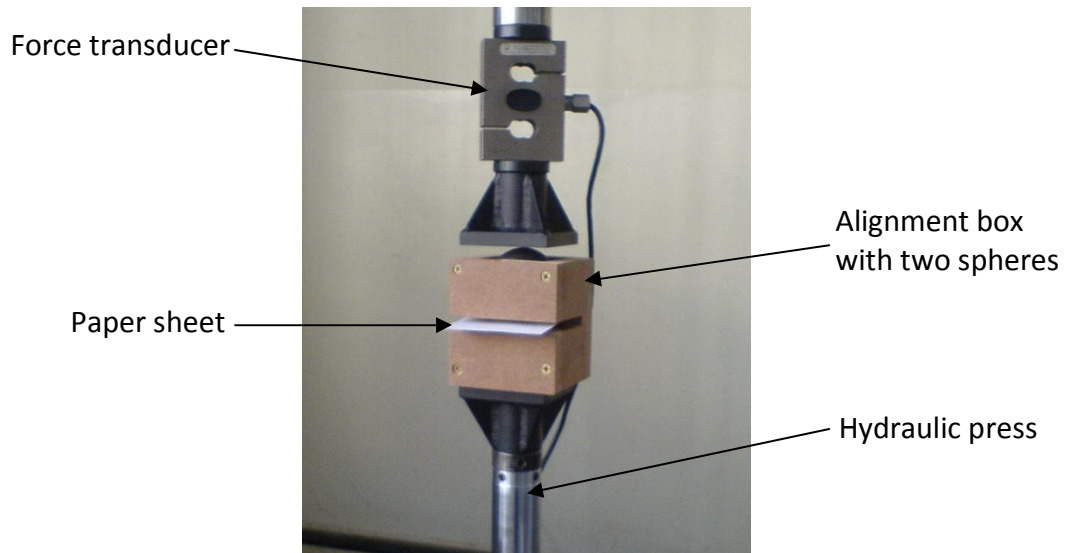
Figure 3-1: Experimental setup used to determine the contact area between two spheres as a function of the applied force

The paper used, was 80 g/m^2 A4 white paper. A procedure was followed to conduct the test and is given in Appendix F. Figure 3-2 show an image of the imprints left by the pebbles after a force had been applied to press them together.
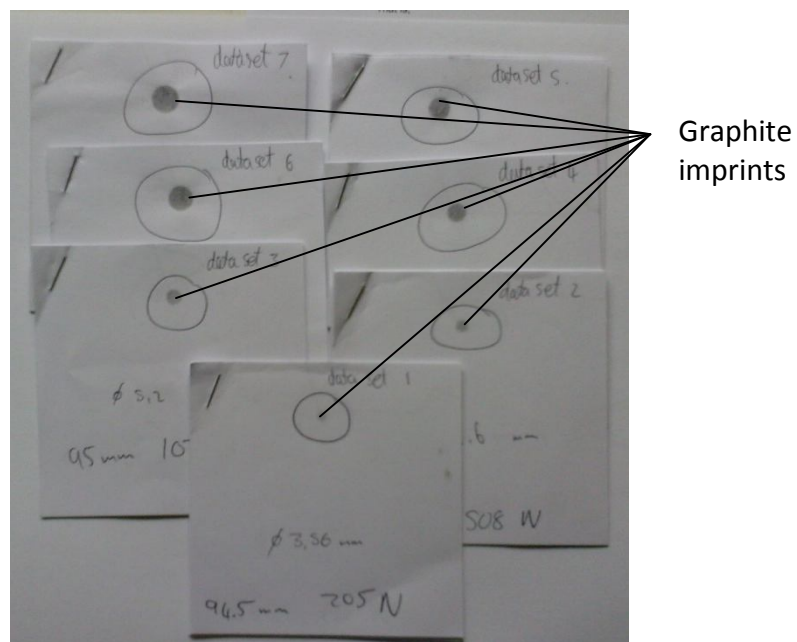
Figure 3-2: The imprints left by the graphite pebbles on the paper

Calibration information of the BSM S9 force transducer used can be found in Appendix C. The pebbles, manufactured by SGL were supplied by PBMR (Pty) Ltd and their properties can be found in table 3-1.

Table 3-1: Properties for pebbles used in experiments (SGL-Carbon-Group, 2006)

	With Grain	Against Grain	General	Units
Crushing Strength			27 - 32	kN
Young's Modulus	9.3	6.4	7.85	GPa
Anisotropy Factor	3.13	4.4	1.41	$10^{-6}/°C$
Bending Strength	21	16	18.5	MPa

3.2. Electrically heated packed bed and enclosure

The design for the enclosure is similar to the North-West University High Pressure Test Unit (HPTU). As seen in figure 3-3, they used aluminum plates that were bolted together. They have holes in the top and bottom, which allowed the fluid to flow through. Two plates, from which the acrylic pebbles were suspended, closed the top and bottom sections. This experiment was used for pressure drop, convection coefficient, near-wall, braiding effect, small cylindrical packed bed, and small annular packed bed tests. These tests were done at temperatures lower than 75 °C (NWU, 2007).
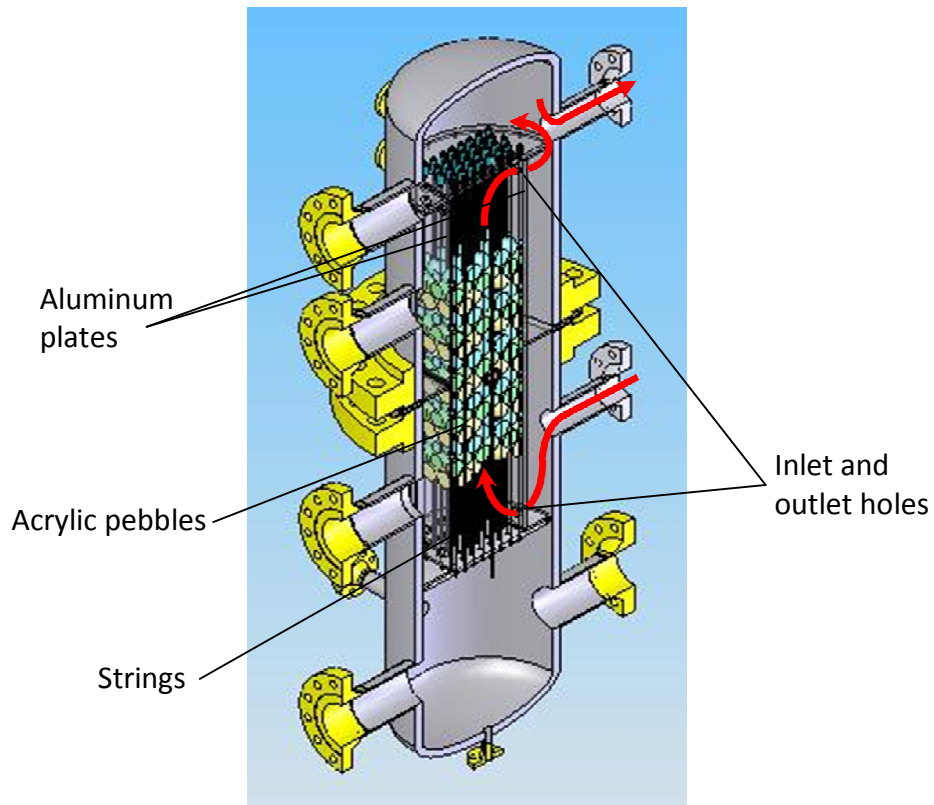
Figure 3-3: High-pressure test unit (NWU, 2007)

Figure 3-4 shows most of the components in the design of the pebble bed experiment. Air flows in from the inlet pipe, through the inlet manifold, down the enclosure and through the pebbles. After which the heated air flows out through the outlet manifold and through the outlet pipe. The hot air is directed to flow to the outside of the building. If this was not done recycling of the hot air could result in the experiment not reaching a constant inlet air temperature. An insulation material was place around the enclosure and reflector block. This decreased the heat lost to the environment and helped to improve the accuracy when calculating an energy balance.
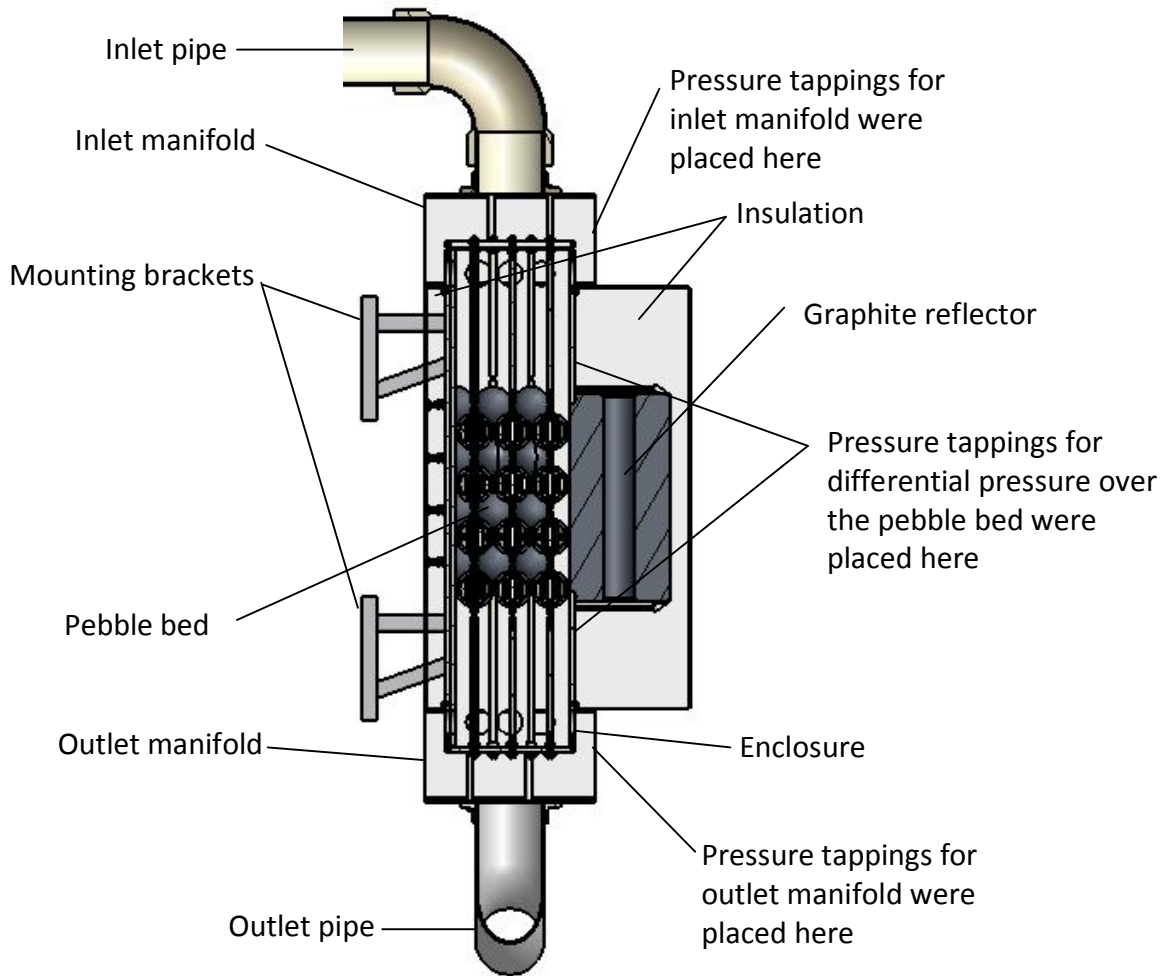
Figure 3-4: Cross-section of the pebble bed experimental setup
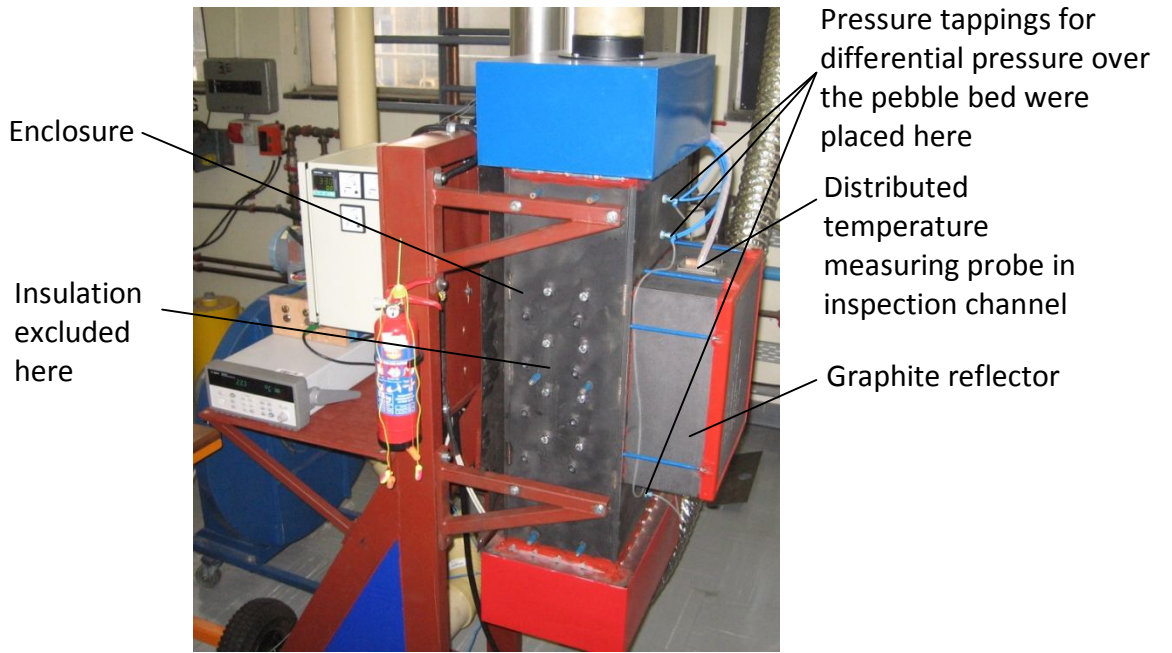
(a)
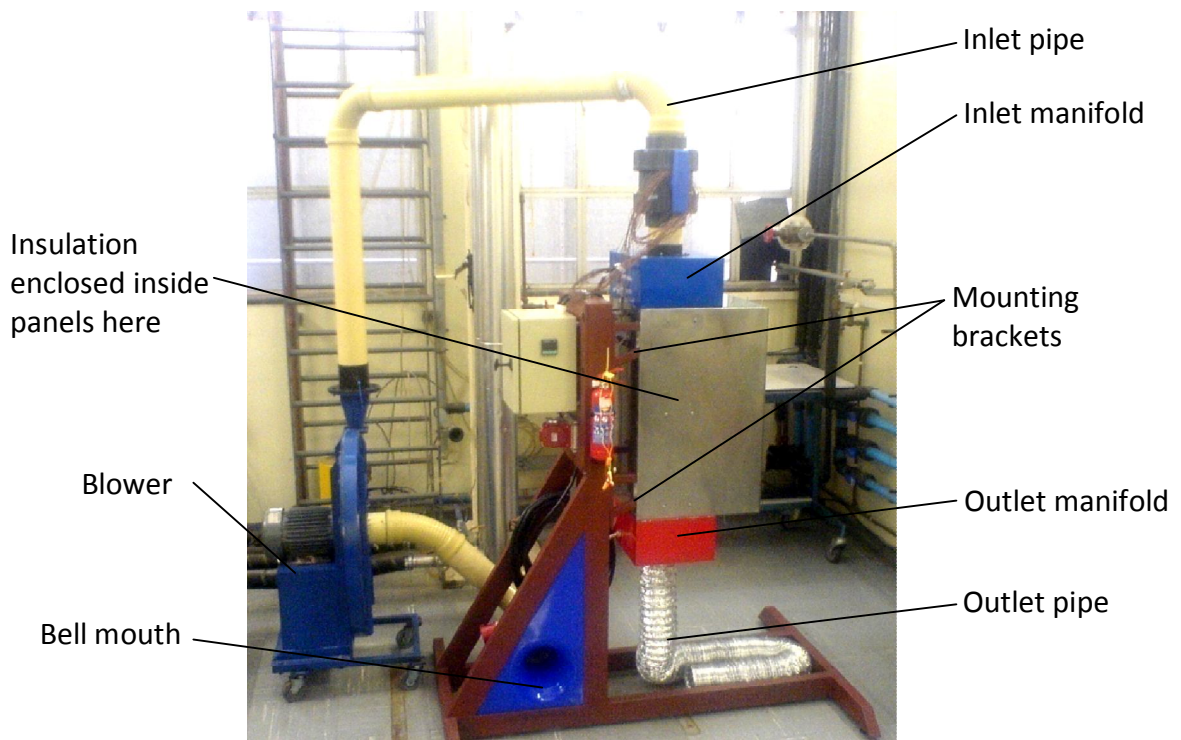
(b)

Figure 3-5: Photographs of the pebble bed experimental setup (a) without insulation, (b) with insulation

3.3. Electrically heated graphite pebble

The PBMR fuel pebbles in the reactor produce heat, with a maximum of 6.5 kW, (Slabber, 2004). Researchers such as Laguerre *et al.* (2007), Van Der Merwe *et al.* (2006) and NWU (2007) made either use of a heated wall or heater elements at the centre of the pebble bed to determine heat transfer characteristics within pebble beds. This is not how heat is generated in the PBMR fuel and does not accurately represent the heat generated in the pebbles. It was decided that if heated pebbles were used it would be more representative of the how the fuel pebbles transfer heat in the PBMR reactor.

To simulate the thermal behavior of a PBMR fuel spheres the inner 50 mm diameter is replaced by an electric heater. The electrical heater consists of an electrical resistance wire embedded in a matrix of plaster of paris. After testing it was found that the design (termed the first design) could be significantly improved, hence a second design was used. Both design are, however, described and discussed in the sub-sections that follow.

3.3.1. First design

The design requirements were that the pebbles must be able to reach a temperature of 350 °C on the inner surface of the graphite shell, yet maintain their structural integrity. The temperature of 350 °C was chosen as it was expected that the center core temperature of the pebble would be much higher and could reach the melting point of the resistance heating wire. It should also be possible to pack the pebbles into a face centered cubic (FCC) or body centered cubic (BCC) packing. The pebbles had to operate from a 220 Vac supply and this power supply could be either three phase or single phase, depending on how the pebble resistances network was configured.

To evenly distribute the heat generated by the electrical element, the design of the heating elements entailed a ceramic cluster in which the electric element is wound. The main function of the ceramic cluster was to ensure that the electrical element wire stay in place until it has been moulded in the insulative filler material. Another reason for the use of the ceramic cluster was to make sure that the pebbles, once placed inside the required packing, that the electric element wire stays in place. To keep the pebbles in the required packing, stainless steel springs and copper tubes aligned the pebbles.

The electrical resistance wire form the heating element was made from 0.5 mm nickel-chrome wire. The wire thickness was chosen as it was more flexible and made wiring the ceramic cluster easier. This wire was spiraled with a diameter of 5 mm and stretched so that it does not short circuit with itself. The reason for this was to ensure that the maximum length of wire is used to keep the surface heat flux as low as possible. By doing this the total heat transfer area of the electrical wire is increased, thereby decreasing the wire temperature. In addition, by decreasing the wire temperature, the wire is less likely to degrade or melt. The average total resistance of the wire in a heater pebble measured 20 Ω. Four of the heater pebbles would then be placed in series, and 28 of these strings will then be placed in parallel, forming the electrical resistance network to heat the pebbles (see figure 3-18).

To insulate the electrical element wire from itself and to any other parts that it might touch, plaster of paris was used as a filler. Another reason for using a filler material was to create a solid volume onto which the graphite shells could be glued. The plaster of paris proved to work very well, as it could be mixed into a watery solution, making it easier to flow in between the windings of the element wire. Plaster of paris contains bounded water that is released at temperatures higher than 120 °C. If the pebble was to be rapidly heated, the water will steam and build up pressure. A high pressure buildup in the pebble may possibly crack

the graphite shell. Fortunately there are many pores in the pebble which allow steam and other gasses to escape, provided that the temperature increase remains below 60 °C/h.

The graphite shells were manufactured from solid graphite pebbles, which were supplied by PBMR (Pty) Ltd but manufactured by SGL (Pty) Ltd using reactor grade graphite stock (SGL-Carbon-Group, 2006).
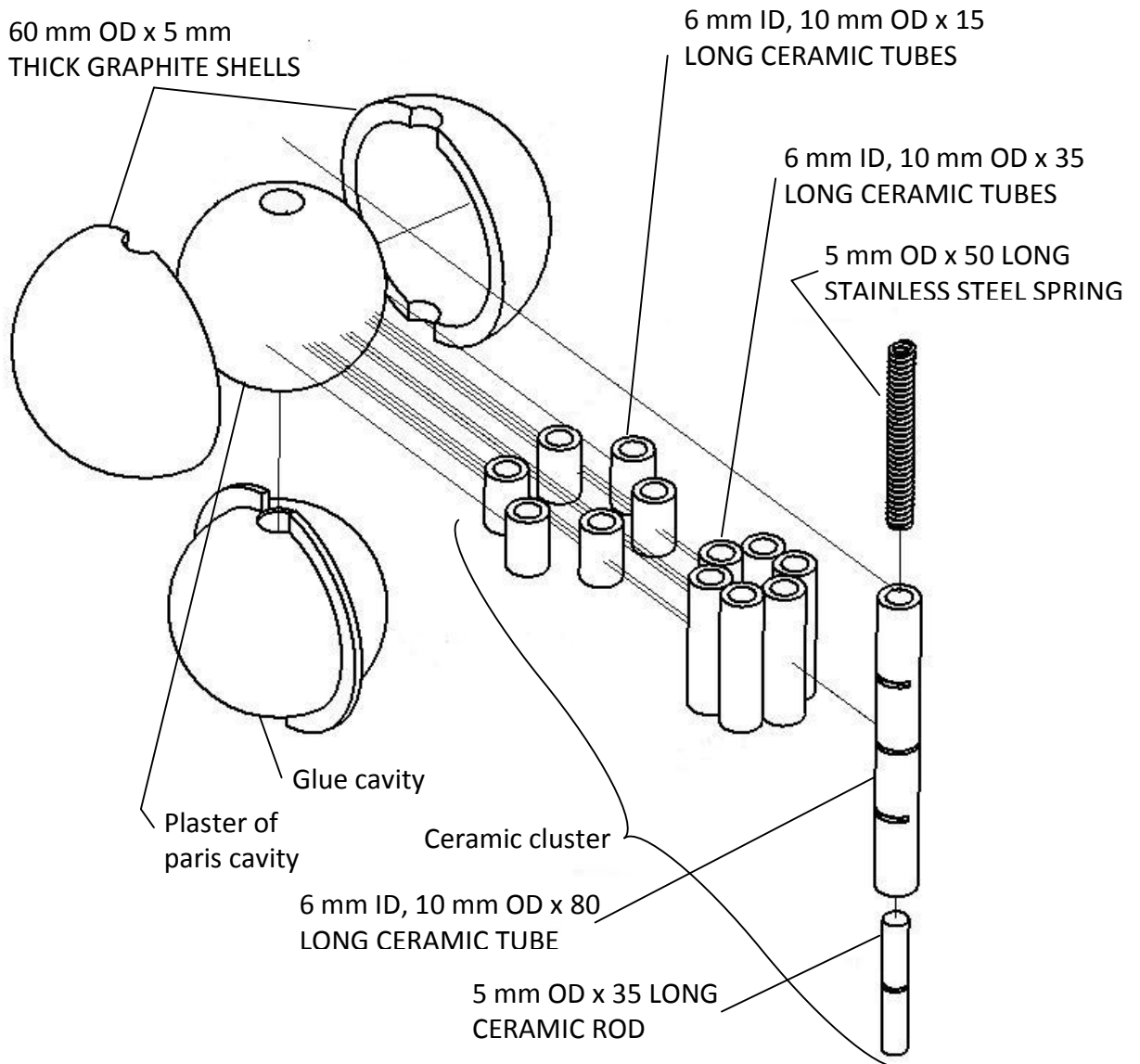
Figure 3-6: Exploded view for the first design of the electrically heated graphite pebble
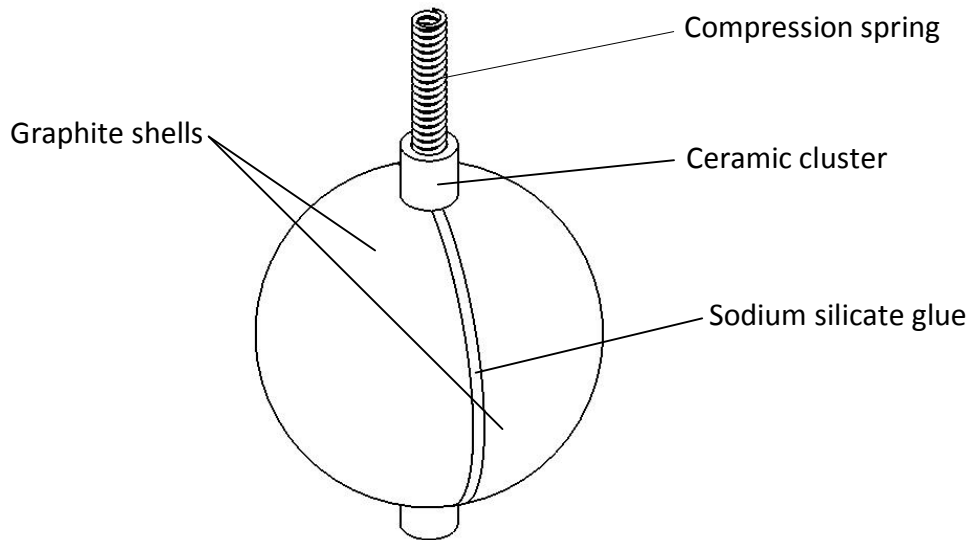
Figure 3-7: Assembled view of the first design of the electrically heated graphite pebble

A sodium silicate base glue (Honeywell, 2009) was used to bond the graphite shells and the plaster of paris filled cluster together. This glue could withstand temperatures higher than 1000 °C. Figure 3-6, figure 3-7 and figure 3-8 show the exploded and assembled views, and construction of the first electrically heated graphite pebble.
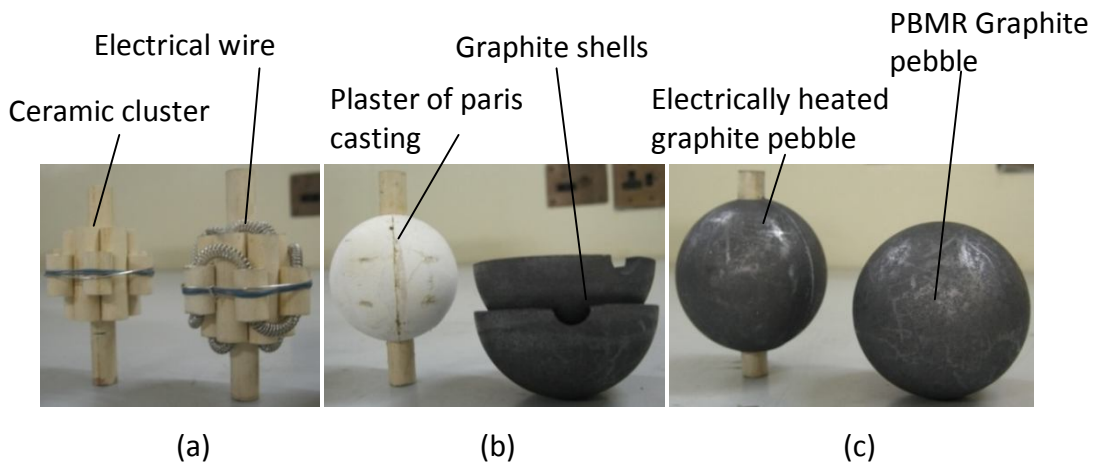
Figure 3-8: (a) Ceramic cluster unit and electrical heating wire; (b) Casted plaster of paris casting and graphite shells; (c) Complete assembly of the first electrically heated pebble and a PBMR graphite pebble

To measure the temperature inside the graphite shell, a k-type thermocouple was used. The thermocouple was placed on the inside of the shell, just before the two shells were glued to the plaster filled cluster. It was assumed that the measured temperature will represent the temperature everywhere on the inside wall of the shell, therefore the placement of the thermocouple was not marked. The electrical heating wire in each pebble was tested for continuity, short circuit and earth leakage before the pebbles were inserted in the packed bed to ensure that they were in a working order. To establish if the pebbles were producing an even temperature on the surface an infra-red camera was used to take a picture relating to temperature. One of these pictures can be viewed in figure 3-9, where it is evident that there is an even pebble surface temperature with no isolated hot spots. It is also clearly seen from the colour contrasts that the ceramic limits the heat conducted away from the pebble.

Ceramic tubes have a lower temperature than pebble surface, thus well insulated and limiting heat conduction away from pebble.

Even surface temperature on graphite shell
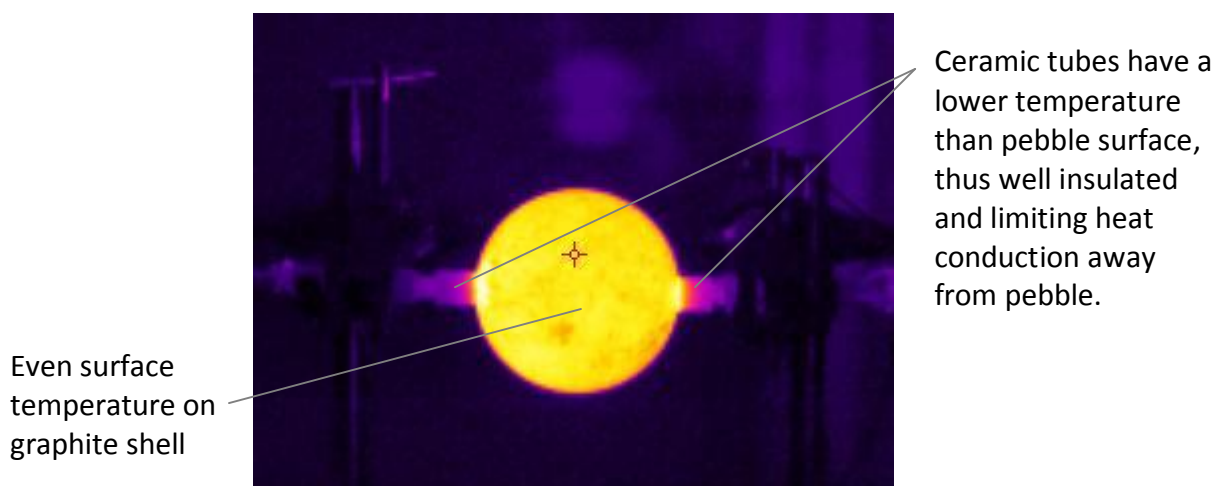
Figure 3-9: Infra-red thermometry of pebble surface temperature

The first design failed due to some practical shortcomings. The problems that were encountered are listed below:

o Improper electrical contact between the spring and the element wire.
o Short circuit between the graphite shell, thermocouple, element wire and therefore causing an earth leakage.
o Variable pebble diameter.
o High concentration of water inside pebble.
o Difficulty of inserting thermocouple and marking of its location.
o Arrangement of pebbles into a cubic packing.
o Construction was time consuming.

To solve these shortcomings it was necessary to redesign the electrically heated pebbles.

3.3.2. Second design

In the first design, the improper electrical contact between the compression spring and the heating element wire contact caused arcing, which increased the wire contact temperature. The wire already had a high local temperature being close to the pebble center. Due to this hot electrical contact, when the pebble temperature increased, the wire temperature increase beyond its melting point. When the wire melted, the electrical contact broke, breaking the electrical path to the other three pebbles. Contact between the spring and wire was prevented by impurities such as the plaster of paris dust. To solve this it was decided that the electrical contact had to be a cold contact. This meant that the electrical contact between the pebbles had to occur outside of the pebble, where the coolant can cool the contact. To achieve this, it was decided that the wire would be extended to the outside of the ceramic tube and bent over towards the outside, as seen in figure 3-11. This wire will then make contact with the next

pebble by means of brass sleeves that is fitted over both ends of the center cluster ceramic tube. Figure 3-10 and figure 3-11 shows the second design.
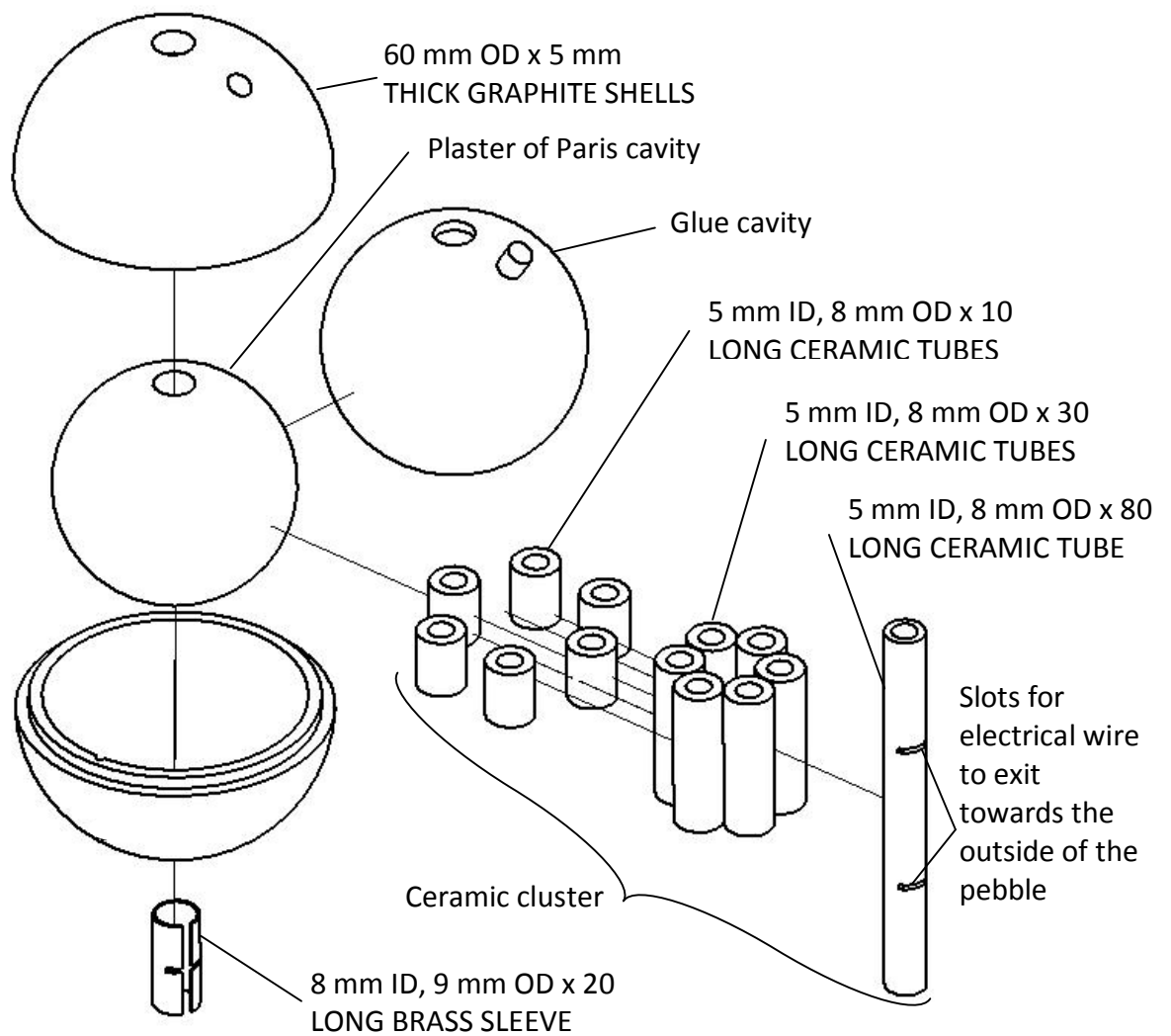
Figure 3-10: Exploded view of the second design of the electrically heated graphite pebble
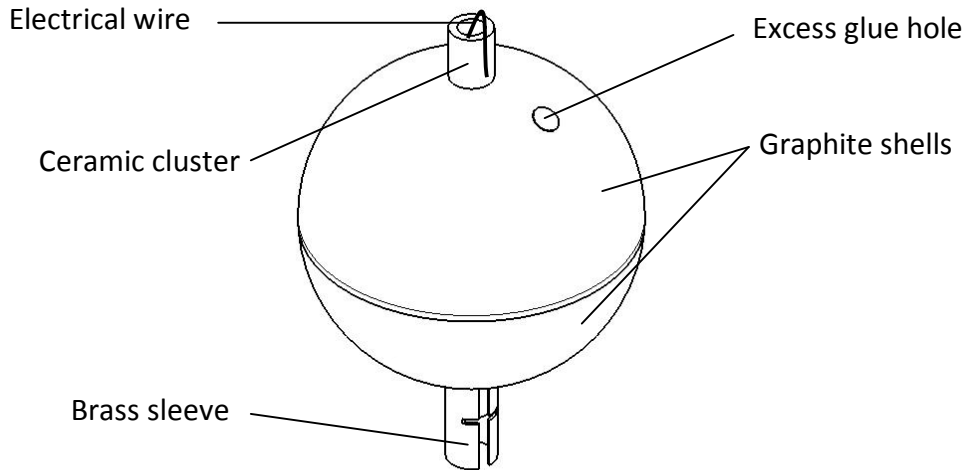
Figure 3-11: Assembled view of the second design of the electrically heated graphite pebble

To reduce or eliminate the chance of a short circuit or earth leakage to the graphite shell, a number of design improvements have been made to the thermocouple placement and heating element. The first design improvement was to reduce clearance between the maximum and minimum diameters of the casted plaster of paris filled ceramic cluster and the graphite shells. This clearance between the graphite shell and the electrical wire was increased from 0.5 mm to 2 mm, by decreasing the overall size of the ceramic cluster. The disadvantage of decreasing the size of the ceramic cluster was that the total power that could be generated by the pebble decreased as the total length of the electrical wire decreased. If the same amount of power were to be delivered the core temperature would have had to increase and that risked melting the wire. The new electrical wire that was supplied also had a higher resistance per meter. This too contributed to lowering the pebble heat generation with the same applied voltage, from 150 W to just less than 100 W per pebble. Secondly, the electrical wire was coated (Powerkote, 2009) with a ceramic coating. This helped to limit short circuiting between the spiral coils and electrical contact with the graphite shells. It also limited initial electrical conduction through water

between the wire and the graphite shells. To position the smaller heating element a clamp was designed that held the ceramic cluster in place while spacing the graphite shells, see figure 3-12 (c). This ensured that each casting was centered in the spherical shell, allowing the glue to insulate it from the graphite. Figure 3-12 shows the ceramic coated electrical wire along with the smaller plaster of paris casting and clamped assembly.
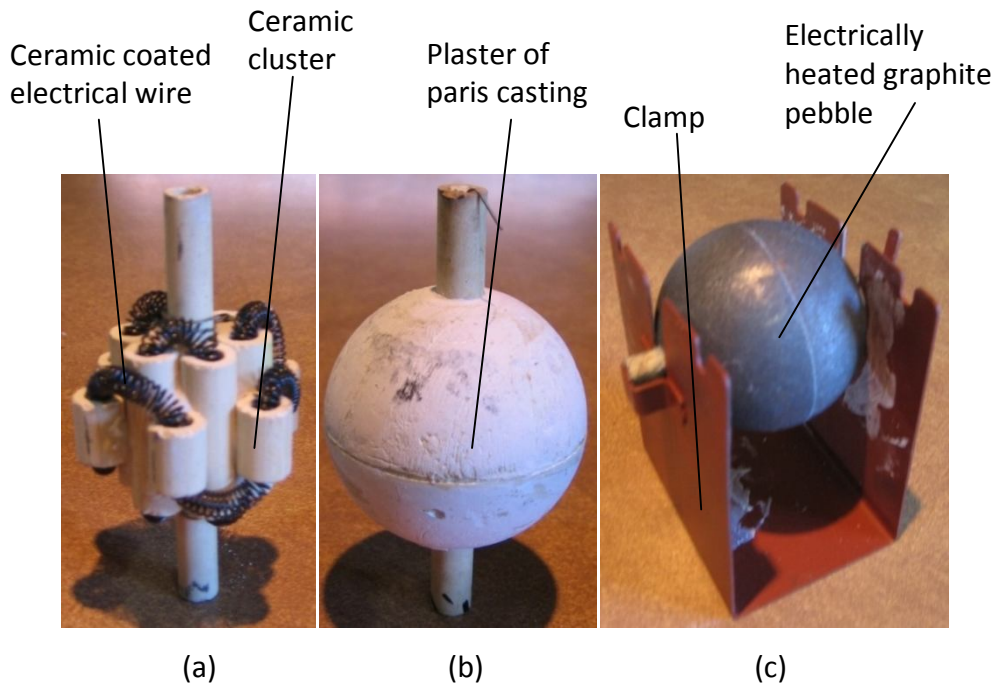
Figure 3-12: (a) Ceramic coated electrical wire and ceramic cluster; (b) Plaster of paris casting; (c) Complete assembly and clamp

The graphite shells were made from the same graphite as what was used for the reflector and they were machined from a solid 70 mm diameter rod. To ensure a spherical fit between the two graphite shells, alignment steps were machined into the two semi-spherical shells as shown in figure 3-13. When glued, this joint also provides a firm enclosure; casing the electrical heating element. This joint did not allow any excess glue to squeeze out as with the first design and therefore a 5 mm hole was added in each shell, see figure 3-11. The holes were also placed so as not to interfere with the pebble to pebble or pebble to reflector

contact areas. Once the glue hardened, the excess was filed off. A small hole for the thermocouple wire was also provided at the top of the shell.
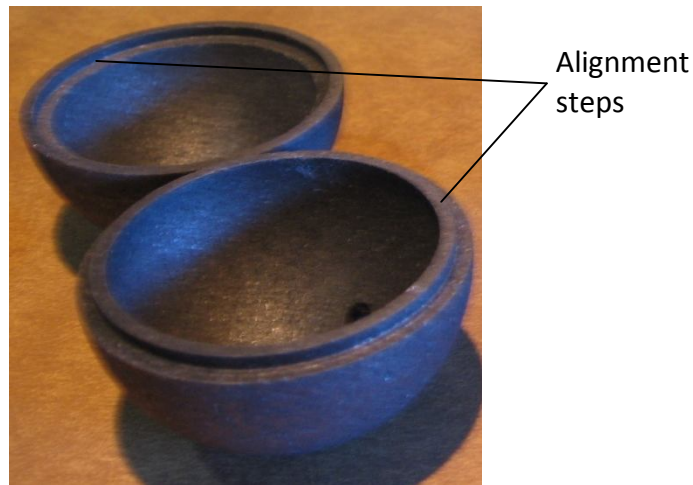
Figure 3-13: Graphite shells

To release the trapped water inside the pebble, it was slowly heated in an oven until the moisture inside the spheres evaporated. It was found that even when heated to 200 °C in an oven for more than 24 hours, there was still a small amount of moisture inside the pebble. To eliminate the remaining moisture the pebbles were individually electrically heated to 250 °C for at least 3 hours. Using the pebbles own heat source eliminated the extra remaining water.

A very important problem that had to be solved was inserting the thermocouple into the pebble and marking its location. In the first design it was assumed that the temperature on the inside surface of the graphite shell was uniform. Therefore, the location of the thermocouple was not important, but it was decided that with the second design the thermocouple would be placed at the correct location inside the pebble. An extra hole was placed in the top of each shell, which marked the location of each thermocouple, so that the pebble can be correctly positioned when placed in the packed pebble bed. The thermocouples were insulated with the glue prior to being glued onto the shell. Due to the precise placement and marking of the thermocouple junction, the

pebbles could be positioned so that the thermocouples can measure the temperature in the proper location without uncertainty.

With the first design, the springs buckled as seen in figure 3-14. This problem was solved by placing the ceramic ends of each pebble inside a brass tube as seen in figure 3-15. With the brass tubes and springs, it was still a tedious process to pack the pebbles in the enclosure without damaging the pebbles. This problem was eliminated when brass sleeves was used to slide over the ends of the ceramic cluster and heating element wire, see figure 3-11.

Buckling of springs
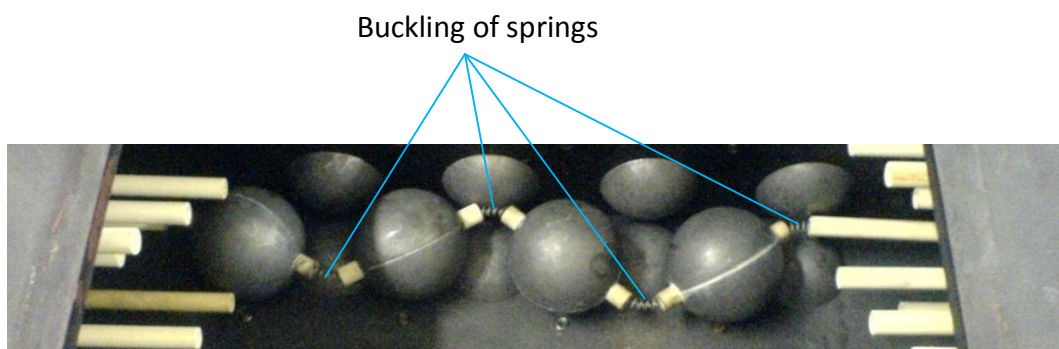
Figure 3-14: Buckling of pebble string
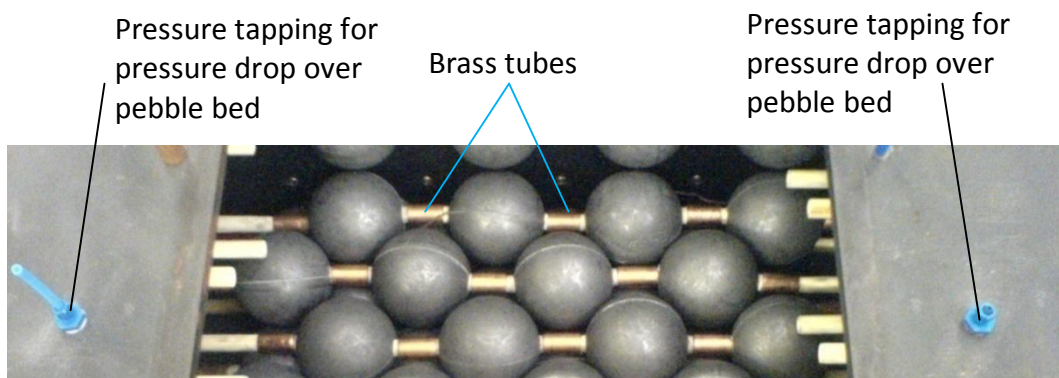
Figure 3-15: Brass tubes helps to align pebble string and pressure tapping

The tight fitting sleeve helped to align the pebbles. It was easier to pack the pebbles using the brass sleeves than with the previous design. A supporting steel grid was cut with a laser to hold the connecting rods in place, see figure 3-16. This restricted any bending movement of the connecting rod and was placed

between the pebbles and the top and bottom of the enclosure. The final packing of the pebbles before closing the enclosure is displayed in figure 3-16.

`

Steel enclosure
Ceramic inserts
Connecting rods
Electrically heated graphite pebbles
Supporting grid for connecting rods
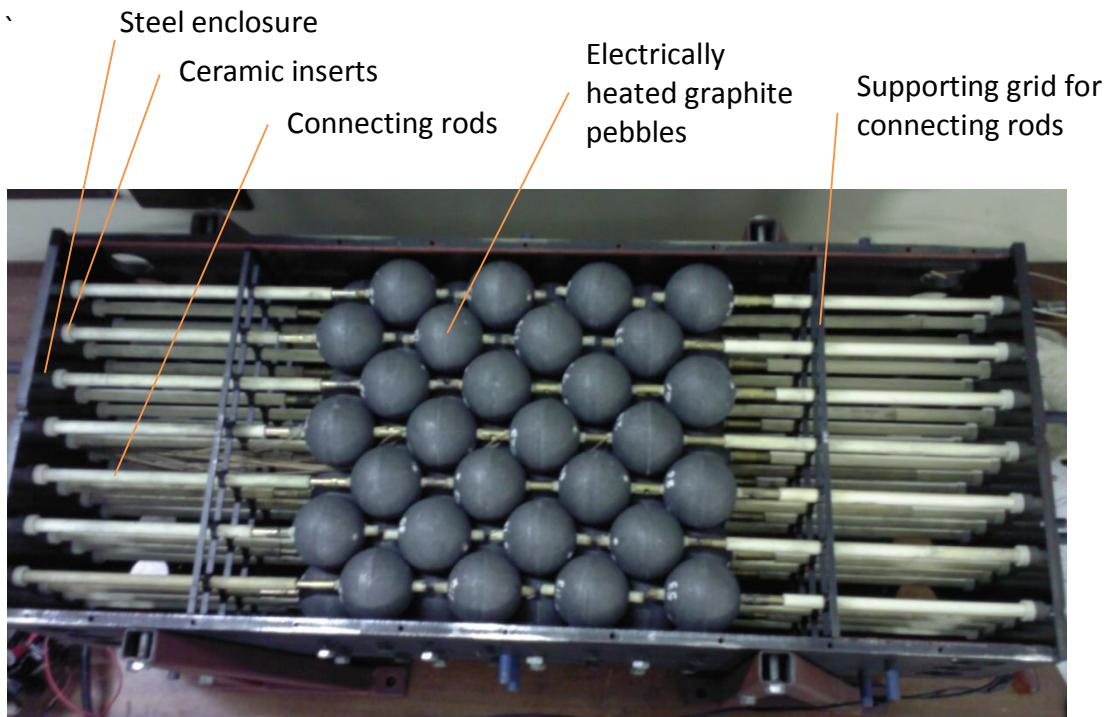
Figure 3-16: Final packing of pebbles before closing the enclosure

It was identified that time could be saved by finding a faster construction method for the ceramic cluster unit. A plastic jig, which kept the ceramic tubes in place while gluing them together as seen in figure 3-17, was used to reduce assembly time.

Sodium silicate glue
Ceramic cluster
Plastic jig
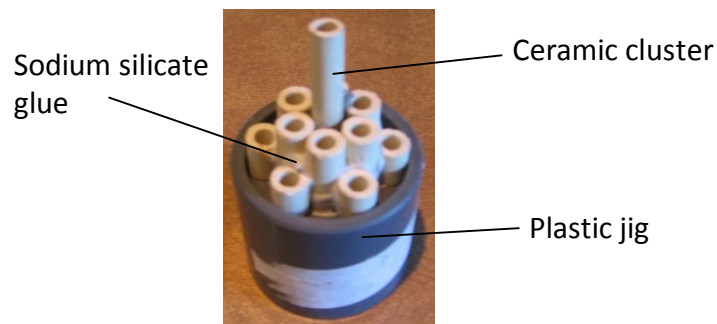
Figure 3-17: Glued ceramic cluster in plastic die

3.4.   Auxiliary components

Supplementary components such as a power regulation circuit, bell mouth flow meter, blower and frequency inverter unit helped to complete the pebble bed experiment. A power regulation circuit was used to control the electrical power delivered to the electrically heated graphite pebbles. A bell mouth flow meter was attached to the inlet of the blower unit to measure the air mass flow rate and to control the blower unit a frequency inverter unit was built. Each are now further explained in the following subsections.

3.4.1.   Power regulation

To electrically power the pebble heaters, the first attempt was to make use of a three phase line. The reason for this was that the total power could then be divided between three lines, therefore balancing the power consumption on the three phase lines. The pebble heater strings were then bundled together to form three resistance lines. The power that is supplied to the pebble heaters is then controlled with three solid state relays (SSR). Each SSR, capable of switching at 230 V and 40 A was connected to a line. A GEFRAN G600 controller controlled the pulse width modulation. The sample period was set to its fastest of one second.

The three-phase configuration was attempted on the first design of the pebbles and was unsuccessful. The reason for it not being successful was that there were earth leakages paths between the pebbles. This resulted in the electrical resistance wire in the first pebble, of each string of four pebbles, melting due to the high line-to-line voltage of 380 Vac. To minimize the voltage drop between pebbles and limiting the path that the electrical current can flow, it was decided to only use one line. Thus all of the pebble strings were connected in parallel with the live connection at the top of the pebbles and the neutral at the bottom. The earth wire was connected to the experiment enclosure, making it electrically

safe. Figure 3-18 shows the schematic layout of this configuration. An Ampere meter was connected to each pebble bundle, see figure 3-18. This was used as a visual monitor to monitor the pebble strings.
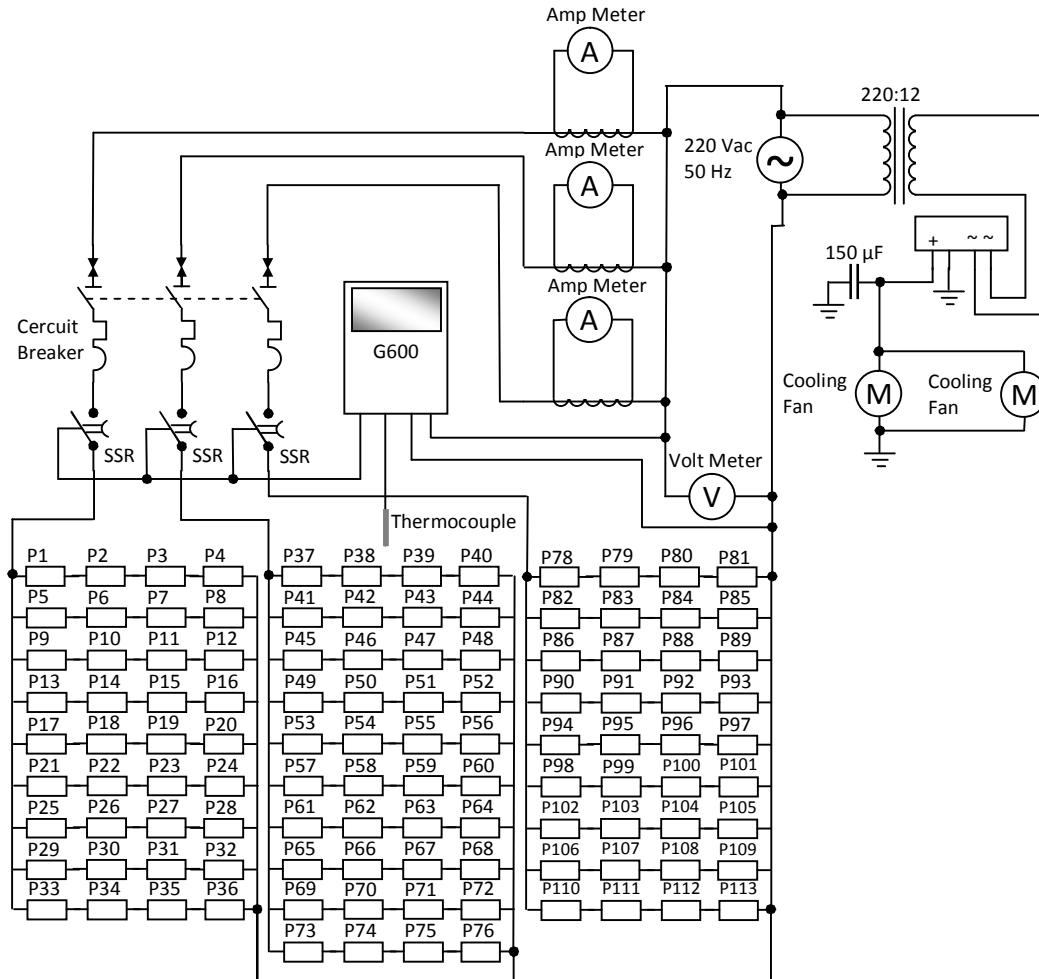
Figure 3-18: Main power regulation circuit schematic

3.4.2. Bell mouth flow meter

A bell mouth flow meter was designed in accordance with British Standards (British Standards Institution, 1981). The inside diameter of the bell mouth flow meter is 0.105 m and closely matched the diameter of the pipe used. The mold together with other wooden material was used to form a new mold. The new mold produced a fiberglass casting of the bell mouth, which is fitted to the frame

as shown in figure 3-19 (a). The bell mouth was sanded down and sprayed with a coat of clear lacquer to produce a smooth surface finish, which reduces inlet resistance. Pressure tappings and a thermocouple probe were place on the bell mouth flow meter as shown in figure 3-19 (b) and were used to determine the air mass flow rate. The air mass flow rate was calculated using the method given by (Kröger, 1998)

$$\dot{m}_{air} = C_n \phi_g Y A_n \left(2 \rho_n \Delta p_n \right)^{0.5} \tag{3.1}$$
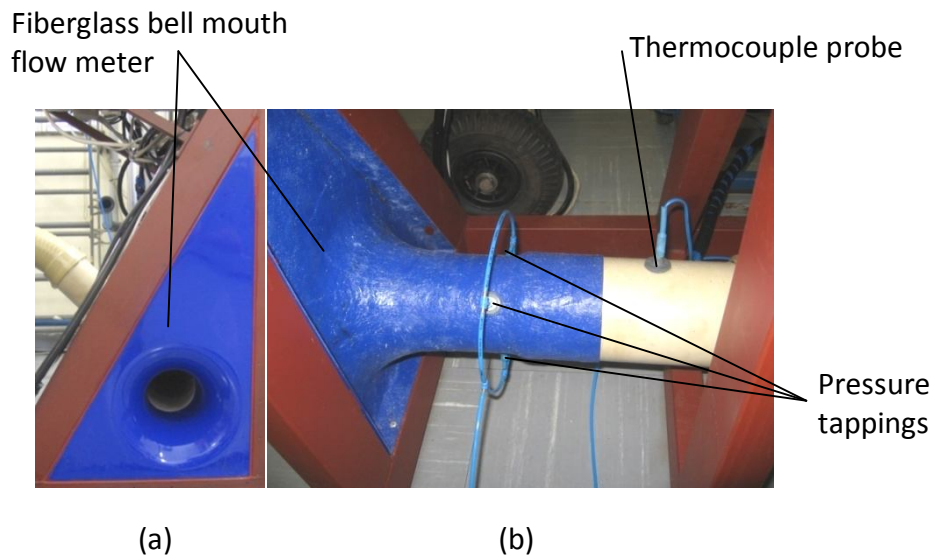
Figure 3-19: (a) Bell mouth flow meter fitted into the steel frame; (b) Pressure tappings and thermocouple probe for air flow measurements

3.4.3. Blower and frequency inverter unit

The 3 kW centrifugal blower manufactured by Continental Fan Works that was used is shown in figure 3-20. The blower's three phase motor's maximum rotational speed was 3000 rpm, at which it could maintain a maximum system pressure of 4.5 kPa. To control the blower the Mitsubishi E700 frequency inverter unit was used as shown in figure 3-20. To protect the frequency inverter unit from dust and water ingress, it was built into the steel enclosure shown in figure 3-20 (b) and (c). The frequency display screen, hand held forward/reverse

and frequency adjustment unit were mounted on the outside of the enclosure for easy reading and adjustment of the frequency.
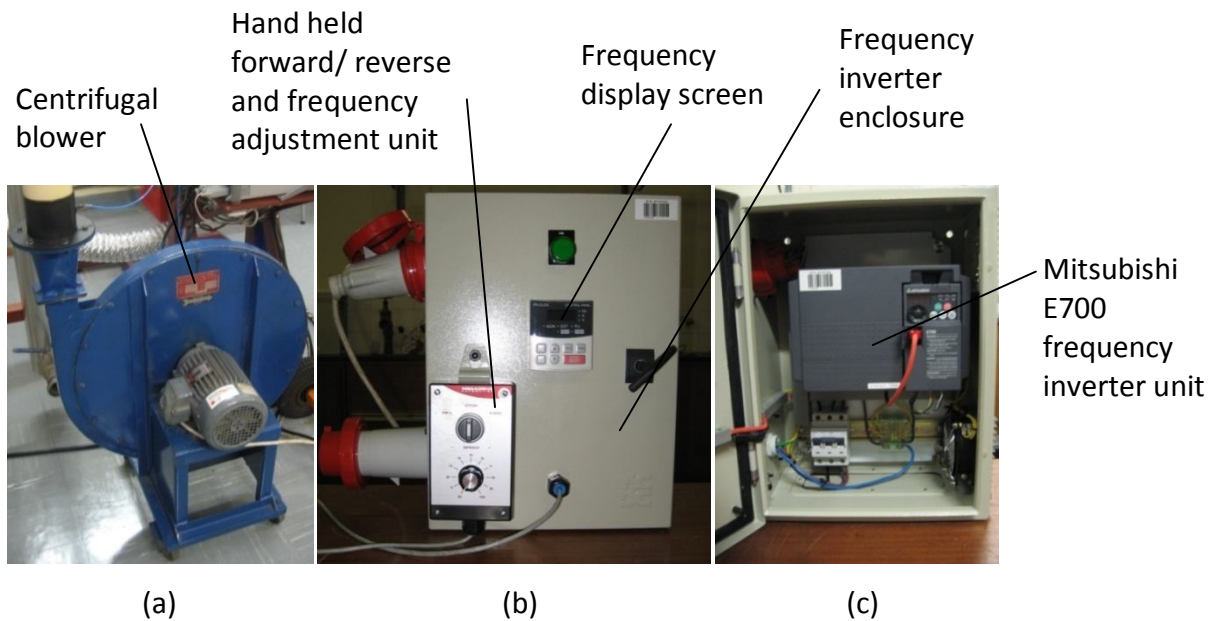
Figure 3-20: (a) Centrifugal blower; (b) Frequency inverter enclosure; (c) Frequency inverter unit

3.5.   Safety provisions

The graphite used to manufacture the pebbles could ignite if heated above 500 °C in air (Li and Sheehan, 2007 and Kim and No, 2006). This poses a possible fire hazard. There was also an electrocution hazard due to the high voltages used in powering the blower and pebbles. Safety measures that include a fire extinguisher, a safety valve and an electrical shock sign board are shown in figure 3-21.

To provide a reactive safety measure for the fire hazard a fire extinguisher was placed on the framework of the experiment. There was also a secondary fire extinguisher at the entrance door of the room. If the pebbles were to ignite and start burning, it is important to stop airflow that can provide oxygen to the fire. If the pebbles should start to burn, the operator should first switch off the power

at the wall socket and thereafter discharge the fire extinguisher into the bell mouth. While the blower's impeller is turning it will draw the CO_2 from the fire extinguisher into the pebble bed, extinguishing the flame. Only then should the safety valve, shown in figure 3-21 be closed to prevent any extra air from entering the enclosure. The fire extinguisher at the door could be necessary if the fire inadvertently spread to the outside of the enclosure. A large yellow information and warning poster regarding electrical safety was placed in a visible location on the experiment as seen in figure 3-21.
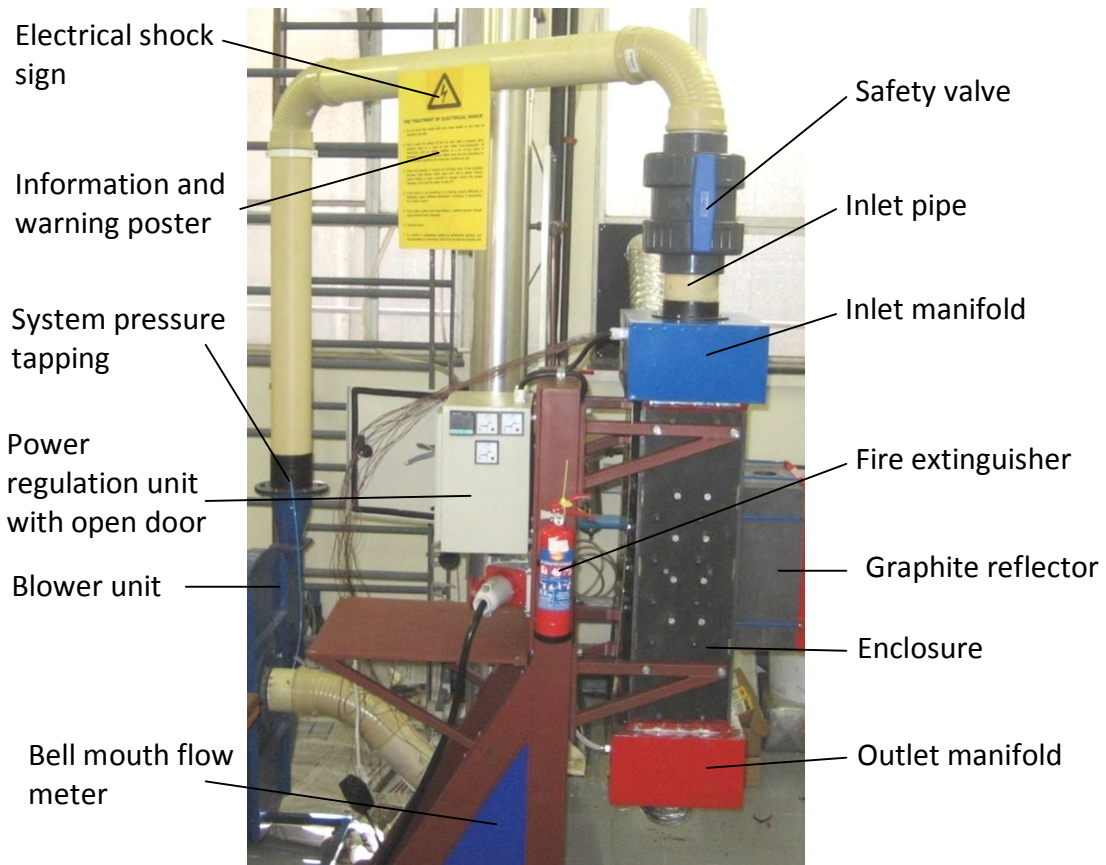
Figure 3-21: Experimental setup showing *inter alia* the fire extinguisher, safety valve and information poster

The inlet and outlet manifold had been painted blue and red as cautionary measures. The blue colour represents cold while the red represents hot. Ear

protection such as earmuffs or earplugs should be worn at all times when conducting an experiment, because of the noise generated by the blower which could lead to hearing loss.

3.6. Instrumentation and measurements

The following sub-sections discuss the equipment that was used and where the measurements were taken.

3.6.1. Data logging equipment

A 34970A Agilent Data Acquisition/ Switch Unit were used as a data logger; see figure 3-22 (a). It makes use of 20-Channel Armature Multiplexer cards as seen in figure 3-22 (b) onto which the thermocouples and pressure transducers where connected. Communication between the Agilent Data Acquisition/ Switch Unit and computer was established using the USB/GPIB Interface USB 2.0 (shown in figure 3-22 (c)).

(a)   (b)   (c)
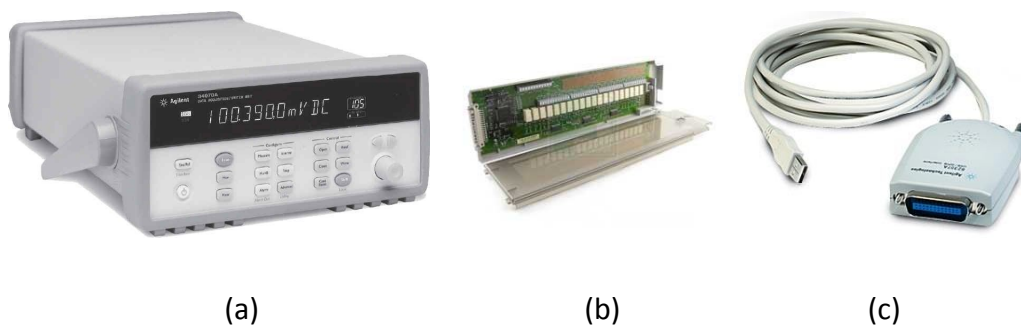
Figure 3-22: (a) Agilent Data Acquisition/ Switch Unit; (b) 20-Channel Armature Multiplexer; (c) USB/GPIB Interface USB 2.0

The Agilent Data Acquisition/ Switch Unit convert the measured thermocouple voltage to a temperature, using a built in static temperature reference. Detailed information regarding the calibration certificates can be found in Appendix C.

3.6.2. Pressure measurements

Pressure measurements were done to measure the differential pressures across the bell mouth flow meter, inlet and outlet manifold, pebble bed and system pressure. See figure 3-4, figure 3-15, figure 3-19 and figure 3-21. A unit was built to measure four individual differential pressures and a schematic drawing of the circuitry is displayed below in figure 3-23. The output of each pressure transducer was filtered with a two-pole low-pass butterworth filter (Neamen, 2001). The cutoff frequency was set at 1 Hz. This creates a constant output signal that does not fluctuate too often, thus making it easier to read a stable pressure.
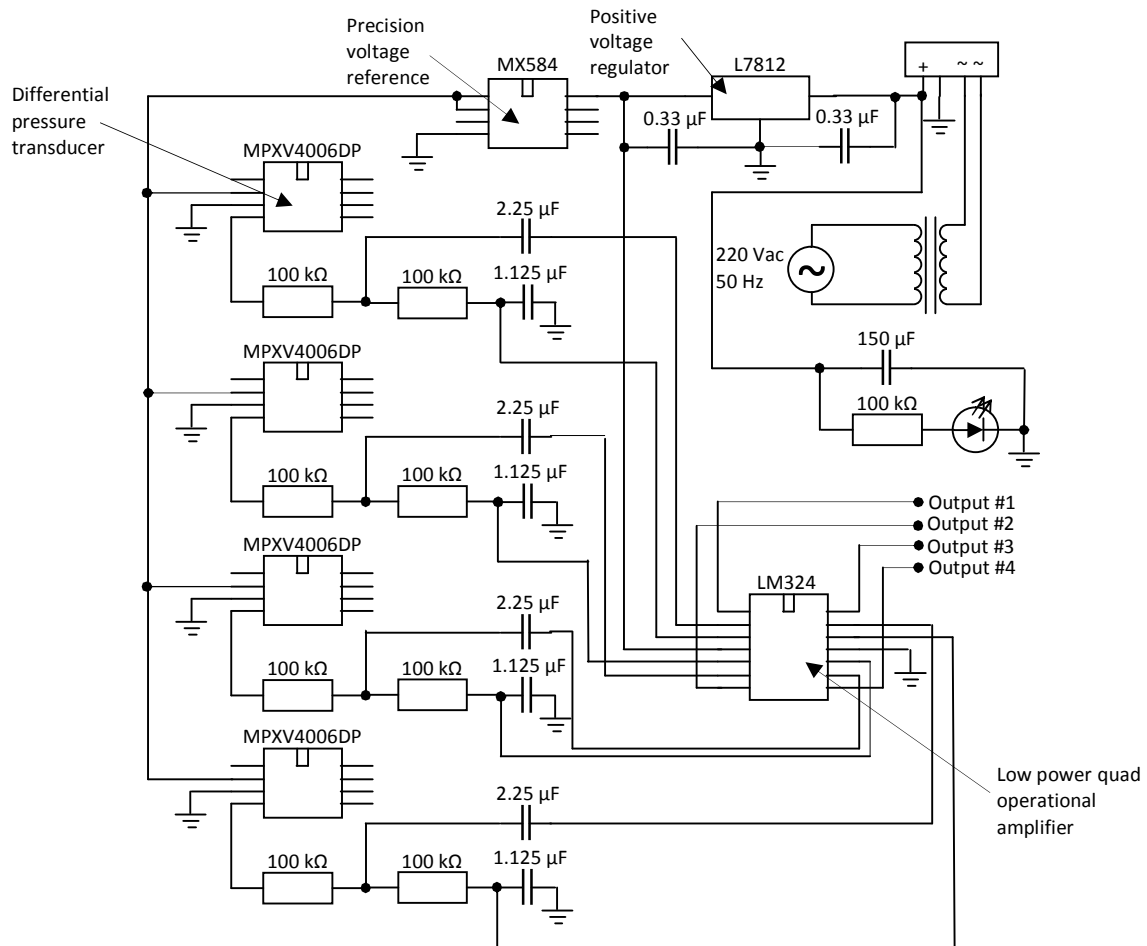
Figure 3-23: Circuit layout for pressure transducers

To calibrate the pressure transducers, pressure measurements was compared with a Betz Micro Manometer as seen in figure 3-24 (a). The calibration data for the pressure transducers is given in Appendix C.
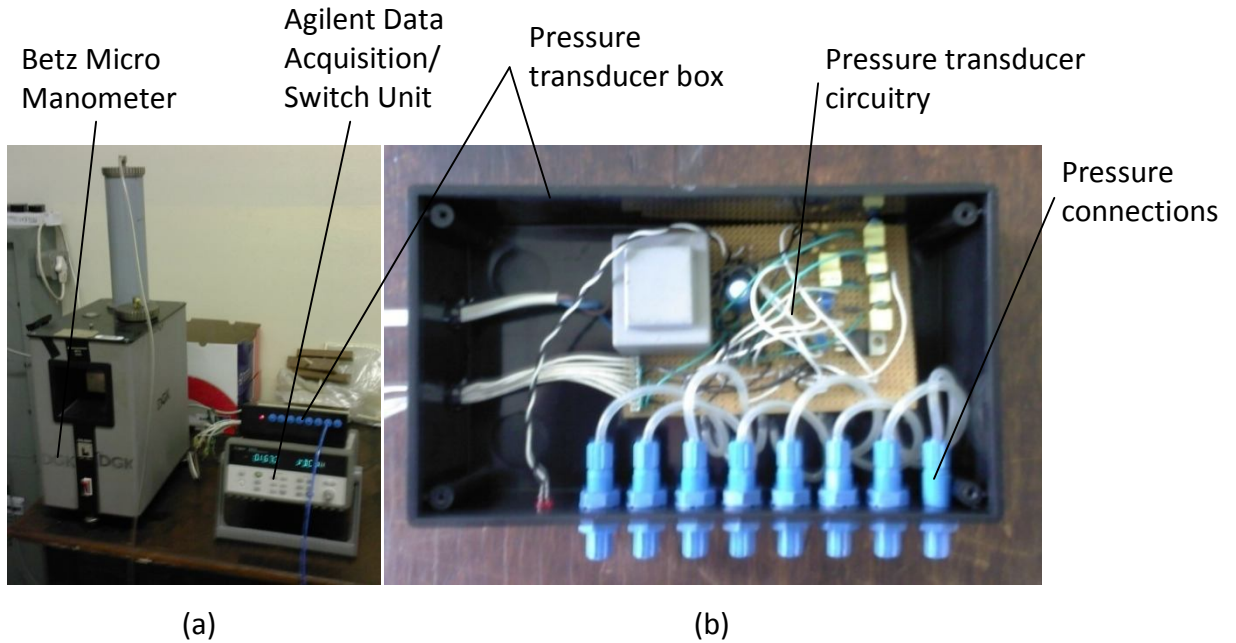
Figure 3-24: (a) Calibration of the pressure transducers; (b) Pressure transducer unit and circuitry

3.6.3. Air flow measurements

A bell mouth as described in section 3.4.2 was used to calculate the air mass flow rate. The temperature of the contracted air was measured along with the differential pressure over the bell mouth which is shown in figure 3-19 (b). The mass flow rate was then determined using equation (3.1). A sample calculation is given in Appendix B and the calibration of the air flow equipment is given in Appendix C.

3.6.4. Temperature measurements

K-type thermocouples were used in measuring the pebble temperatures, the distributed temperatures in the reflector channel, the air inlet temperature at

the bell mouth and the inlet and outlet manifold temperatures. The thermocouple junction was secured by fusing the two wire ends together using a blow torch after which it was calibrated against a platinum resistance thermometer and a uncertainty analysis was conducted. It was found that the average uncertainty of the k-type thermocouples was ± 1.1 °C. The calibration and uncertainty analysis data is given in Appendix C.
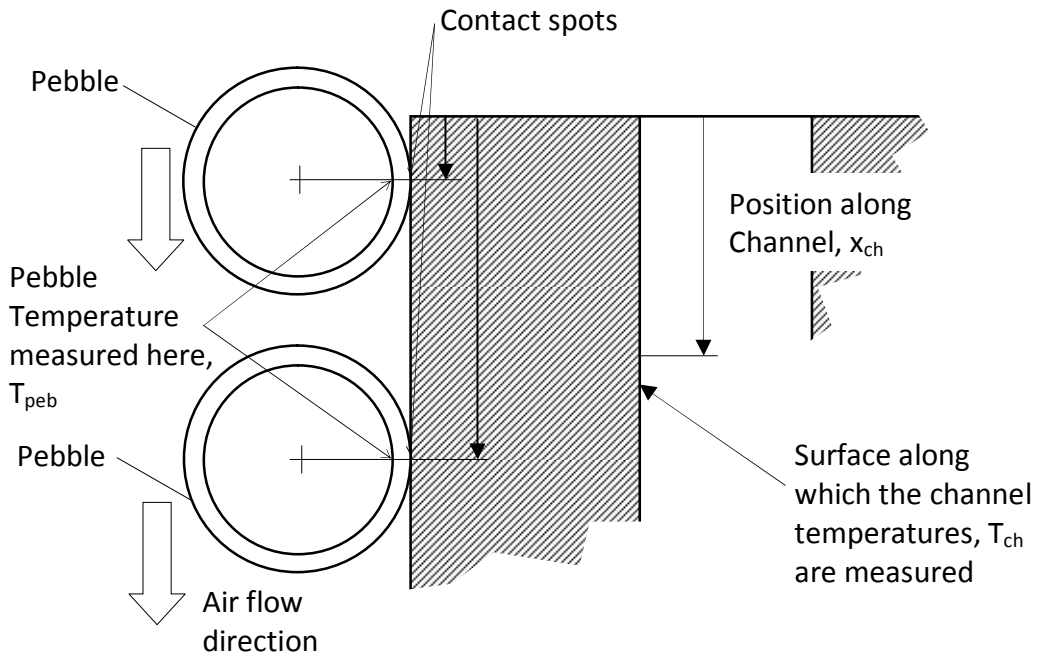
Figure 3-25: Description of pebble and reflector temperature measurements

Figure 3-25 shows where the pebble and reflector channel temperature measurements were located. The device that was built to measure the temperatures along the reflector channel is shown in figure 3-26. To be certain accurate surface temperature measurements were taken on the surface of the reflector channel, a ceramic bead was placed behind the thermocouple for insulation. To ensure that the thermocouple pressed against the reflector surface a spring was placed behind the ceramic bead, applying a constant pressure on the thermocouple, see figure 3-26 (c).
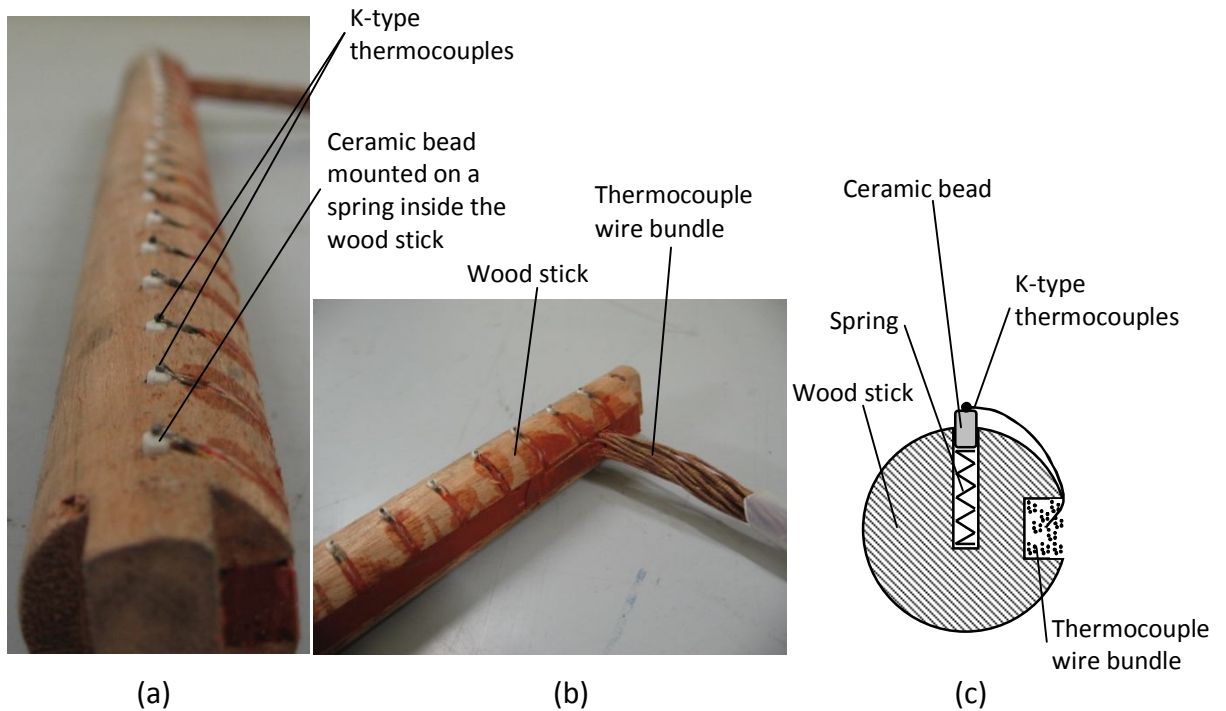
Figure 3-26: Distributed thermocouple measuring device (a) Lower end of the device; (b) Top end of the device; (c) Detail section view of one thermocouple, ceramic bead and spring

3.6.5. Electrical power measurements

To calculate the amount of electrical energy that was consumed by the heaters in the pebbles, the line voltage and line current were measured. The voltage was measured using two different multimeters and their average where used for the calculation. Figure 3-27 shows the Siemens analog amp meter that was used to measure the current. The load is purely resistive, and therefore the power was calculated by multiplying the voltage with the current.

Figure 3-27: Siemens analog Ampere meter

3.6.6. Atmospheric pressure and room temperature readings

A Thies Clima mercury station barometer was used to measure the atmospheric pressure and room temperature. Each reading had to be adjusted to compensate for the elevation above sea level and temperature (ThiesClima, 1985). A sample calculation is given in Appendix B.

3.7. Operational procedures

Adherence to the operational test procedures as given in Appendix F was maintained. This should ensure that experiments are executed in the same manner each time.

4. Numerical modelling

Computational Fluid Dynamics (CFD) Modelling has been chosen to numerically model the flow and temperature distributions in the pebble bed experiment. An overview of the CFD modelling process is displayed in figure 4-1. How it was applied will be further explained throughout the rest of the chapter.
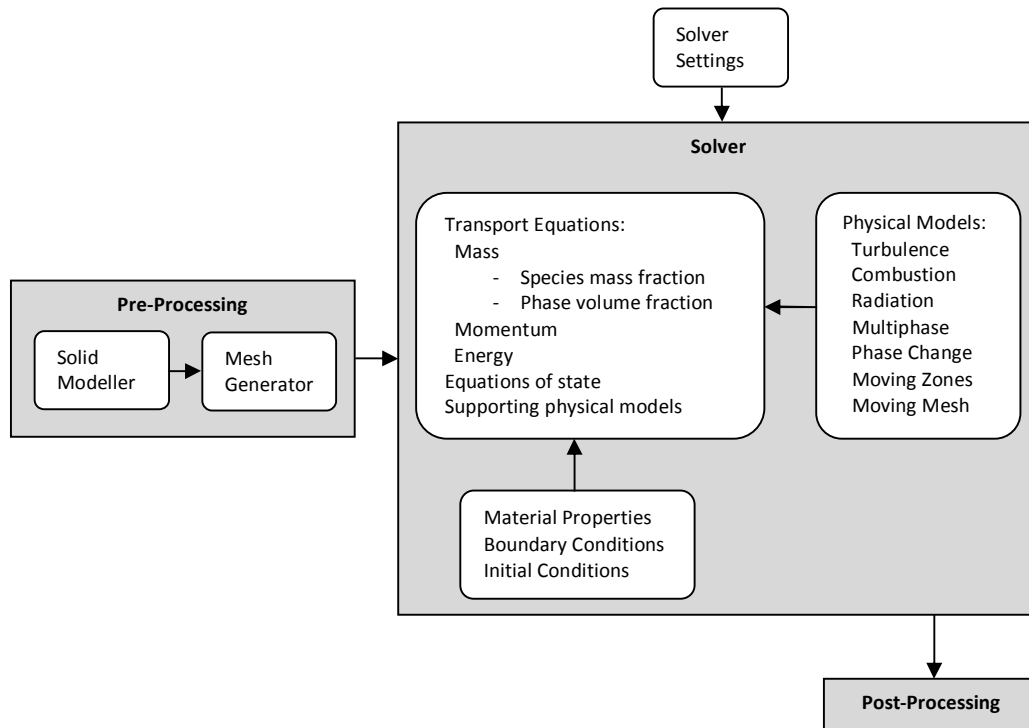
Figure 4-1: CFD modelling overview

GAMBIT (FLUENT, 2006) was used to complete the pre-processing stage. The FLUENT CFD package consist of the remaining two stages, the solver and post-processing as seen in figure 4-1.

Pre-processing consist of the input of the physical problem that needs solving. This involves the definition of the computational domain, grid generation, selection of the physical phenomena that needs to be modeled and continuum and boundary definitions.

The solver is based on the finite volume method. The numerical algorithm consist of the following steps: integration of the governing equations over the domain, discretisation (conversion of the resulting integral equations into a system of algebraic equations) and the solution of the algebraic equations by means of iteration.

Post-processing involves data extraction and processing by creating graphs, particle tracking, surface plots ect. The rest of the chapter deals with these topics regarding settings and features used in FLUENT.

4.1. Governing equations

The governing equations of the continuum represent mathematical statements of the conservation laws of physics. The conservation laws of physics consist of the conservation of mass, net rate of change of momentum equal to sum of the forces on a continuum particle, and net rate of change of energy equal to the sum of the rate of heat addition and the rate of work done on a continuum particle. The governing equation in Cartesian coordinates for conservation of mass for an unsteady and compressible fluid is given as

$$\frac{\partial \rho}{\partial t} + \frac{\partial (\rho u)}{\partial x} + \frac{\partial (\rho v)}{\partial y} + \frac{\partial (\rho w)}{\partial z} = 0 \qquad (4.1)$$

where the first term on the left hand side is the rate of change in time of the density (Versteeg and Malalasekera, 2007). The remaining three terms are convective terms and describes the net flow of mass across the boundaries of the element. The momentum governing equations in three dimensions are written as

x-component: $\qquad \rho \frac{Du}{Dt} = \frac{\partial (-p + \tau_{xx})}{\partial x} + \frac{\partial \tau_{xy}}{\partial y} + \frac{\partial \tau_{zx}}{\partial z} + S_{Mx}$ $\qquad (4.2)$

y-component: $\qquad \rho \frac{Dv}{Dt} = \frac{\partial \tau_{xy}}{\partial x} + \frac{\partial (-p + \tau_{yy})}{\partial y} + \frac{\partial \tau_{zy}}{\partial z} + S_{My}$ $\qquad (4.3)$

z-component:
$$\rho \frac{Du}{Dt} = \frac{\partial \tau_{xz}}{\partial x} + \frac{\partial \tau_{zy}}{\partial y} + \frac{\partial \left(-p + \tau_{zz}\right)}{\partial z} + S_{Mz} \qquad (4.4)$$

The effect of body forces such as gravity is captured in the source terms S_{Mx}, S_{My} and S_{Mz}. From the first law of thermodynamics (Sonntag and Borgnakke, 2001) which states that

Rate of increase of energy of continuum particle		Net rate of heat added to continuum particle		Net rate of work done on continuum particle
	=		+	

and resulting from this, the energy equation can be derived as

$$
\begin{aligned}
\rho \frac{DE}{Dt} = -\mathrm{div}\left(p\vec{u}\right) + &\left[\frac{\partial \left(u\tau_{xx}\right)}{\partial x} + \frac{\partial \left(u\tau_{yx}\right)}{\partial y} + \frac{\partial \left(u\tau_{zx}\right)}{\partial z} \right.\\
&+ \frac{\partial \left(v\tau_{xy}\right)}{\partial x} + \frac{\partial \left(v\tau_{yy}\right)}{\partial y} + \frac{\partial \left(v\tau_{zy}\right)}{\partial z} + \frac{\partial \left(w\tau_{xz}\right)}{\partial x}\\
&\left. + \frac{\partial \left(w\tau_{yz}\right)}{\partial y} + \frac{\partial \left(w\tau_{zz}\right)}{\partial z} \right] + \mathrm{div}\left(k\,\mathrm{grad}\,T\right) + S_E
\end{aligned}
\qquad (4.5)
$$

The left-hand side term is the rate of increase of energy, the first term on the right hand side describes the contribution to energy due to convection and the second term on the right-hand side yields the total rate of work done on the continuum particle by surface stresses. The last two terms on the right-hand side is the rate of heat addition to the continuum particle due to heat conduction and the energy source term respectively. A more conservative form of the governing equations is listed in table 4-1.

Table 4-1: Governing equations of the fluid flow of a compressible Newtonian fluid

Continuity	$\dfrac{\partial \rho}{\partial t} + \mathrm{div}\left(\rho \vec{u}\right) = 0$
x-momentum	$\dfrac{\partial(\rho u)}{\partial t} + \mathrm{div}\left(\rho u \vec{u}\right) = -\dfrac{\partial p}{\partial x} + \mathrm{div}\left(\mu\,\mathrm{grad}\,u\right) + S_{Mx}$
y-momentum	$\dfrac{\partial(\rho v)}{\partial t} + \mathrm{div}\left(\rho v \vec{u}\right) = -\dfrac{\partial p}{\partial y} + \mathrm{div}\left(\mu\,\mathrm{grad}\,v\right) + S_{My}$
z-momentum	$\dfrac{\partial(\rho w)}{\partial t} + \mathrm{div}\left(\rho w \vec{u}\right) = -\dfrac{\partial p}{\partial z} + \mathrm{div}\left(\mu\,\mathrm{grad}\,w\right) + S_{Mz}$
Energy	$\dfrac{\partial(\rho i)}{\partial t} + \mathrm{div}\left(\rho i \vec{u}\right) = -p\,\mathrm{div}\,\vec{u} + \mathrm{div}\left(k\,\mathrm{grad}\,T\right) + \Phi + S_{i}$
Equations of state	$p = \rho R T$ and $i = C_v T$

The dissipation function Φ is defined as follow

$$\Phi = \mu\left\{ 2\left[\left(\frac{\partial u}{\partial x}\right)^2 + \left(\frac{\partial v}{\partial y}\right)^2 + \left(\frac{\partial w}{\partial z}\right)^2\right] + \left(\frac{\partial u}{\partial y} + \frac{\partial v}{\partial x}\right)^2 + \right.$$
$$\left. + \left(\frac{\partial u}{\partial z} + \frac{\partial w}{\partial x}\right)^2 + \left(\frac{\partial v}{\partial z} + \frac{\partial w}{\partial y}\right)^2 \right\} + \lambda\left(\mathrm{div}\,\vec{u}\right)^2$$

(4.6)

If a general variable ϕ is introduced, the conservative governing equations can be written in the following form

$$\frac{\partial(\rho\phi)}{\partial t} + \mathrm{div}\left(\rho\phi\vec{u}\right) = \mathrm{div}\left(\Gamma\,\mathrm{grad}\,\phi\right) + S_{\phi}$$

(4.7)

and is called the transport equation. In words

Rate of increase of ϕ of continuum particle		Net rate of flow of ϕ out of continuum particle		Rate of increase of ϕ due to diffusion		Rate of increase of ϕ due to sources
	+		=		+	

The transport equation illustrates the various transport processes: the rate of change term and convective term on the left-hand side and the diffusion and

source term on the right-hand side. Computational procedures using the finite volume method uses the transport equation as a starting point whereby setting ϕ equal to 1, u, v, w and i and selecting relevant values for the diffusion coefficient, Γ and source terms the transport equation will simplify back to the governing equations as listed in table 4-1.

4.2. Solver

The solver that is used to solve the governing equations, as mentioned in the previous section, makes use of the projecting method algorithm (FLUENT, 2006). In the projection method, the constraint of continuity of the velocity field is achieved by solving a pressure equation. The pressure equation is derived from the continuity and momentum equations in such a way that the velocity field, corrected by the pressure, satisfies continuity. Due to the non-linearity and pressure-velocity coupled governing equations; the solution process involves iterations, where the set of governing equations is solved continually until the solution has converged.

In the solver settings, the velocity formulation was set to absolute. This means that the momentum equations are expressed using the absolute velocities as the dependent variables. An alternative to this is to set the velocity formulation to use the relative velocity as the dependent variable.

Data measurements were taken from the experiment only once thermal equilibrium has been reached. Thus, all numerical cases were computed for a steady state solution.

Gravity was enabled for all numerical models. Due to the design of the experimental equipment, the gravitational acceleration is in the same direction as the bulk fluid flow. This is also the case in the PBMR (Slabber *et al.*, 2006).

4.3. Turbulence model

According to Versteeg and Malalasekera (2007) the Shear Stress Turbulence (SST) k-ω turbulence model is a good general purpose model. Both McLaughlin *et al.* (2008) and In *et al.* (2008) made use of the SST k-ω model to simulate turbulence in packed beds and obtained good numerical results compared with analytical calculations. Due to the popularity of the SST k-ω model to solve strong adverse pressure gradients, flow separation (Menter *et al.*, 2003) and integration to the wall without the requirement of wall-damping functions in low Reynolds applications (Versteeg and Malalasekera, 2007), it was chosen to best simulate the effect of turbulence in the numerical simulations of this study.

The SST k-ω model is based on Wilcox's original k-ω model (Menter, 1994), hence the Reynolds stress computation and the k-equation remains the same. The Reynolds stresses are computed as usual in two-equation models with the Boussinesq expression (Versteeg and Malalasekera, 2007)

$$\tau_{ij} = -\rho \overline{u_i' u_j'} = 2\mu_t S_{ij} - \frac{2}{3}\rho k \delta_{ij} = \mu_t \left(\frac{\partial U_i}{\partial x_j} + \frac{\partial U_j}{\partial x_i} \right) - \frac{2}{3}\rho k \delta_{ij} \tag{4.8}$$

The k- equation is given as

$$\frac{\partial \rho k}{\partial t} + \text{div}\left(\rho k \overline{U} \right) = \text{div}\left[\left(\mu + \frac{\mu_t}{\sigma_k} \right) \text{grad}(k) \right] + P_k - \beta^* \rho k \omega \tag{4.9}$$

Due to shortcomings in the k-ε model, Menter (1994) suggested a hybrid model. Deficiencies such as inadequate performance in the near-wall region when solving boundary layers with adverse pressure gradients led to a model that transforms from the k-ω model to the k-ε model. The ε-equation is transformed into a ω- equation by substituting ε with kω. This yield

$$\frac{\partial \rho \omega}{\partial t} + \mathrm{div}\left(\rho \omega \overline{U}\right) = \mathrm{div}\left[\left(\mu + \frac{\mu_t}{\sigma_{\omega,1}}\right)\mathrm{grad}(\omega)\right]$$

$$+ \gamma_2\left(2\rho S_{ij}.S_{ij} - \frac{2}{3}\rho\omega\frac{\partial U_i}{\partial x_j}\delta_{ij}\right) \qquad (4.10)$$

$$- \beta_2\rho\omega^2 + 2\frac{\rho}{\sigma_{\omega,2}\omega}\frac{\partial k}{\partial x_k}\frac{\partial \omega}{\partial x_k}$$

Comparing to the standard k-ω model (Versteeg and Malalasekera, 2007), the SST k-ω model has an extra term in the ω-equation. The last term in equation (4.10) is the cross-diffusion term and arises from the ε =kω transformation of the k-ε model diffusion term in the ε- equation.

For the inlet and outlet boundaries values for k and ω and zero gradient has to be specified respectively. The most challenging boundary condition to specify is the condition for ω in the free stream, where the turbulence kinetic energy k → 0 and the turbulence frequency ω → 0. Due to this, it is difficult to determine the eddy viscosity as ω → 0. Therefore, a small non-zero value has to be specified for ω. It is unfortunate that the model tends to be dependent on the free stream value of ω (Versteeg and Malalasekera, 2007).

Improvements were made to the model by Menter *et al.* (2003) based on their experience with the model in general purpose applications (Versteeg and Malalasekera, 2007). The improvements include:

- o   Revised model constants, see table 4-2

Table 4-2: Revised SST k-ω turbulence model constants

$\sigma_k = 1.0$	$\sigma_{\omega,1} = 2.0$	$\sigma_{\omega,2} = 1.17$	$\gamma_2 = 0.44$	$\beta_2 = 0.083$	$\beta^* = 0.09$

o Blending functions

Computation of the eddy viscosity using the standard k-ε model in the far field and the transformed k-ε model (SST k-ω model) near the wall results in different values. This difference causes instabilities. To overcome this, a blending function is used. The cross-diffusion term is modified by introducing the blending functions in the equation. Blending functions are also used for the model constants that take the value for C_1 for the original k-ω model and the value C_2 in the transformed k-ε model:

$$C = F_c C_1 + \left(1 - F_c\right) C_2 \tag{4.11}$$

Typically, a blending function $F_c = F_c\left(l_t / y, \text{Re}_y\right)$ is a function of the ratio of turbulence $l_t = \sqrt{k} / \omega$ and distance y to the wall and of a turbulence Reynolds number $\text{Re}_y = y^2 \omega / v$. F_c is chosen such that:

- it is zero at the wall

- it tends to unity in the far field

- and it produces a smooth transition between the k-ε model and the transformed k-ε model, half way between the wall and the edge of the boundary layer. Therefore $F_c \to 0$ as $y^+ > 70$, (Menter, 1994)

Due to the blending functions, the SST k-ω model combines the good near-wall modelling behavior of the k-ω model with the strong and robust behavior of the k-ε model in the far field. The implementation of the blending functions is also numerically stable.

o Limiters

To improve the performance in flows with adverse pressure gradients and wake regions, the eddy viscosity is *limited*. Limiters are also extended to the turbulent kinetic energy production to prevent the build-up of turbulence in stagnation regions.

The limiters are:

$$\mu_t = \frac{a_1 \rho k}{\max(a_1 \omega, SF_2)} \tag{4.12}$$

where $S = \sqrt{2S_{ij}S_{ij}}$, a_1 = constant, F_2 is a blending function and

$$P_k = \min\left(10\beta^* \rho k \omega, 2\mu_t S_{ij}.S_{ij} - \frac{2}{3}\rho k \frac{\partial U_i}{\partial x_j}\delta_{ij}\right) \tag{4.13}$$

4.4. Radiation model

The radiation model implemented in this study is the Discrete Ordinates (DO) radiation model. The discrete ordinates method is based on a discrete representation of the directional variation of the radiative intensity, I. A solution to the radiative transport equation is found by solving the equation of transfer for a set of discrete directions spanning the total solid angle range of 4π. As such, the discrete ordinates method is simply a finite differencing of the directional dependence of the equation of transfer. Integrals over the solid angle are approximated by numerical quadrature, usually Gaussian quadrature (Versteeg and Malalasekera, 2007). The general equation of transfer for an absorbing, emitting, and anisotropically scattering medium is (Modest, 1993):

$$\frac{dI}{ds} = \hat{\mathbf{s}} \cdot \nabla I(\mathbf{r}, \hat{\mathbf{s}}) = \kappa(\mathbf{r})I_b(\mathbf{r}) - \beta(\mathbf{r})I(\mathbf{r}, \hat{\mathbf{s}}) + \frac{\sigma_s(\mathbf{r})}{4\pi}\int_{4\pi}I(\mathbf{r}, \hat{\mathbf{s}}')\Phi(\mathbf{r}, \hat{\mathbf{s}}', \hat{\mathbf{s}})d\Omega' \tag{4.14}$$

Equation (4.14) is valid for a gray medium or, on a spectral basis, for a nongray medium, and is subjected to the boundary condition

$$I(\mathbf{r}_w, \hat{\mathbf{s}}) = \in(\mathbf{r}_w)I_b(\mathbf{r}_w) + \frac{\rho(\mathbf{r}_w)}{\pi}\int_{\hat{\mathbf{n}}\cdot\hat{\mathbf{s}}'<0}I(\mathbf{r}_w, \hat{\mathbf{s}}')|\hat{\mathbf{n}}\cdot\hat{\mathbf{s}}|d\Omega' \tag{4.15}$$

where equation (4.15) have been limited to an enclosure with opaque, diffusely emitting and diffusely reflecting walls. In the discrete ordinate method, equation (4.14) is solved for a set of n different directions $\hat{\mathbf{s}}_i$, where $i = 1, 2, \ldots, n$, and the integrals over direction are replaced by numerical quadrature, that is,

$$\int_{4\pi} f(\hat{\mathbf{s}})d\Omega \simeq \sum_i^n w_i f(\hat{\mathbf{s}}_i) \tag{4.16}$$

where w_i are the quadrature weights associated with the directions $\hat{\mathbf{s}}_i$. Thus equation (4.15) is approximated by a set of n equations

$$\begin{aligned}\hat{\mathbf{s}}_i \cdot \nabla I(\mathbf{r},\hat{\mathbf{s}}_i) &= \kappa(\mathbf{r})I_b(\mathbf{r}) - \beta(\mathbf{r})I(\mathbf{r},\hat{\mathbf{s}}_i) \\ &+ \frac{\sigma_s(\mathbf{r})}{4\pi}\sum_{j=1}^n w_j I(\mathbf{r},\hat{\mathbf{s}}_j)\Phi(\mathbf{r},\hat{\mathbf{s}}_i,\hat{\mathbf{s}}_j)d\Omega', \quad i=1,2,.....,n\end{aligned} \tag{4.17}$$

subject to the boundary conditions

$$I(\mathbf{r}_w,\hat{\mathbf{s}}_i) = \in(\mathbf{r}_w)I_b(\mathbf{r}_w) + \frac{\rho(\mathbf{r}_w)}{\pi}\sum_{\hat{\mathbf{n}}\cdot\hat{\mathbf{s}}_j<0} w_j I(\mathbf{r}_w,\hat{\mathbf{s}}_j)\left|\hat{\mathbf{n}}\cdot\hat{\mathbf{s}}_j\right|, \quad \hat{\mathbf{n}}\cdot\hat{\mathbf{s}}_i > 0 \tag{4.18}$$

The angular ordinates $\hat{\mathbf{s}}_j = \xi\mathbf{i} + \eta\mathbf{j} + \mu\mathbf{k}$ and angular weights w_j are available in Lathrop and Carlson (1965) and Fiveland (1991). Equations (4.17) together with their boundary conditions (4.18) constitute a set of n simultaneous, first-order, linear partial differential equations for the unknown $I_i(\mathbf{r}) = I(\mathbf{r},\hat{\mathbf{s}}_i)$. The solution for the I_i may be found using the solutions method described in section 4.6. Once the intensities have been determined, the desired direction-integrated quantities are readily calculated. The radiative heat flux, inside the medium or at the surface is

$$\mathbf{q}(\mathbf{r}) = \int_{4\pi} I(\mathbf{r},\hat{\mathbf{s}})\hat{\mathbf{s}}d\Omega \simeq \sum_{i=1}^n w_i I_i(\mathbf{r})\hat{\mathbf{s}}_i \tag{4.19}$$

The standard DO method is suitable for Cartesian and axisymmetric geometries, but not directly applicable to non-orthogonal and unstructured grids. Modifications have been done to the DO method that allows it to be used with more complex geometries (Versteeg and Malalasekera, 2007).

4.5. Continuum and boundary types

All cell zones in the CFD model are either defined as a fluid or solid continuum. A fluid zone is a group of cells for which all of the governing equations are solved, whereas for the solid zone only the energy equation is solved.

Boundary conditions specify the flow and thermal variables on the boundaries. Brief descriptions provided by (FLUENT, 2006), of the type of boundaries used in this project are listed below.

- o Mass flow inlet boundary: This condition is used to specify the mass flow rate or mass flux at an inlet boundary. The static pressure is not fixed and is allowed to change to the appropriate value in order to satisfy the inlet condition. However, the turbulence parameters, temperature and flow direction can be changed or specified.

- o Pressure boundary: This type of boundary condition allows for flow in both directions across the boundary. For this boundary, the static pressure at the boundary plane needs to be specified. When outflow across the boundary occurs, field variables are extrapolated from the interior cells. However, when inflow occurs, the flow is assumed normal to the boundary plane. In this instance the temperature and turbulence parameters needs to be specified.

- o Wall boundary: This condition is used to separate the fluid and solid regions. The thermal boundary condition (for heat transfer calculations) regarding the wall boundary could be changed.

- o Symmetry boundary: This boundary condition is implemented where the physical geometry of interest and the expected pattern of flow and/or thermal solution have mirror symmetry. Therefore flow across this boundary is not allowed and it is assumed that the normal velocity and normal gradients for all other field variables are zero.

4.6. Solution methods

The methods and parameters described in the following sub-sections is used by the solver, see figure 4-1, to calculate the solution to the transport equations, equations of state and other supporting physical models that are implemented in the numerical modelling of the experimental pebble bed simulation.

4.6.1. Pressure-velocity coupling

The procedure that was used to calculate the flow field is the SIMPLE algorithm. SIMPLE stands for Semi-Implicit Method for Pressure Linked Equations. The sequence of operations is as follows (Thiart, 2007):

- The momentum equation is solved with guessed pressure field p^* and the velocity field (u^*, v^*, w^*) values. This produces new values for u^*, v^*, w^*.
- Next the pressure correction equation is solved to obtain a value for p'.
- The guessed pressure field p^* is corrected by adding p'.
- Next u', v', w' is calculated from the velocity correction formulas.
- The guessed velocity field u^*, v^*, w^* is corrected by respectively adding u', v', w'.
- Solve the discretization equations for other ϕ's.
- Treat the corrected pressures as a new guessed pressure p^* as with the corrected velocities and repeat the procedure from the second step until the solution has converged.

4.6.2. Discretization scheme

To obtain a second order accuracy the second order upwind scheme was implemented. This scheme uses a multidimensional linear reconstruction approach to calculate the quantities at the cell faces. By introducing a Taylor

series expansion of the cell centered solution about the cell centroid, higher-order accuracy is achieved. Thus when second-order upwind scheme is selected, the face value ϕ_f is computed using the following expression:

$$\phi_{f,SOU} = \phi + \nabla\phi \cdot \vec{r} \tag{4.20}$$

where ϕ and $\nabla\phi$ are the cell-centered value and its gradient in the upstream cell, and $\vec{r}$ is the displacement vector from the upstream cell centroid to the face centroid (Fluent, 2008). This formulation requires the determination of the gradient $\nabla\phi$ in each cell and is limited so that no maxima or minima are introduced. Table 4-3, shows the different variables on which the second order upwind scheme has been applied.

Table 4-3: Discretization schemes

Variable	Scheme
Pressure	Second order
Density	Second order upwind
Momentum	Second order upwind
Turbulent kinetic energy	Second order upwind
Specific dissipation rate	Second order upwind
Energy	Second order upwind
Discrete ordinates	Second order upwind

4.6.3.   Relaxation factors

The convergence rate of point iterative methods depends on the properties of the iteration matrix. In order to improve the convergence rate of these methods a relaxation factor is introduced in the method. By either choosing the relaxation factor between one and zero the procedure is an under-relaxation method, whereas if it is higher than one it is called over-relaxation. Table 4-4 shows the relaxation factors for different variables. These variables are either under-relaxed or not relaxed.

Table 4-4: Relaxation factors

Variable	Relaxation factors
Pressure	0.3
Density	1
Body forces	1
Momentum	0.7
Turbulent kinetic energy	0.8
Specific dissipation rate	0.8
Turbulent viscosity	1
Energy	1
Discrete ordinates	1

4.7.   Judging convergence

Usually the first choice of judging whether a steady state solution has converged is by evaluating the residual reduction. In addition to residual reduction, it is recommended to monitor global balances of conserved variables, such as the mass, momentum and energy against the iteration number. Convergence is monitored and ensured by the following steps (Menter, 2002):

- o   Reduce residuals by a pre-specified level and provide residual plots.
- o   Plot evolution of r.m.s and maximum residual with iteration number.
- o   Report global balances of conserved variables with iteration number.
- o   Plot target variables as a function of iteration number or residual level.
- o   Report target variables as a function of r.m.s residual.

These guidelines are used to evaluate the convergence of the numerical modelling cases. The following sections explain the residual levels and the variables used to evaluate a converged solution.

4.7.1.   Residuals monitors for the transport equations

All the transport equations residual monitor's absolute criteria were set to 1×10^{-6}. These residuals represent the normalized summation of the absolute

error for the transport equations. The residuals never reached this criteria and the convergence was judged by evaluating the surface target variables.

4.7.2. Surface target variables

In accordance with the general guidelines given by (Menter, 2002) the target variables are chosen such that:

- o They should be representative of the goals of the simulation.
- o They have to be sensitive to numerical treatment and resolution.
- o They should be computed with the existing post-processing tools.
- o They should be computed inside the solver and displayed during *run-time*.

The surface target variables used in evaluating convergence are shown in table 4-5. They were chosen to represent the areas of the model that is most likely to take the longest to converge. The time that it takes for the solution to converge is dependent on criteria such as the thermal inertia and un-steady flow patterns.

Table 4-5: Surface target variables

Position	Variable	Integral method
Outlet	Static temperature	Area-weighted average
Inside pebble shell	Static temperature	Area-weighted average
Reflector channel	Static temperature	Area-weighted average
Inlet	Static pressure	Area-weighted average
Pebble surface	Static temperature	Area-weighted average
Pressure drop over manifolds	Static pressure	Area-weighted average
Pressure drop over pebbles	Static pressure	Area-weighted average

4.8. Solution sensitivity

Versteeg and Malalasekera (2007) state that the discretisation errors can be minimized by either decreasing the time step or the space mesh size. This

however increases the computing time and memory usage. Therefore, it is up to the CFD user to determine the lowest achievable level of the numerical error by exploiting resource constraints and simplified profile assumptions.

Due to the complex and large modelling domain, it was not possible to generate various space mesh sizes to test for grid independence. To test that the mesh used showed some form of independence, an evaluation was done between first and second order discretisation schemes of the polyhedral converted mesh. A second evaluation between the polyhedral converted mesh and tetrahedral mesh was done. The results and discussions of these evaluations can be found in sub-section 6.2.1.

5. Numerical setup

The numerical setup's pre-processing (see figure 4-1) was started by constructing the geometry in Gambit 2.4. Thereafter the geometry was meshed, after which all the necessary boundary conditions were applied. The following sections will elaborate more on the individual steps.

5.1. Geometry

The geometry for the numerical setup was constructed using the dimensions of the experimental setup. The experimental setup had a symmetry plane and therefore the geometry was only constructed for the one half. This contributed to the reduction of the total number of cells used. Figure 5-1 shows the symmetry plane and geometry.

The inlet and outlet manifolds, steel enclosure, connecting rods, graphite reflector and electrically heated graphite pebbles in the experimental setup were modeled. It is, however, difficult to include all the components of the experimental setup, therefore some simplification was done to the pebbles, connecting rods and connections between the pebbles, the thermal insulation and inlet and outlet piping. The only geometry of the pebbles that was modeled was the 5 mm graphite shell and the protruding ceramic cluster tube. The thermal insulation was omitted, but an appropriate boundary condition was applied. To simplify the inlet and outlet piping leading towards the inlet and outlet manifolds, a small vertical section was used to model the air flowing into and out of the manifolds. The connecting rods were modeled as a solid ceramic rod and the brass connecting sleeves were omitted.
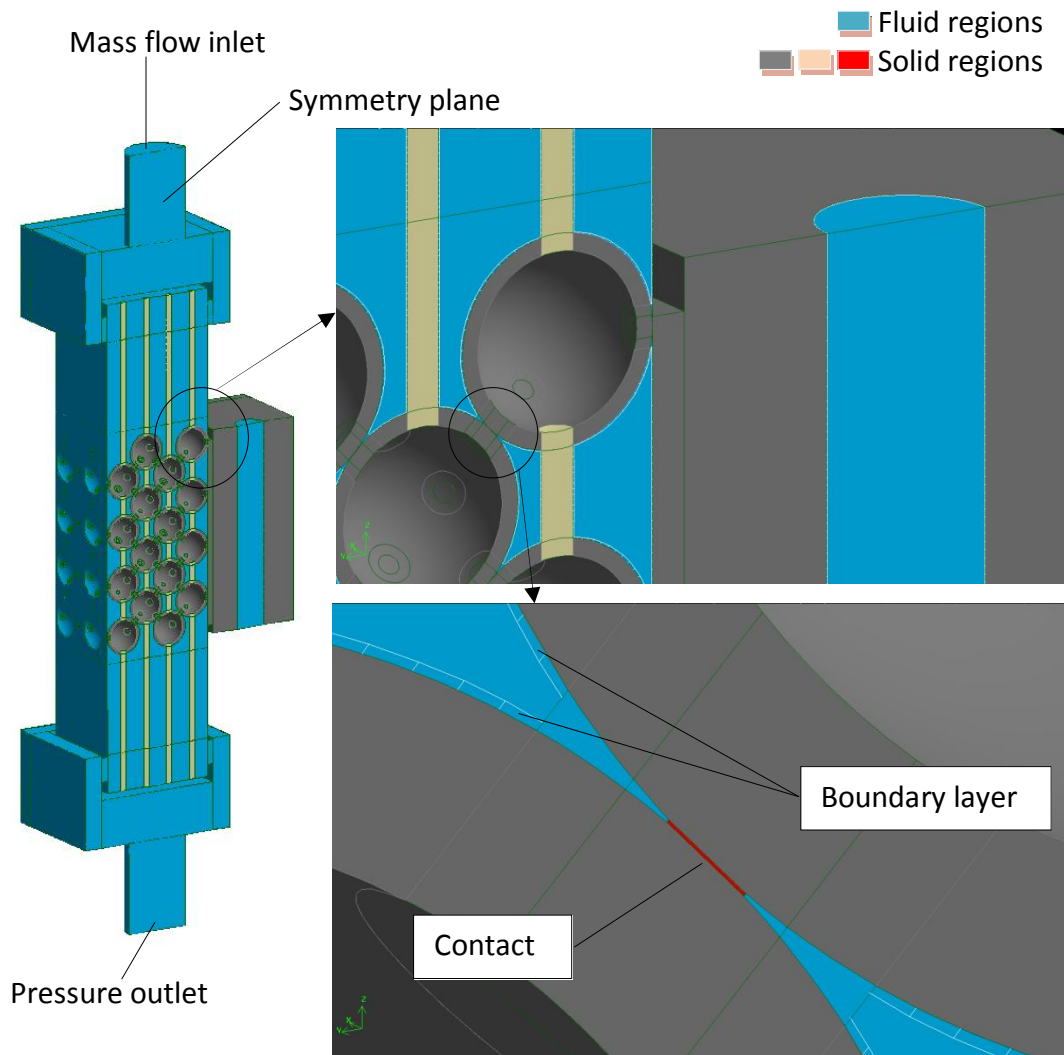
Figure 5-1: Image of the geometry used in the numerical model

The pebble thermal contact area was modeled by creating a cylindrical disc, 3 mm x 0.075 mm thick between the two pebbles in contact, see figure 5-2. Figure 5-3 shows the pebble thermal contact that is located on the symmetry plane.
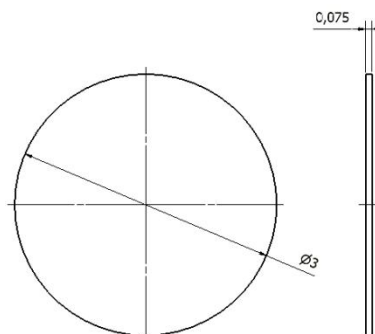
Figure 5-2: Schematic drawing of the pebble thermal contact
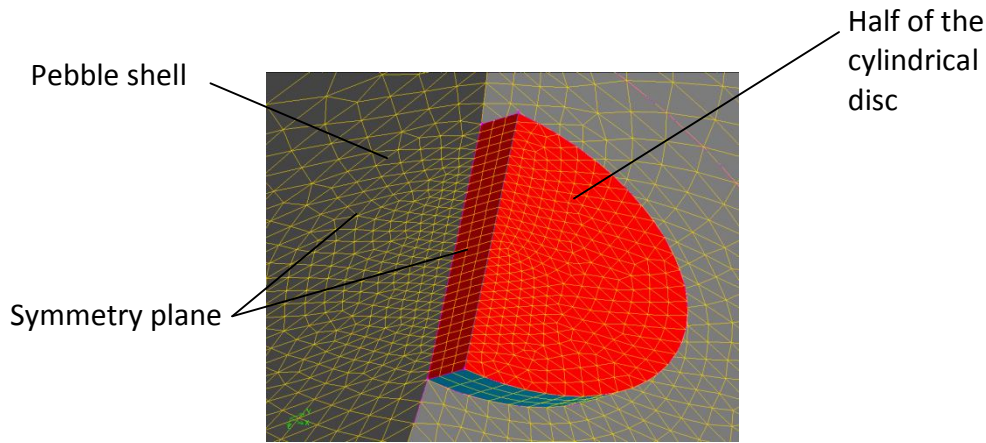
Figure 5-3: Pebble thermal contact area, which is located on the symmetry plane

5.2.   Mesh

The meshing approach that was used was to generate a tetrahedral mesh and then convert it to a polyhedral mesh. By doing this conversion, the cell count is reduced by a factor of three. Table 5-1 shows the mesh parameters for the tetrahedral mesh and the polyhedral mesh.

Table 5-1: Mesh parameters

Mesh parameters	Tetrahedral mesh	Polyhedral converted mesh
Cells	38754837	11686211
Faces	82222908	63774493
Nodes	9230292	50786604
Partitions	1	1
Cell zones	11	11
Face zones	60	60
Maximum cell squish	9.67215×10^{-1}	9.64217×10^{-1}
Maximum cell skewness	9.99998×10^{-1}	9.45618×10^{-1}
Maximum aspect ratio	2.02537×10^{2}	1.44117×10^{2}

A difficult problem was encountered whilst trying to mesh the pebble thermal contact cylinder and the surrounding fluid and solid volumes. Due to the sharp angle geometry near the contact region, highly skewed tetrahedral elements are created. A method to solve these highly skewed tetrahedral elements is to reduce the mesh size. This is not very practical as the number of cells rapidly increase. McLaughlin *et al.* (2008) and Lee *et al.* (2007) both had the same problems generating a mesh in this confined space. To overcome this problem

two *grow-volumes* was created in the pebble shell and fluid region along with the contact volume. This allows the cells to rapidly grow to an acceptable size and also limiting the number of cells used in the overall mesh, see figure 5-4 and figure 5-5.

(a)

(b)
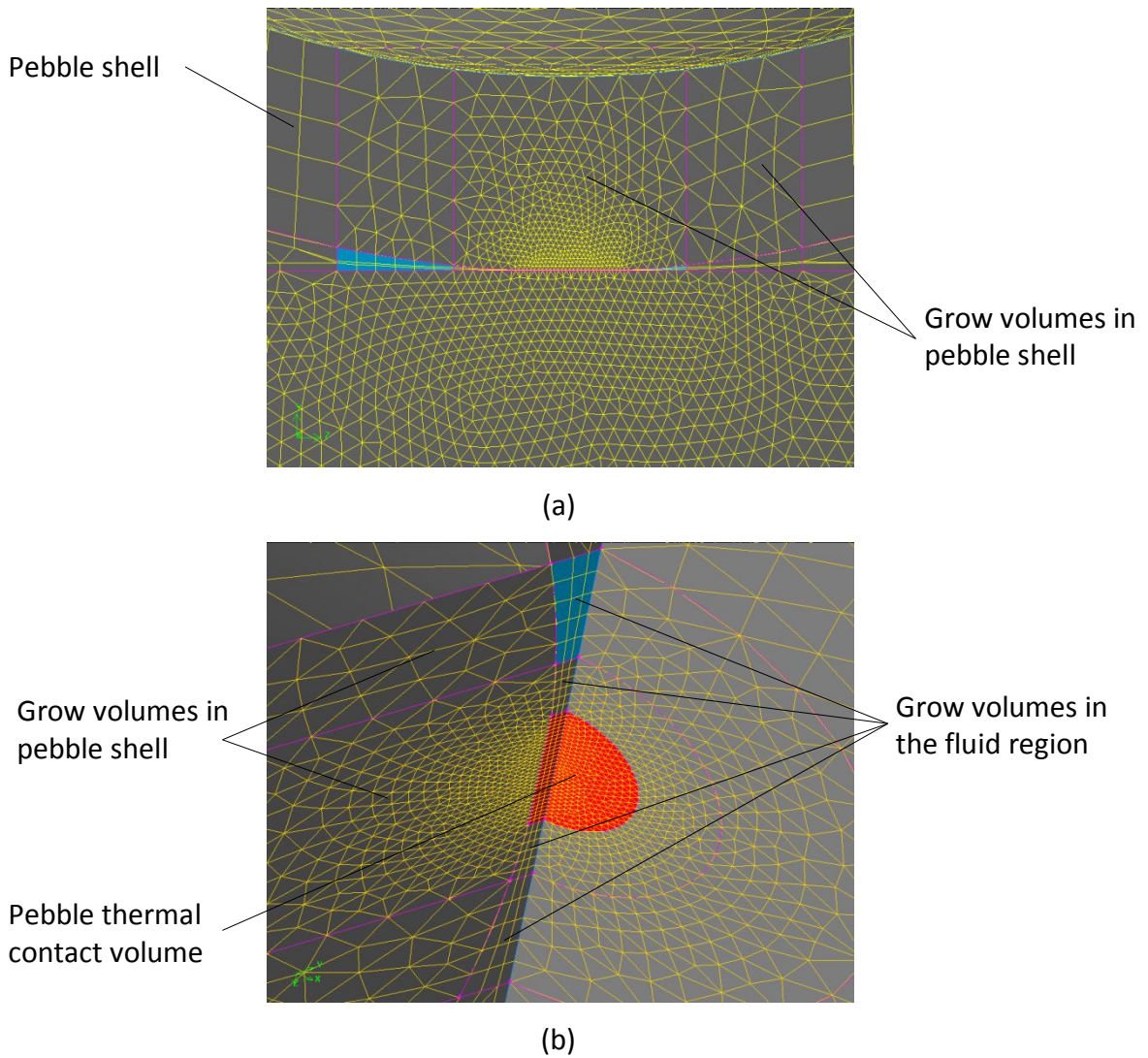
Figure 5-4: Pebble thermal contact and surrounding mesh volumes showing (a) side view and (b) detail view

Single boundary layer on pebble surface and walls

Tetrahedral mesh growing from a structured mesh
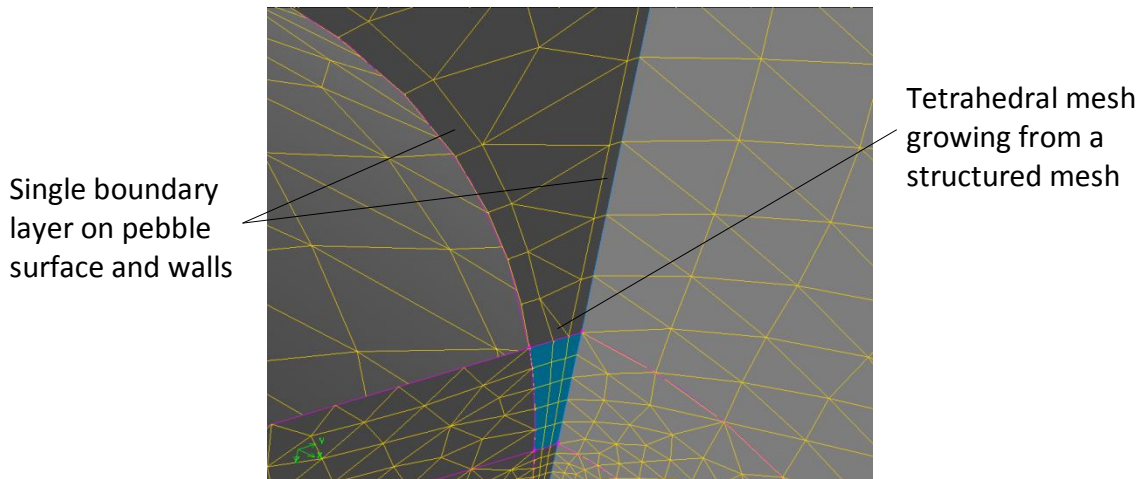
Figure 5-5: Pebble thermal contact and surrounding mesh volumes showing boundary layer and mesh growth

A boundary layer was placed on the pebble surfaces, connecting rods, the inner walls of the model and the reflector inspection channel, see figure 5-1 and figure 5-5. Figure 5-6 shows the polyhedral converted mesh.
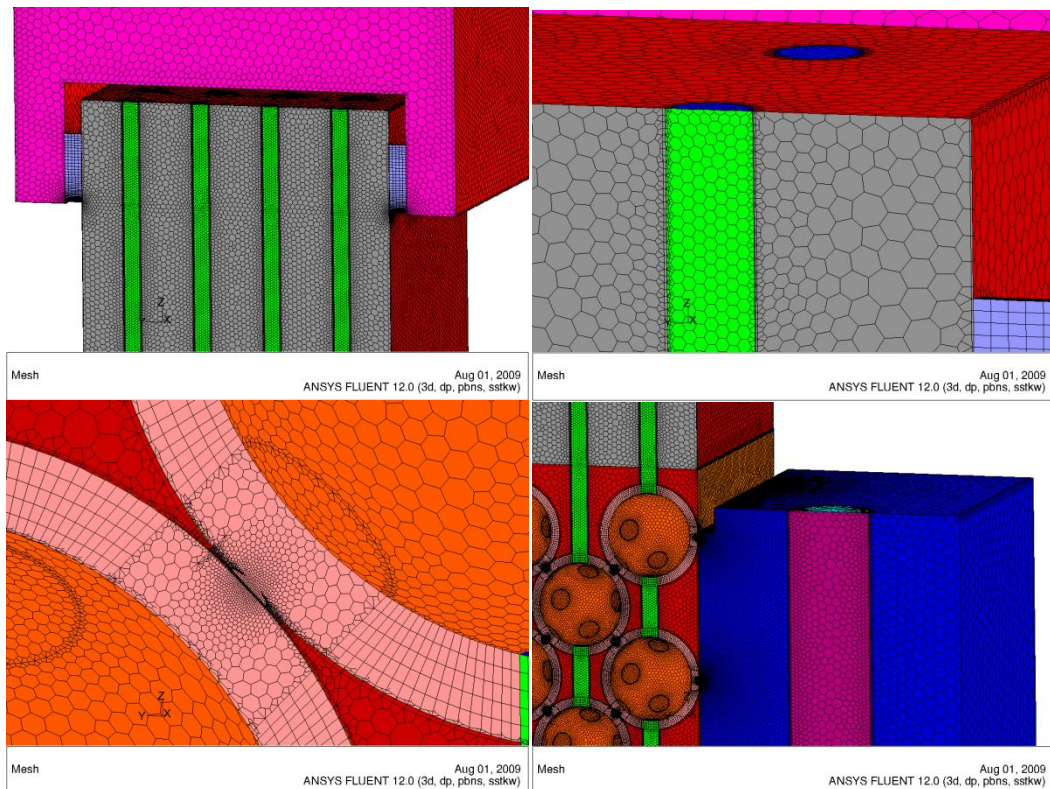
Figure 5-6: Polyhedral mesh

5.3. Continuum and boundary conditions

The continuum properties for the various fluid and solid volumes was selected in accordance with the experimental setup. The material properties for the fluid and solid continuums can be found in Appendix A.

In the numerical setup, the thermal heat loss through conduction from the enclosure and the insulation to the outside has been omitted. To compensate for this a perfect insulated boundary condition was applied to all the walls in the numerical setup.

6. Experimental and numerical results

The experimental and numerical results are given and explained in this chapter. First, the experimental results are given followed by the numerical results, after which the experimental results are compared with the numerical results.

6.1. Experimental results

The experimental results for the pebble thermal contact area experiment and the energy balance for the electrically heated graphite pebble bed is given below.

6.1.1. Pebble thermal contact area

Each graphite imprint, see figure 3-2, was measured after the pebble thermal contact area experiment as described in section 3.1. The results were plotted and figure 6-1 show the pebble thermal contact area diameter versus the applied force. A least squares quadratic equation was fitted through the data.

It could be expected that the contact diameter needs to go through zero. Polson's (2009) calculation of the contact diameter is also based on the principal that if no force is applied the diameter will be zero. This is, however, not evident in the results displayed in figure 6-1. A possible explanation why the experimental results do not go through zero could be provided by adhesion forces between elastic bodies and surface roughness (Johnson, 1989). A contact force of 113 N, which has the highest occurrence in the pebble bed reactor (Polson, 2009) has been used to calculate the contact diameter using the quadratic equation shown in figure 6-1. This calculates to a diameter of 3.4 mm. A diameter of 3 mm was therefore used in the numerical modelling as a reasonable average pebble thermal contact area in a PBMR.
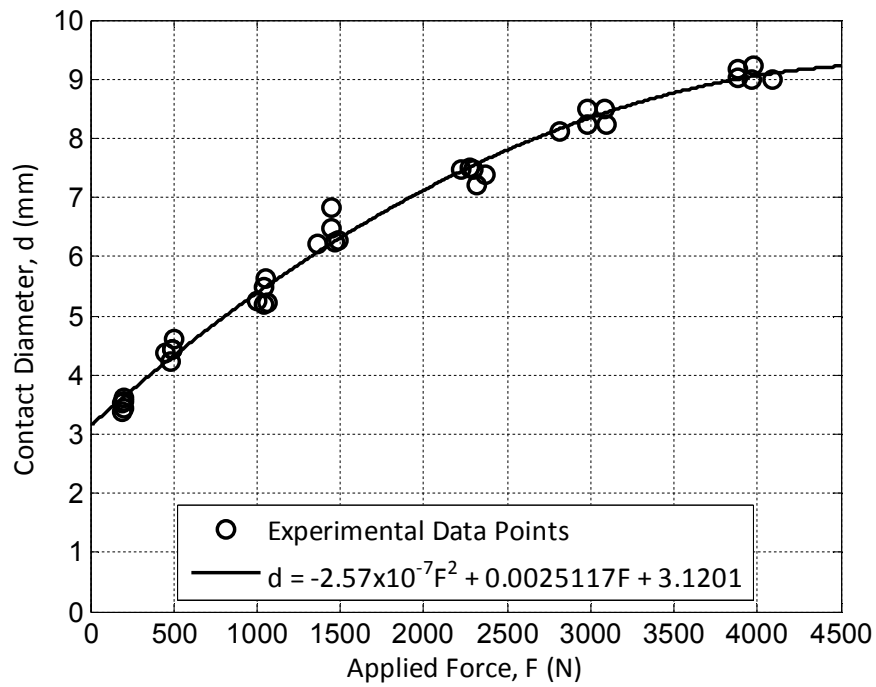
Figure 6-1: Pebble thermal contact area diameter versus the applied force

6.1.2. Energy balance

An energy balance was calculated between the electrical power supplied to the pebbles, the amount of heat energy that was transferred to the air and the energy that was lost to the environment. The experiment was thermally insulated and it is expected that there should only be a small amount of heat loss to the environment. The energy balance for all of the heated pebble bed experiments was calculated and it was found that on average, 2.47 % of the energy was lost to the environment as shown in figure 6-2.
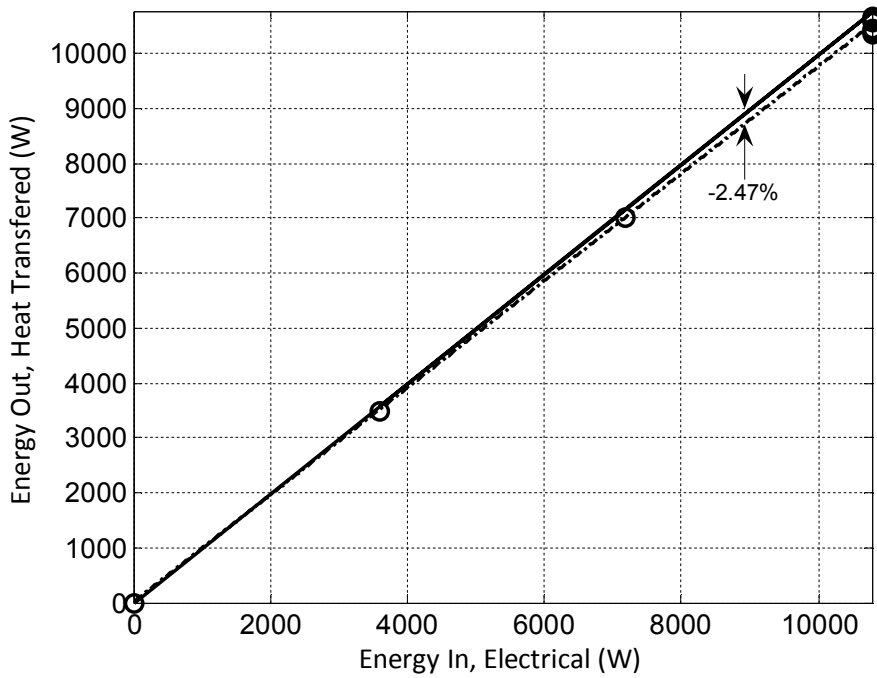
Figure 6-2: Energy balance for experiments

6.2. Numerical results

The numerical results for the mesh independence study and the sensitivity analysis for the pebble contact region is given in the following sections.

6.2.1. Mesh independence

Generally, a mesh independence study is the progressive refinement of an initially coarse mesh until certain key results do not change. To test that near mesh independent results were obtained, results based on a second order discretization scheme on the tetrahedral mesh were compared with results based on first and second order discretization schemes on the polyhedral converted mesh. The parameters that was use for the test are as follow; the air mass flow rate was 0.28572 kg/s and the atmospheric pressure and air inlet temperature was 100730.2 Pa and 16.5 °C.

To calculate the average difference between the channel temperatures, see figure 6-3, the following equation is defined:

$$\text{Difference (\%)} = \frac{\sum\limits_{i=1}^{n}\left(\frac{\left|T_{higher}^{i} - T_{lower}^{i}\right|}{T_{higher}^{i}}\right)}{n} \times 100 \qquad (6.1)$$

Using equation (6.1), the average percentage difference between temperatures computed based on first order discretization on the polyhedral mesh and second order discretization on the tetrahedral mesh amounts to 2.27 %. The average percentage difference between temperatures computed based on first and second order discretiztion on the polyhedral mesh was calculated as 1.32 %. Both these average differences are significantly low and therefore the results are considered mesh independent.
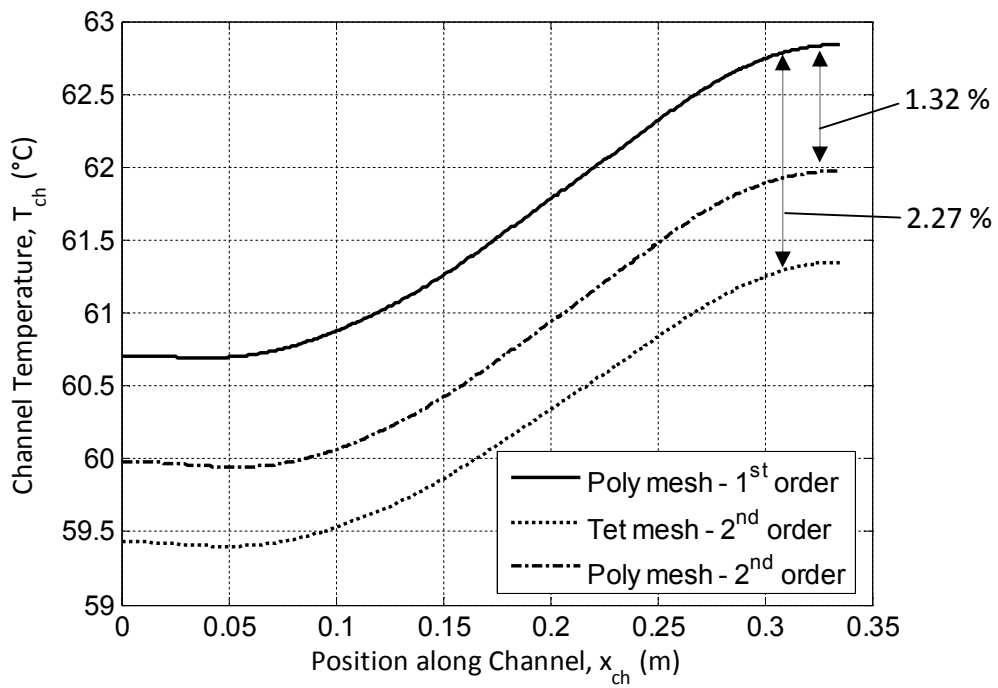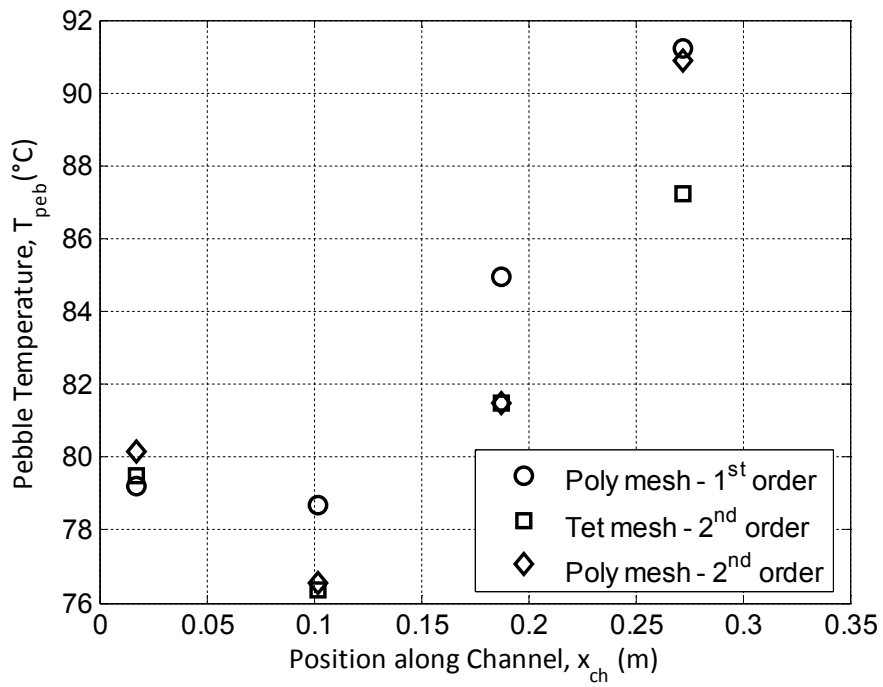
Figure 6-3: Mesh independence test results

6.2.2. Sensitivity analysis for contact region

A sensitivity analysis for the contact region was done to investigate the effect of the thermal contact resistance. It involved, firstly, simply equating the effective thermal conductivity of the pebble thermal contact volume to that of graphite, and, secondly, utilizing the contact resistance as explained in section 2.4. After these two tests, a third test, whereby the pebble thermal contact volume was considered to be air, was undertaken. Due to the low conductivity 0.025 W/mK at 293 K of air, this case essentially simulated no contact between the pebbles. The parameters that were use for the analysis are as follow; the air mass flow rate was 0.28572 kg/s and the atmospheric pressure and air inlet temperature was 100730.2 Pa and 16.5 °C.

Figure 6-4 show the pebble and reflector channel temperatures for the three different contact cases and an experimental test. Using equation (6.1), an average percentage temperature difference of 0.11 % calculated between the graphite contact and the higher resistance contact could be considered negligible. There is, however, a big difference between the contact and no-contact simulation. The average percentage temperature difference in this case was calculated to be 32.04 %. Less heat is conducted away from the pebble, thus raising the pebble temperature and lowering the reflector temperature.

Pebble and reflector channel temperatures measured in the experiment are lower than that of the CFD temperatures, see figure 6-4. This is caused by the insulation boundary condition that was applied to the walls in the CFD model. In the experiment, heat was lost to the environment, thus lowering the pebble and reflector temperatures. In the CFD model, no heat was lost and therefore the pebble and reflector temperatures are higher.
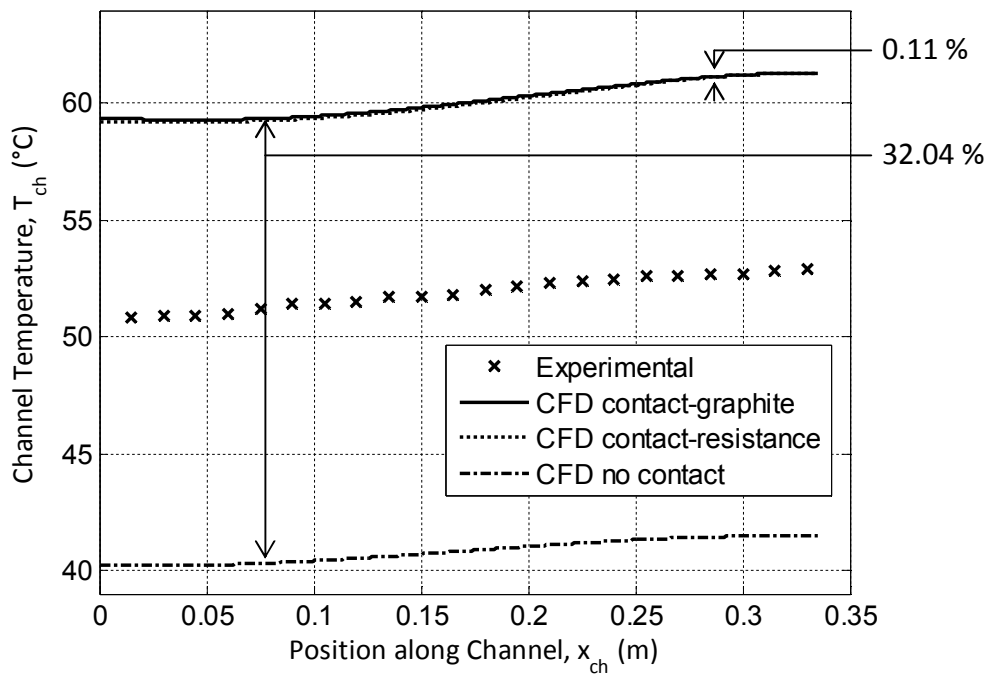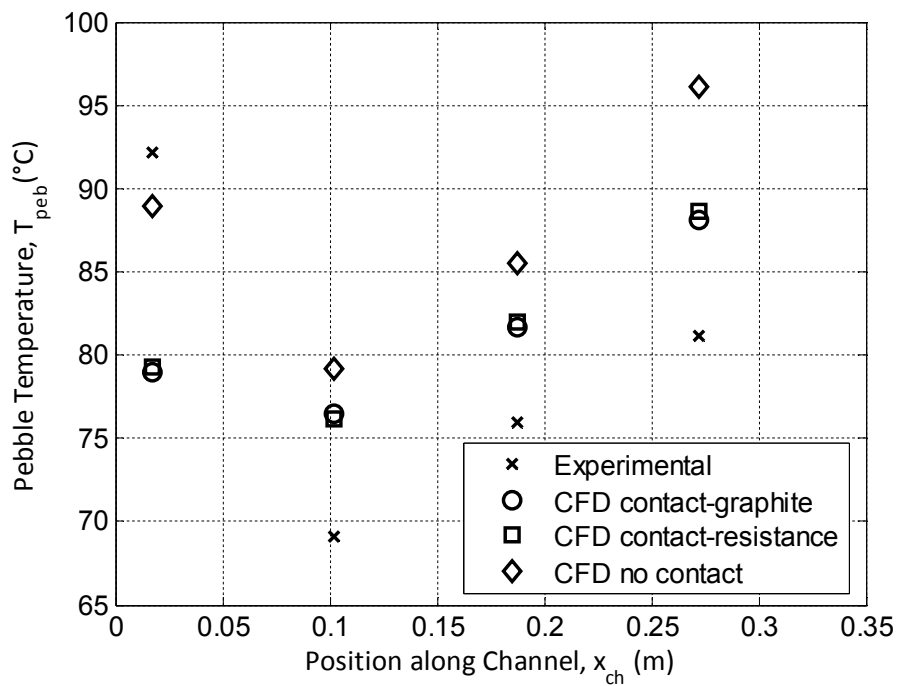
Figure 6-4: Sensitivity for contact region

6.3. Comparison between experimental and numerical results

A comparison between measured values in the electrically heated pebble bed experiment tests and the CFD simulation results are given for differential pressure drop evaluations, different mass flow rate and pebble heating tests.

6.3.1. Pressure measurements

The differential pressure for the bell mouth and system pressure was measured relative to atmosphere, see figure 3-19 and figure 3-21. The differential pressure for the manifolds and pebble bed were measured between two points on the pebble bed experiment, see figure 3-4 and figure 3-15. Figure 6-5 shows the differential pressure versus the air mass flow rate. The pebbles were not heated for this experiment. The atmospheric pressure was 99984.8 Pa and air inlet temperature was 17 °C.
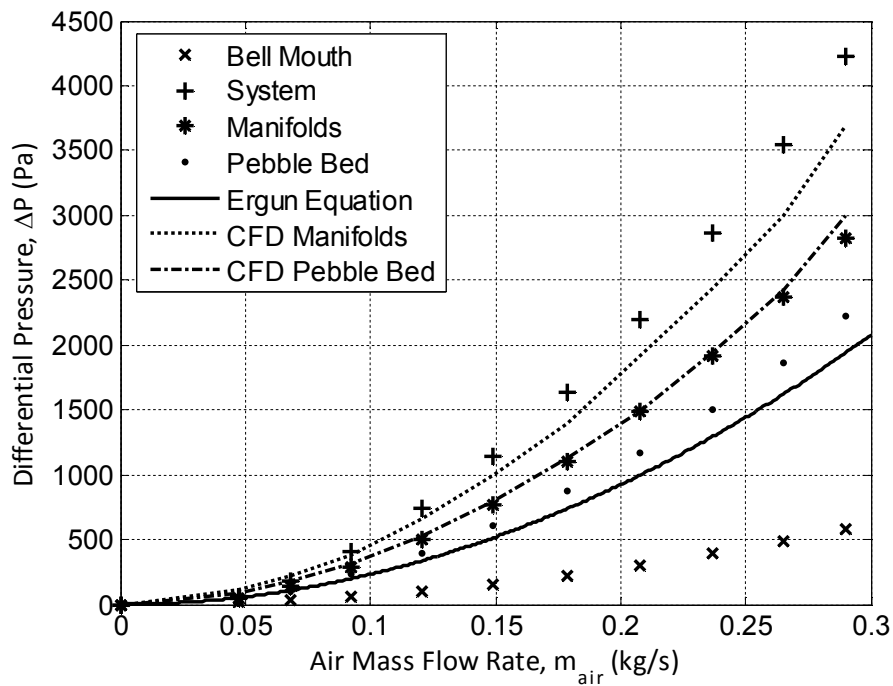
Figure 6-5: Pressure measurements

The calculated differential pressure across the pebble bed using the Ergun equation under predicted the CFD and experimental data. The CFD results over predicted the experimental values.

6.3.2. Sensitivity analysis for mass flow rate

An analysis was done to see how the mass flow rate affects the temperature measured in the reflector channel and the pebbles. The pebble and reflector channel temperatures for different air mass flow rates are seen in figure 6-6. The room temperature was 15 ± 1 °C with the atmospheric pressure at 101472.4 ± 654.3 Pa.
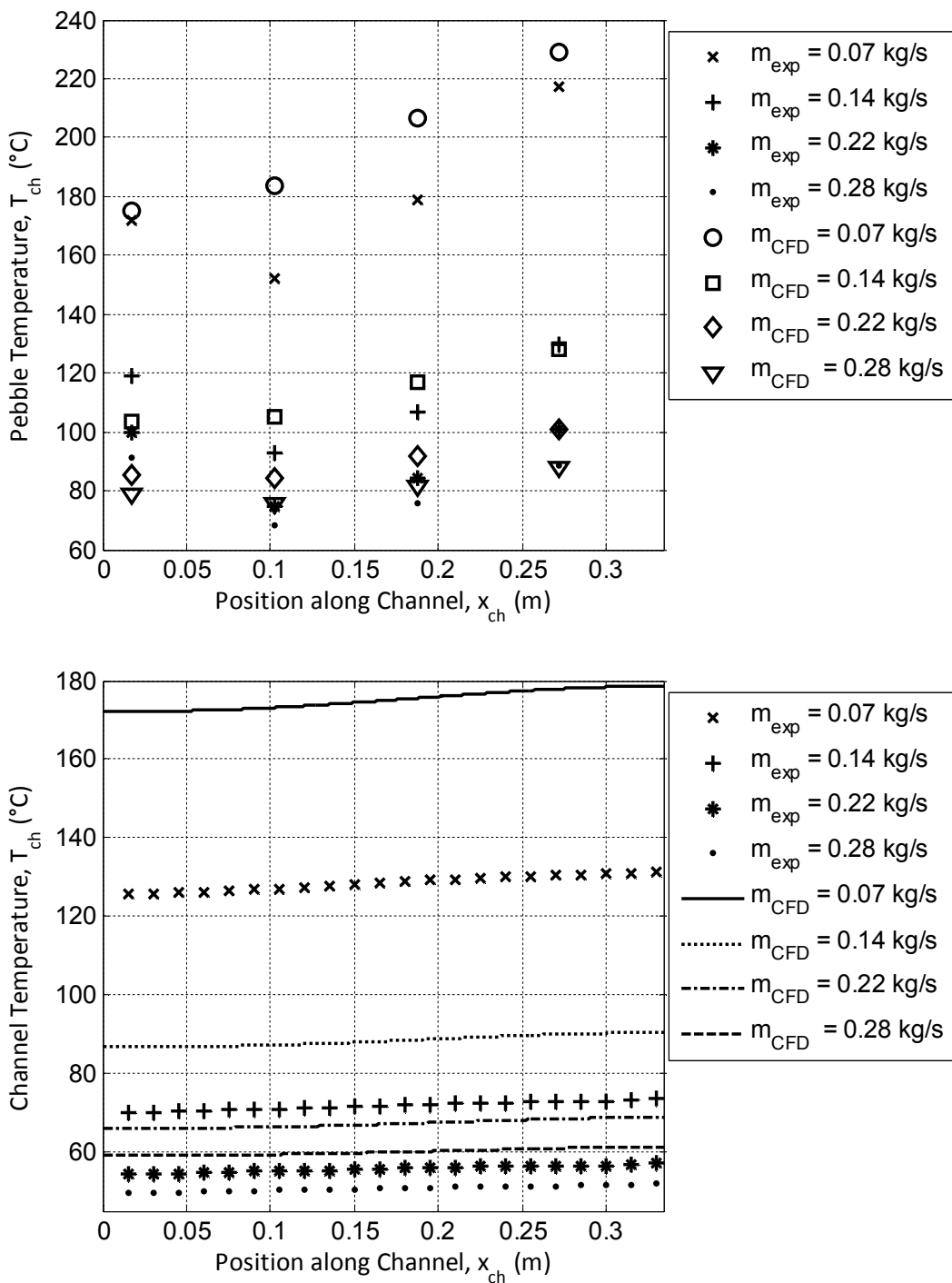
Figure 6-6: Sensitivity analysis for mass flow rates

The experimental measurements compare well with the CFD results for the pebble temperatures. There is, however, a larger temperature difference between the channel temperatures, especially at higher temperature. This is

caused by the perfect insulation boundary condition that was applied in the CFD simulation to the walls of the pebble bed experiment.

6.3.3. Sensitivity analysis for pebble heating

A sensitivity analysis for pebble heating was done by change the electrical power that is supplied to the pebbles. The air mass flow rate was held constant at 0.28417 kg/s. The room temperature was 15.75 ± 0.25 °C and the atmospheric pressure 100882 ± 35.75 Pa. The pebble temperatures obtain through CFD simulation matched the experimental measurements quite close as can be seen in figure 6-7.
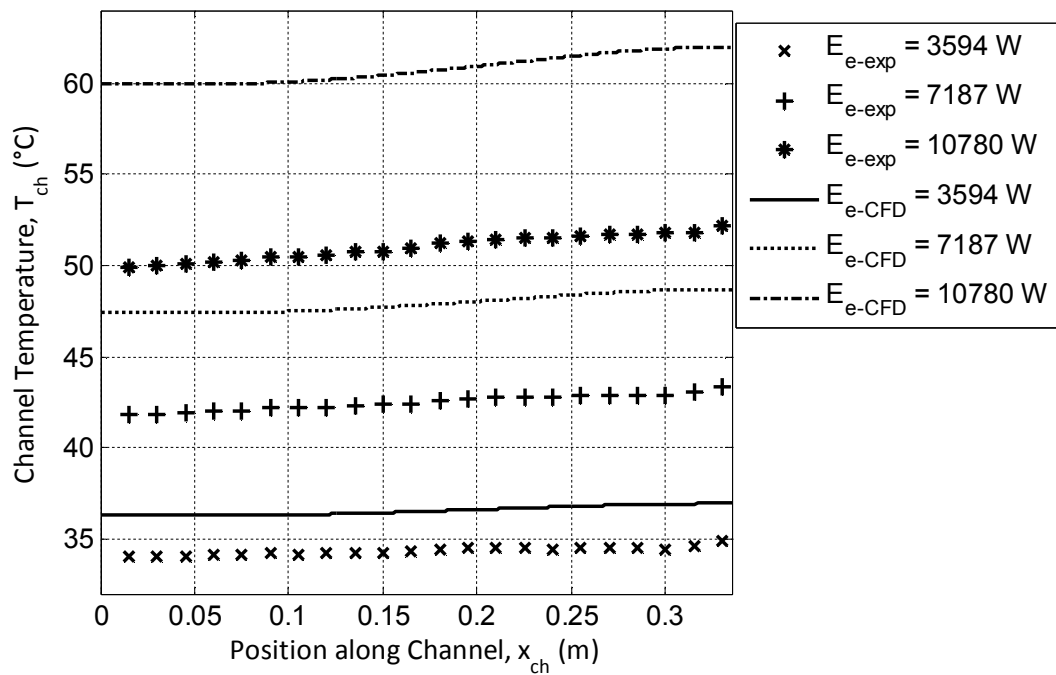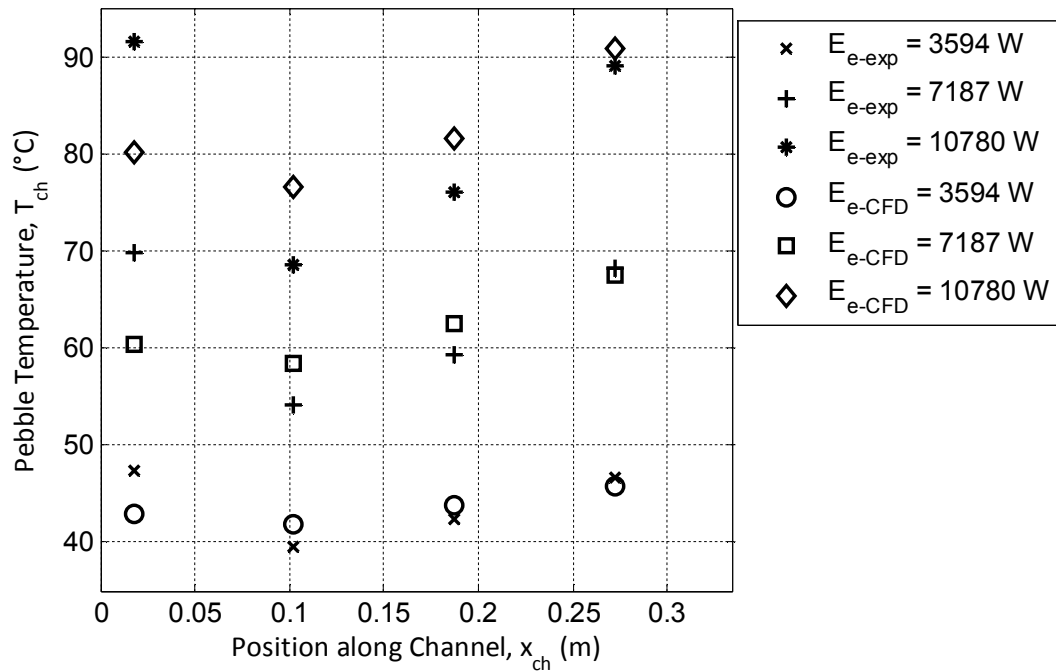
Figure 6-7: Sensitivity for pebble heating

6.3.4. Difference with inspection channel closer to pebble bed

In the previous test the temperature measured in the reflector channel did not deliver the expected temperature peaks on the temperature profile along the inspection channel. It was therefore suggested that the reflector channel be moved closer to the pebbles in order to determine if it was indeed possible to measure the temperature fluctuations. The channel was moved to a point 10 mm away from the pebbles and the results are seen in figure 6-8 in comparison with the normal setup (channel 80 mm away from the pebbles). The results show the temperature peaks on the temperature profile where the pebbles are in contact with the reflector wall. The parameters that were use for the analysis are as follow; the air mass flow rate was 0.28572 kg/s and the atmospheric pressure and air inlet temperature was 100730.2 Pa and 16.5 °C.
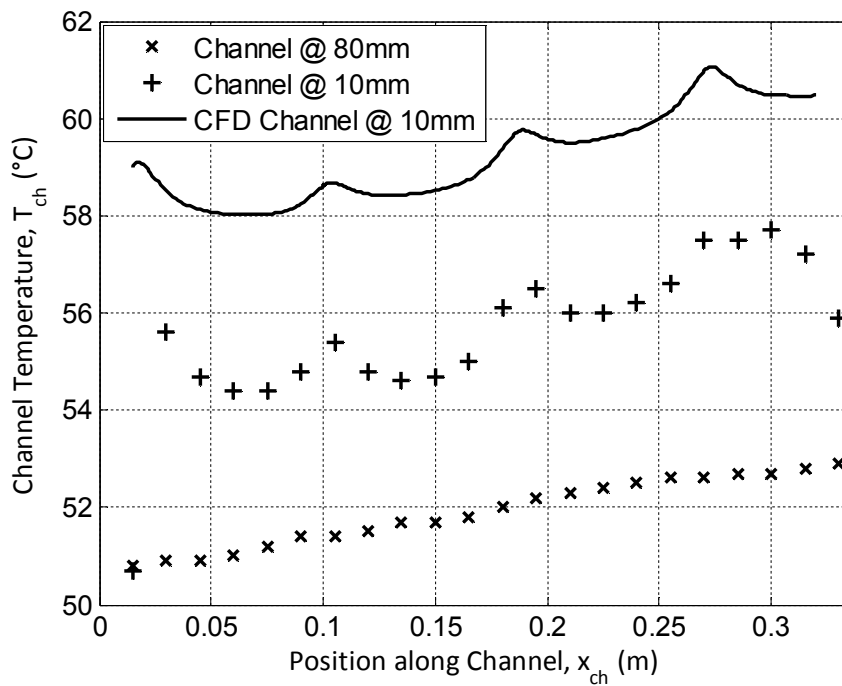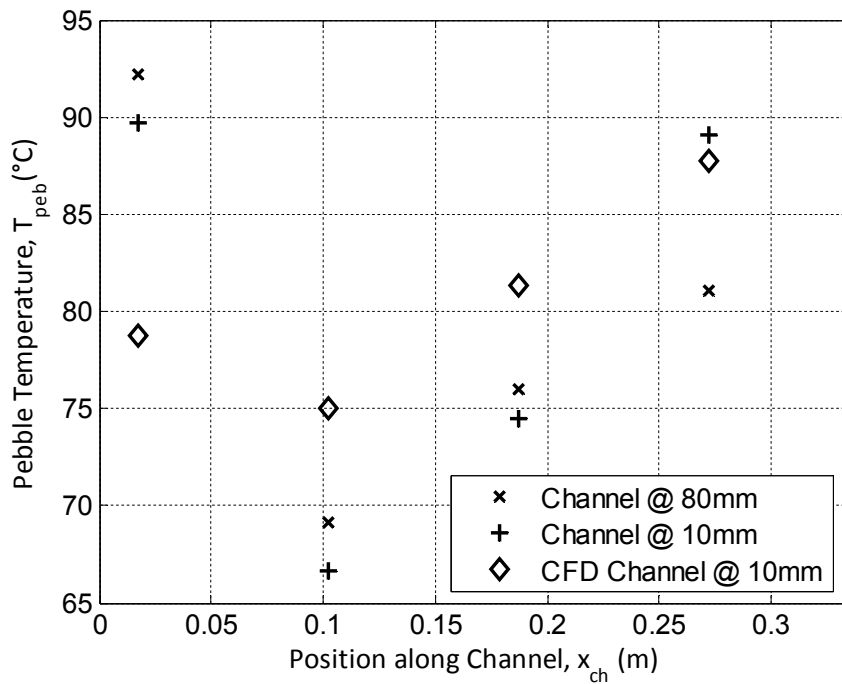
Figure 6-8: Difference with inspection channel closer to pebble bed

7. Discussion and conclusions

Pebble bed nuclear reactors started operating in Germany in 1966. Over the years, a vast amount of research has been done in this field. Since 1999, South Africa became a part of the research endeavor to build a new, safer and more efficient pebble bed reactor. Since the conception of pebble bed reactors, no viable solution has been found to directly measure the dynamic pebble fuel temperature inside such a reactor. This still posed a problem for the design engineers at PBMR, because the safety and efficiency of the reactor is coupled to the pebble temperature. Due to this need, this research study was done to determine if it is indeed possible to measure the pebble fuel temperature by measuring the temperature in the reflector channel and to determine whether there is a measurable peak in temperature on the temperature profile along the reflector channel.

A literature study was completed. The literature study provided a starting point and key issues such as the pebble thermal contact area, inter-pebble flow regimes, various turbulence models to model turbulent flow over spheres and quality mesh generation with unstructured grids was investigated and integrated in the thesis.

When research was done on pebble contact it was found that they have numerous effects on the flow regime when compared to no contact. Two different methods were evaluated to calculate the pebble thermal contact area. Discrepancies were found between the two methods and it was decided that by conducting an experiment some confusion could be eliminated. It was then found that the contact area diameter was much larger than what has been used in literature. Further research was done and a conclusion was drawn that it could be due to adhesion and cohesion forces between the pebbles, where in

literature only gravitational forces were considered and therefore a thermal contact area diameter of 3 mm was used in the numerical model.

The thermal conductivity of spherical packed beds and its dependence on the thermophysical properties of the spheres and gas, load, the rarefaction effects of the interstitial gas, gas temperature and pressure, sphere diameter, roughness and asperity slope were also investigated. A method to calculate the effective thermal contact conductivity was presented. The effective thermal contact conductivity was needed, due to the modelling of the pebble contact as a flat cylinder, rather than a circular plane. The calculated value for the effective thermal contact conductivity; using the thermophysical properties of the materials and gas used in the experiment was further used in the numerical model. It was found that there was only a 0.11 % average difference in channel temperature between simulating the effective thermal contact conductivity using the conductivity for graphite, 160 W/mK and that of the calculated lower conductivity value of 128 W/mK. Due to this, it was shown that the error when using only the material's conductivity to simulate a contact resistance would be small. However, the contact areas cannot be excluded, because there was a significant difference in pebble and channel temperatures when no contact was simulated.

To simulate turbulence in packed beds it was concluded that the Shear Stress Turbulence (SST) k-ω model would best model the flow turbulence due to its ability to solve adverse pressure gradients and flow separation, and is also know to be a good general purpose model. It was also decided that radiation would also be modeled in the numerical model even though simulations occurred at low temperatures. The model that was used in this study was the Discrete Ordinate (DO) radiation model.

An experimental setup simulating a cutout section of the PBMR reactor was built. This was used to determine the pebble fuel temperature and if there are measurable peaks on the temperature profile along the inspection channel. The electrically heated packed bed consists out of a 112 electrically heated graphite pebbles where each could deliver a maximum up to 100 W. Two designs, termed the first and second design of the electrically heated graphite pebbles were built. The second design was an improvement on the first design and showed good performance throughout the experiments. To measure the temperature profile along the inspection channel, a distributed thermocouple measuring device was built and a purposely-built pressure transducer unit was used to measure four individual differential pressures. All of the measurement instruments were either calibrated or were provided with calibration certificates.

The software that was used to for pre-processing was GAMBIT. The electrically heated packed bed experimental setup was successfully constructed and meshed. Due to the complicated task of generating a quality mesh in the contact region between the pebbles, the methodology presented by McLaughlin *et al.* (2008) assisted in overcoming this problem. The method that was used to generate a mesh in the pebble contact region proved to be successful and delivered a good quality mesh. The mesh was generated using tetrahedral cells, after which a polyhedral conversion was performed to lower the computational cost. Although some simplification of the geometry was done, it, however, did not affect the results when compared with the experimental results. A mesh independence study was done to evaluate the solution sensitivity. It was, however, not possible to generate course, medium and fine grids, because of the large number of cells already used and the complex geometry. The mesh independence was evaluated by comparing first and second order discretization schemes for the tetrahedral and polyhedral meshes. The results were found to be mesh independent (small or no change in a particular result, such as the temperature profile down the reflector channel).

FLUENT was used as solver and for post-processing. The solver settings and the boundary conditions were explained and how they were applied in the numerical setup. It was found that the SIMPLE algorithm was the most stable solution method. By following the guidelines (Menter, F.R. 2002) for judging convergence, numerical errors were reduced and provided better judgement for determining when a steady state solution was achived.

An energy balance between the heat gained by the air, as it flowed through the pebble bed and the electric power supplied to the pebbles is given in figure 6-2. In this figure, it is seen that there is a consistent 2.47 % loss of energy through the insulated side walls. From this, two conclusions are immediately apparent. Firstly, the favorable similarity between the input and output energies added confidence to the accuracy of the experimental measurements. Secondly, the zero-heat-flux boundary condition for the side walls in the CFD simulation is reasonably accurate. This does, however, also account for the CFD calculated temperatures being slightly higher than the experimental values as reflected in figure 6-6, figure 6-7 and figure 6-8, for instance.

A difference in pressure is necessary to enable gas is to flow through the pebble bed. This difference in pressure for a given mass flow rate was calculated using the Ergun equation which takes the viscous and form drag into account. The differential pressures across the manifolds and pebble bed was calculated using the numerical model. It was found that the Ergun equation under predicted the experimentally measured differential pressure across the pebble bed. This can be explained due to the small number of pebbles used compared to the number of pebbles used for which the Ergun equation was formulated. The numerically calculated differential pressure over-predicted the experimentally measured differential pressure across the pebble bed and manifolds.

Safety measures were taken, because the heated graphite pebbles could ignite in should they be inadvertently heated above their spontaneous ignition temperature point above 500 °C in air. To reduce the risk of this hazard occurring as well as to ameliorate the consequence should it have occurred, a number of safety measures were taken. The safety measures that were taken was to provide a fire extinguisher, electrical shock sign and information poster, a safety valve to close the air flow and ear protection. Experimental apparatus operating procedures were drawn, also considering safety.

Overall, the CFD has predicted the pebble and reflector temperatures very well when compared to the experimentally measured temperatures. It was indeed found that the peaks in temperature on the temperature profile along the reflector could be measured permitted that the reflector channel be moved closer to the pebbles. The heat being conducted away from the pebble via the contact points caused these temperature peaks. The differences between the numerically calculated pebble temperatures and experimentally measured pebble temperatures could be caused by unsteady flow patterns resulting from turbulence and the geometrical layout inside the experiment.

The CFD results showed promising agreement with the experimental measurements for the temperature and mass flow rates investigated. This warrants further research work to establish whether this would also be the case under actual high temperature conditions (much higher radiations load for example) in the PBMR. CFD may be considered a capable tool to simulate heat transfer phenomena in complex geometries where analytical solutions are impossible.

8. Recommendations

By constructing an experimental setup simulating a cutout section of the PBMR reactor and simulating this setup with a CFD program it was, however, found that there were indeed measureable temperature peaks in the temperature profile along the inspection channel. These peaks were only observed when the channel was move closer to the pebbles and is therefore recommended that some redesigning of the channel should be done if engineers at PBMR wished to measure these temperature peaks.

All of the modelling cases and experiments were conducted in atmospheric conditions using air as coolant and operating at temperatures below 350 °C. The experiments are dimensionally similar to the PBMR core and it is therefore recommended that more simulations be carried out using the conditions experienced in the PBMR reactor.

Due to the dynamic core within the PBMR, pebble bed packings can range from BCC in the center of the annulus towards a FCC at the reflector wall interface. The pebble bed packings are also random to any specific location and cannot be predicted. It is therefore recommended that the simulations and experimentation be continued using a BCC packing in the effort to place some bounds on the pebble and reflector temperatures.

In this study, it was assumed that all of the pebbles made contact with each other and with the reflector wall. A case simulating no contact was performed and it had a major effect on pebble and reflector temperatures. In practice, this would not be the case, because the number of contacts per pebble will vary depending on its location. It is therefore necessary to investigate what effects it will have on the temperature profile along the reflector wall if some of the contacts are removed, simulating a mixture of contact and no contact.

References

Agilent. 2009. *Literature.* http://cp.literature.agilent.com/litweb/pdf/5989-7622EN.pdf.

Bahrami, M., Yovanovich, M.M. & Culham, J.R. 2006. Effective thermal conductivity of rough spherical packed beds. *International Journal of Heat and Mass Transfer* 49: 3691-3071.

British Standards Institution. 1981. BS 1042 Section 1.1: Methods of measurement of fluid flow in closed conduits.

Çengel, Y.A. 2003. *Heat Transfer - A practical approach.* 2nd edition. Boston: McGraw Hill.

Constantinescu, G., Chapelet, M. & Squires, K. 2003. Turbulence modelling applied to flow over a sphere. *AIAA Journal* 41.9: 1733-1742.

Emissivity values for common materials. 2009. http://www.infrared-thermography.com/material-1.htn.

Fiveland, W.A. 1991. The Selection of Discrete Ordinates Quadrature Sets for Anisotropic Scattering. *ASME HTD* 160: 89-96.

FLUENT. 2008. FLUENT 12 Theory Guide. Ansys Inc.

FLUENT. 2006. FLUENT 6.3 - User's guide. Fluent Inc.

Holman, J.P. 1992. *Heat Transfer.* 7th edition. United Kingdom: McGraw Hill.

Honeywell. 2009. *Safety data sheet: Firegum.* http://www.a1motorstores.co.uk/shop-manager-info/cosshh/Holts_ Firegum.pdf.

How the PBMR works. 2007. South Africa: PBMR (Pty) Ltd.

In, W.K., Lee, S.W., Lim, H.S. & Lee, W.J. 2006. Three-dimensional analysis of the hot-spot fuel temperature in pebble bed and prismatic modular reactor. *Transactions of the Korean Nuclear Society Spring Meeting.* Chuncheon. Korea. 305-600.

In, W.K., Chun, T.H., Lee, W.J. & Chang, J.H. 2005. CFD analysis of the fuel temperature in high temperature gas-cooled reactors. Daejon. Korea. 305-600.

In, W.K., Hassan, Y.A. & Lee, W.J. 2008. CFD Simulation of a coolant flow and a heat transfer in a pebble bed reactor. *Proceedings of the 4th International Topical Meeting in High Temperature Reactor Technology.* Washington DC. USA.

Johnson, K.L. 1989. *Contact Mechanics.* Cambridge: Cambridge University Press.

Kim, E.S. & No, H.C. 2006. Experimental study on the oxidation of nuclear graphite and development of an oxidation model. *Journal of Nuclear Materials* 349: 182-194.

Kröger, D.G. 1998. *Air-cooled heat exchangers and cooling towers - Thermal-flow performance evaluation and design.* South Africa: Department of mechanical engineering. University of Stellenbosch.

Laguerre, O., Amara, S.B., Alvarez, G. & Flick, D. 2007. Transient heat transfer by free convection in a packed bed of spheres: Comparison between two modelling approaches and experimental results. *Journal of Applied Thermal Engineering*.

Lalk, J. 2007. PBMR Technology programme: Fuel temperature measurement system project - Sensors. South Africa: PBMR (Pty) Ltd.

Lathrop, K.D. & Carlson, B.G. 1965. *Discrete-ordinates Angular Quadrature of the Neutron Transport Equation.* Technical Information Series Report LASL-3186. Los Alamos National Laboratory.

Lee, J.J., Park, G.C., Kim, K.Y. & Lee, W.J. 2007. Numerical treatment of pebble contact in the flow and heat transfer analysis of a pebble bed reactor core. *Journal of Nuclear Engineering and Design*.

Li, C.C. & Sheehan, J.E. 2007. Friction and wear studies of graphite and a carbon-carbon composite in air and in helium. *General Atomic Company*.

Mathworks. 2009. MATLAB 7.0.1. http://www.mathworks.com.

McLaughlin, B., Worsley, M. & Stainsby, R. 2008. Development of local heat transfer and pressure drop models for pebble bed high temperature gas-cooled reactor cores. *Proceedings of the 4th International Topical Meeting in High Temperature Reactor Technology.* Washington DC. USA.

Menter, F.R. 2002. CFD Best practice guidlines for CFD code validation for reactor-safety applications. *5th Euratom Framework Programme.* European Commision. ECORA.

Menter, F.R., Kuntz, M. & Langtry, R. 2003. Ten years of industrial experience with the SST turbulence model. *Journal of Turbulence, Heat and Mass Transfer 4.* Begell House. Inc.

Menter, F.R. 1994. Two-equation eddy-viscosity turbulence models for engineering applications. *AIAA Journal* 32.8: 1598-1605.

Mills, A.F. 1979. *Heat Transfer.* 2nd edition. New Jersey: Prentice Hall.

Mitchell, M.N. & Polson, A.G. 2007. Assessment of the loads on a solid centre reflector of a pebble bed reactor using DEM techniques. *Journal of Nuclear Engineering and Design* 237: 1332-1340.

Modest, M.F. 1993. *Radiative Heat Transfer.* United States of America: McGraw Hill.

Neamen, D.A. 2001. *Electronic Circuit Analysis and Design*. 2nd edition. New York: McGraw Hill.

NWU. 2007. PBMR Heat transfer test facility. M-Tech Industrial – North West University. South Africa.

Polson, A. 2009. Calculating the contact stiffness and area between two graphite pebbles. South Africa: PBMR (Pty) Ltd.

Powerkote. 2009. *Thermal barrier coatings*. South Africa.

SAG. 2009. Correspondence: Facsimile. South Africa: SAG CC. Industrial Ceramics Supplier.

SGL-Carbon-Group. 2006. *Inspection certificate.* South Africa: PBMR (Pty) Ltd.

Siegel, R. & Howell, J. 2002. *Thermal Radiation Heat Transfer.* 4th edition. New York: Taylor & Francis.

Slabber, J. 2004. Pebble Fuel Advantages. *2nd International Topical Meeting on HTR Technology.* Beijing. China.

Slabber, J., Matzner, H.D. & Theron, W. 2006. Technical description of the PBMR demonstration power plant.South Africa: PBMR (Pty) Ltd.

Sonntag, R.E. & Borgnakke, C. 2001. *Introduction to Engineering Thermodynamics.* New York: John Wiley & Sons Inc.

The pebble bed evolution. 2007. South Africa: PBMR (Pty) Ltd.

Thiart, G.D. 2007. *Numerical Fluid Dynamics 814 - Course Notes.* South Africa: Department of Mechanical and Mechatronic Engineering. University of Stellenbosch.

ThiesClima. 1985. *Instructions for Use: Mercury Station Barometer*.

Tien, C.L. & Vafai, K. 1979. Statistical bounds for the effective thermal conductivity of microsphere and fibrous insulation. *AIAA Prog. Ser.* 65: 135-148.

UCAR. 2009. *Graphite Specialty Products: Technical Information.* South Africa: Graftech SA (Pty) Ltd.

Van Der Merwe, J., Van Antwerpen, H.J. & Mulder, E.J. 2006. Heat transfer correlation limitations at the pebble bed-reflector interface. *3rd International Topical Meeting in High Temperature Reactor Technology.* South Africa.

Versteeg, H.K. & Malalasekera, W. 2007. *An introduction to computational fluid dynamics - The finite volume method.* 2nd edition. Harlow. Essex: Prentice Hall.

Appendix A - Thermophysical properties

The thermophysical properties for dry air, graphite, ceramic and other materials that was used are given in the following sub-sections.

A.1 Thermophysical properties for dry air

The thermophysical properties of dry air at 1 atmosphere pressure within the temperature range 273.15 K to 2273.15 K are given below (Çengel, 2003):

Density:

$$\rho_{air} = p_{atm} / \left[287.08\left(T_{air}\right) \right], \text{kg/m}^3 \tag{A.1}$$

Specific Heat:

$$c_{p-air} = 5.5202 \times 10^{-17} T_{air}^6 - 4.817 \times 10^{-13} T_{air}^5 + 1.6993 \times 10^{-9} T_{air}^4$$
$$- 3.0673 \times 10^{-6} T_{air}^3 + 0.0028762 T_{air}^2 - 1.0841 T_{air} + 1142.9, \text{J/kgK} \tag{A.2}$$

Dynamic Viscosity:

$$\mu_{air} = 3.2306 \times 10^{-15} T_{air}^3 - 1.8708 \times 10^{-11} T_{air}^2 + 5.3168 \times 10^{-8} T_{air}$$
$$+ 4.2943 \times 10^{-6}, \text{kg/ms} \tag{A.3}$$

Kinematic Viscosity:

$$v_{air} = -1.08 \times 10^{-14} T_{air}^3 + 8.7282 \times 10^{-11} T_{air}^2 + 4.7908 \times 10^{-8} T_{air}$$
$$- 6.2596 \times 10^{-6}, \text{m}^2/\text{s} \tag{A.4}$$

Thermal Conductivity:

$$k_{air} = 0.0010022 + 9.0441 \times 10^{-5} T_{air} - 2.9024 \times 10^{-8} T_{air}^2$$
$$+ 4.641 \times 10^{-12} T_{air}^3, \text{W/mK} \tag{A.5}$$

Thermal Diffusivity:

$$\alpha_{air} = -9.9874 \times 10^{-15} T_{air}^3 + 9.0362 \times 10^{-11} T_{air}^2 + 1.0271 \times 10^{-7} T_{air}$$
$$- 1.74 \times 10^{-5}, \text{m}^2/\text{s} \tag{A.6}$$

Prandtl Number:

$$\text{Pr}_{air} = 2.5041 \times 10^{-20} T_{air}^6 - 2.4896 \times 10^{-16} T_{air}^5 + 9.8516 \times 10^{-13} T_{air}^4$$
$$- 1.998 \times 10^{-9} T_{air}^3 + 2.1867 \times 10^{-6} T_{air}^2 - 0.0011676 T_{air} + 0.92875 \tag{A.7}$$

Figure A-1 show the thermophysical properties *versus* the air temperature using the equations above.
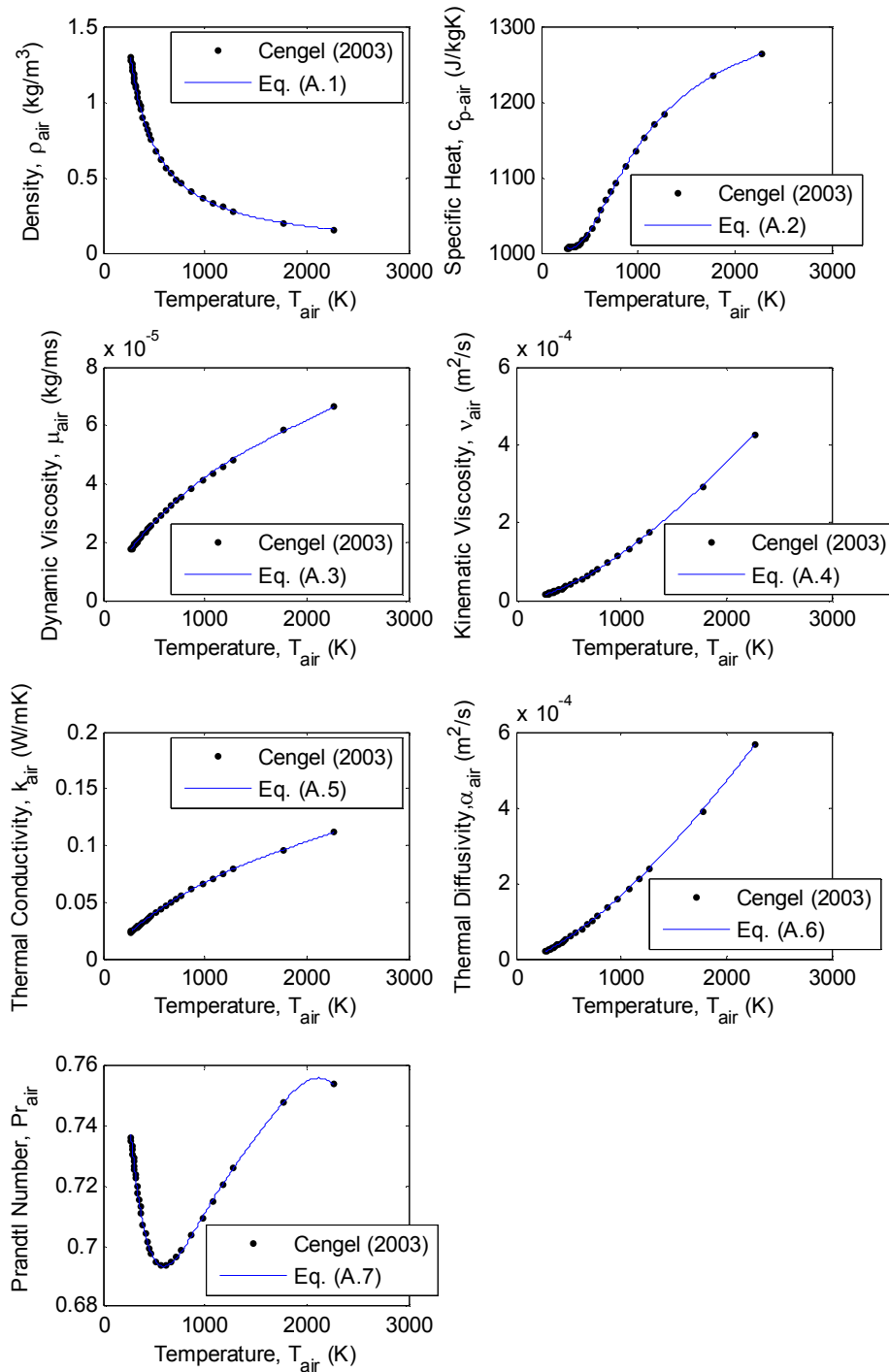
Figure A-1: Thermophysical properties for dry air at 1 atmosphere pressure

A.2   Thermophysical properties for graphite

The graphite used is supplied by Graftech (Pty) Ltd and was used for both the pebbles and the reflector block. Typical properties at room temperature are (UCAR, 2009):

Density:

$$\rho_{graphite} = 1720 \text{ kg/m}^3$$

Thermal conductivity:

$$k_{graphite} = 160 \text{ W/mK}$$

Emissivity (The emissivity is only a representative value):

$$\varepsilon_{graphite} = 0.77$$

Specific heat:

$$
\begin{aligned}
c_{p-graphite} = 4187 \big(& 0.44391 + 0.30795 \times 10^{-5} T_{graphite} \\
& -0.61257 \times 10^{4} T_{graphite}^{-2} + 0.10795 \times 10^{7} T_{graphite}^{-3} \big) \text{, J/kgK}
\end{aligned}
\tag{A.8}
$$

$$
\begin{aligned}
c_{p-graphite} = {} & -4.2034 \times 10^{-18} T_{graphite}^{6} + 5.1742 \times 10^{-14} T_{graphite}^{5} \\
& -2.5934 \times 10^{-10} T_{graphite}^{4} + 6.7985 \times 10^{-7} T_{graphite}^{3} \\
& -0.00099312 T_{graphite}^{2} + 0.7994 T_{graphite} + 1576.3 \text{, J/kgK}
\end{aligned}
\tag{A.9}
$$

where $300 \text{ K} < T_{graphite} < 3200 \text{ K}$. Figure A-2 show the specific heat *versus* the graphite temperature using equations (A.8) and (A.9).
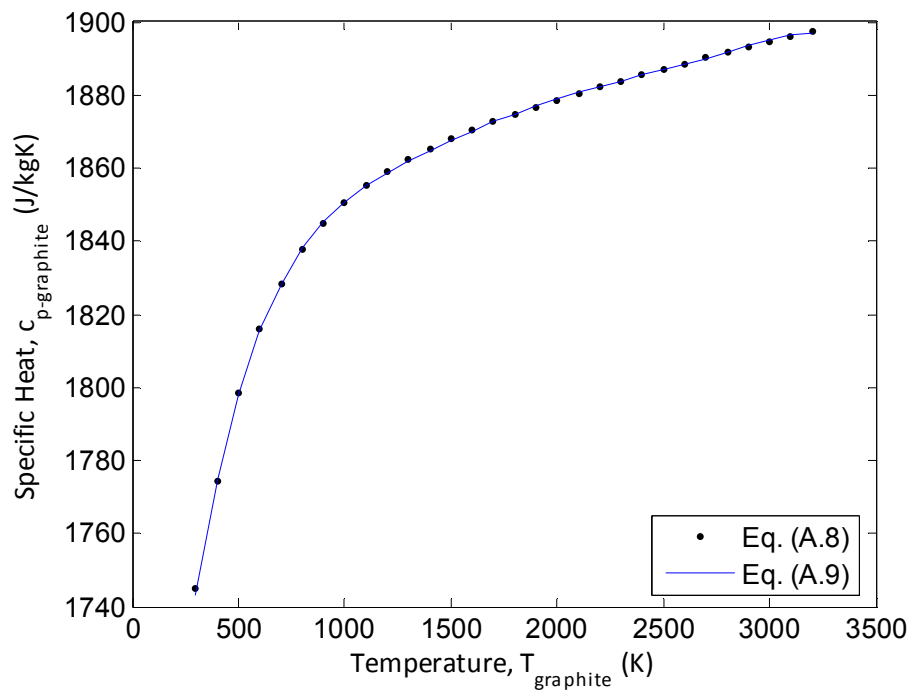
Figure A-2: Specific heat *versus* graphite temperature

A.3   Thermophysical properties for ceramic

SAG Ceramics CC. (SAG, 2009) supplied the properties and ceramic tubes that were used for the ceramic cluster, connecting rods and inserts.

Density:

$$\rho_{ceramic} = 1900, \text{kg/m}^3$$

Thermal conductivity:

$$k_{ceramic} = 1.8, \text{W/mK}$$

Emissivity:

$$\varepsilon_{ceramic} = 0.4$$

Specific heat:

$$c_{p-ceramic} = 900, \text{J/kgK}$$

A.4   Thermophysical properties of other miscellaneous materials

Siegel *et al.* (2002) give the following emissivity for the following two surfaces. These emissivity values was used in the numerical modelling.

Emissivity for stainless steel 310 smooth with a surface temperature of 1090 K:

$$\varepsilon_{ss310smooth} = 0.39$$

Emissivity for paint lacquer flat black with a surface temperature of 370 K:

$$\varepsilon_{paintblack} = 0.98$$

Emissivity values for common materials (2009) give the emissivity for the following surface:

Emissivity for plastic in the wavelength of 5.6 µm:

$$\varepsilon_{plastic} = 0.93$$

Appendix B - Calculations

A sample calculation was done to determine the air mass flow rate through a bell mouth flow meter, the differential pressure over a packed pebble bed and the effective thermal contact conductivity. The atmospheric pressure and temperature correction calculations are also given in the following sections.

B.1 Sample calculation of the air mass flow rate

To determine the mass flow rate of air through the pebble bed, a bell mouth flow meter was used at the inlet to the blower. The differential pressure was measured over the bell mouth flow meter relative to atmosphere and the air temperature was measured just after the bell mouth flow meter. The method described by Kröger (1998) was used to calculate the air mass flow rate.

A sample calculation follows below, which only shows one calculation of the air mass flow rate for one differential pressure. To calculate the mass flow rate for a range of differential pressure, a computer program has been written. The program generates a graphof mass flow rate versus differential pressure. The program code in MATLAB (Mathworks, 2009) is given in Appendix E.

Sample calculation:

Dimensional properties of the elliptical bell mouth flow meter

$$d = 0.105 \text{ m}$$

Calculate the minimum cross-sectional area of the bell mouth flow meter.

$$A_n = \frac{\pi d^2}{4} = \frac{\pi 0.105^2}{4} = 8.659 \times 10^{-3} \text{ m}^2 \tag{B.1}$$

The area upstream of the nozzle is infinitely large, due to it being not enclosed in a wind tunnel

$$A_{tus} = \infty$$

The atmospheric pressure is measured using the Thies Clima mercury barometer and corrected using the calculations in section B.3.

$$p_{up} = 100709 \text{ Pa}$$

The room temperature is measured using the Thies Clima mercury barometer and converted from degrees Celsius to Kelvin.

$$T_{up} = 15 + 273.15 = 288.15 \text{ K}$$

The differential pressure over the bell mouth flow meter relative to atmosphere is measured.

$$\Delta p_n = 269 \text{ Pa}$$

The temperature of the air after the bell mouth flow meter is measured and converted from degrees Celsius to Kelvin.

$$T = 19 + 273.15 = 292.15 \text{ K}$$

The gas constant for air is

$$R = 287.08 \text{ J/kgK}$$

For air, $\dfrac{c_p}{c_v} = 1.4$

Knowing the air temperature, the density and dynamic viscosity can be calculated.

$$\rho_n = \frac{p_{up} + p_n}{RT} = \frac{100709 + 269}{287.08 \cdot 292.15} = 1.204 \text{ kg/m}^3 \tag{B.2}$$

$$
\begin{aligned}
\mu_n &= 2.287973 \times 10^{-6} + 6.259793 \times 10^{-8} T - 3.131956 \times 10^{-11} T^2 \\
&\quad + 8.15038 \times 10^{-15} T^3 \\
&= 2.287973 \times 10^{-6} + 6.259793 \times 10^{-8} \cdot 292.15 \tag{B.3} \\
&\quad - 3.131956 \times 10^{-11} \cdot 292.15^2 + 8.15038 \times 10^{-15} \cdot 292.15^3 \\
&= 18.106 \times 10^{-6} \text{ kg/ms}
\end{aligned}
$$

The approach velocity factor was calculated by means of

$$Y = 1 + 0.5\left(A_n / A_{tus}\right)^2 + 2\left(A_n / A_{tus}\right)^2 \Delta p_n / \left(p_{up} \frac{c_p}{c_v}\right)$$

$$= 1 + 0.5\left(8.659 \times 10^{-3} / \infty\right)^2 \tag{B.4}$$

$$+ 2\left(8.659 \times 10^{-3} / \infty\right)^2 \cdot 269 / \left(100709 \cdot 1.4\right)$$

$$= 1$$

The gas expansion factor was calculated by means of

$$\phi_g = 1 - 3\Delta p_n / \left(4 p_{up} \frac{c_p}{c_v}\right) = 1 - 3 \cdot 269 / \left(4 \cdot 100709 \cdot 1.4\right) = 0.9986 \tag{B.5}$$

Initial guess for the mass flow rate.

$$\dot{m}_{air} = 0.08 \text{ kg/s}$$

The Reynolds number can now be calculated by means of

$$\text{Re}_n = \frac{4\dot{m}_{air}}{\pi d \mu_n} = \frac{4 \cdot 0.08}{\pi \cdot 0.105 \cdot 18.106 \times 10^{-6}} = 53578 \tag{B.6}$$

The bell mouth flow meter, coefficient of discharge can now be calculated using the Reynolds number.

For $30000 < \text{Re}_n < 100000$

$$C_n = 0.954803 + 6.37817 \times 10^{-7} \text{Re}_n - 4.65394 \times 10^{-12} \text{Re}_n^2$$

$$+ 1.33514 \times 10^{-17} \text{Re}_n^3$$

$$= 0.954803 + 6.37817 \times 10^{-7} \cdot 53578 - 4.65394 \times 10^{-12} \cdot 53578^2 \tag{B.7}$$

$$+ 1.33514 \times 10^{-17} \cdot 53578^3$$

$$= 0.9777$$

Revised mass flow rate is calculated by means of

$$\dot{m}_{air} = C_n \phi_g Y A_n \left(2 \rho_n \Delta p_n\right)^{0.5}$$

$$= 0.9777 \cdot 0.9986 \cdot 1 \cdot 8.659 \times 10^{-3} \left(2 \cdot 1.204 \cdot 269\right)^{0.5} \tag{B.8}$$

$$= 0.2159 \text{ kg/s}$$

The revised Reynolds number can now be calculated.

$$\text{Re}_n = \frac{4\dot{m}_{air}}{\pi d \mu_n} = \frac{4 \cdot 0.2159}{\pi \cdot 0.105 \cdot 18.106 \times 10^{-6}} = 144600 \tag{B.9}$$

The bell mouth flow meter, coefficient of discharge can now be recalculated using the revised Reynolds number.

For $30000 < \mathrm{Re}_n < 100000$

$$
\begin{aligned}
C_n &= 0.9758 + 1.08 \times 10^{-7} \, \mathrm{Re}_n - 1.6 \times 10^{-13} \, \mathrm{Re}_n^2 \\
&= 0.9758 + 1.08 \times 10^{-7} \cdot 144600 - 1.6 \times 10^{-13} \cdot 144600^2 \\
&= 0.9914
\end{aligned}
\tag{B.10}
$$

The new mass flow rate is now:

$$
\begin{aligned}
\dot{m}_{air} &= C_n \phi_g Y A_n \left(2\rho_n \Delta p_n \right)^{0.5} \\
&= 0.9914 \cdot 0.9986 \cdot 1 \cdot 8.659 \times 10^{-3} \left(2 \cdot 1.204 \cdot 269 \right)^{0.5} \\
&= 0.2182 \text{ kg/s}
\end{aligned}
\tag{B.11}
$$

After a further five iterations the converged mass flow rate is 0.21745 kg/s. This is the value indicated as the *working point* as seen in figure B-1.
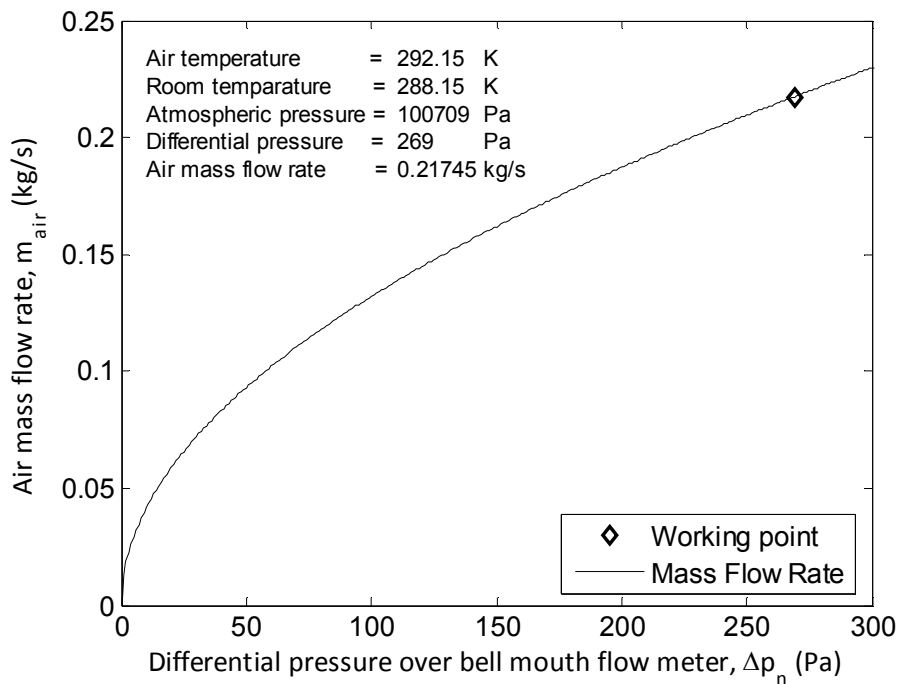
Figure B-1: Air mass flow rate *versus* differential pressure over bell mouth flow meter

B.2   Sample calculation of differential pressure over packed bed

To calculate the differential pressure drop over the packed bed the Ergun equation (Mills, 1979) is used. A sample calculation for the packed bed in the experimental setup is shown below.

The void fraction is defined as

$$\varepsilon_v = \frac{\text{Bed volume} - \text{Packing volume}}{\text{Bed volume}} \tag{B.12}$$

and calculated as

$$\varepsilon_v = \frac{0.02106 - \left(1.983811 \times 10^{-5} \cdot 32 + 1.13097336 \times 10^{-4} \cdot 112\right)}{0.02106}$$
$$= 0.36864$$

The specific surface area a [m^{-1}] of a packed bed is the transfer area per unit volume of the bed:

$$a = \frac{\text{Total surface area of particles}}{\text{Bed volume}} \tag{B.13}$$

The specific surface area for the pebble bed is

$$a = \frac{\left(0.003015928947 \cdot 32 + 0.011309733553 \cdot 112\right)}{0.356711 \cdot 0.315 \cdot 0.1875}$$
$$= 64.704 \text{ m}^{-1}$$

Next the cross-sectional area of the pebble bed has to be calculated

$$A_c = 0.315 \cdot 0.1875 = 0.059063 \text{ m}^2$$

The effective particle diameter is calculated by means of

$$d_p = 6 \cdot \frac{\left(1 - \varepsilon_v\right)}{a} \tag{B.14}$$

Therefore

$$d_p = 6 \cdot \frac{\left(1 - 0.36864\right)}{64.704} = 0.058546 \text{ m}$$

The characteristic velocity and length are defined as follow:

$$V = \frac{\dot{m}}{\rho \varepsilon_v A_c} \tag{B.15}$$

and

$$L = d_p \left(\frac{\varepsilon_v}{1 - \varepsilon_v} \right) \tag{B.16}$$

Hence the characteristic velocity and length are calculated as

$$V = \frac{0.24034}{1.1958 \cdot 0.36864 \cdot 0.059063} = 9.231 \text{ m/s}$$

and

$$L = 0.058546 \left(\frac{0.36864}{1 - 0.36864} \right) = 0.034184 \text{ m}$$

The pressure drop over the pebbles can be obtained using

$$\frac{dP}{dx} = 150 \frac{\mu V}{L^2} + 1.75 \frac{\rho V^2}{L} \tag{B.17}$$

And calculated as

$$\frac{dP}{dx} = 150 \frac{1.8064e\text{-}005 \cdot 9.231}{0.034184^2} + 1.75 \frac{1.1958 \cdot 9.231^2}{0.034184} = 5238 \text{ Pa/m}$$

Times the length of the pebble bed the total pressure drop over the pebbles is

$$dP_{peb} = \frac{dP}{dx} \cdot l_{peb} = 5238 \cdot 0.254558 = 1333.4 \text{ Pa}$$

B.3 Sample calculation of atmospheric pressure and room temperature using the Thies Clima mercury station barometer

The Thies Clima mercury station barometer was used to measure the room temperature as well as the atmospheric pressure. Below is a sample calculation for correcting the reading taken from the barometer as described in the Thies Clima mercury station barometer hand guide (ThiesClima, 1985). Thereafter due to many readings that need to be corrected, a computer programs was written to correct the readings. The computer program is given in Appendix E.

Sample calculation:

Atmospheric pressure and room temperature readings are taken

$$P = 1002.6 \text{ mbar}$$

$$t = 21°C$$

Correcting for the effect of the temperature

$$\Delta P_t = -\left(\alpha_{Hg} - \alpha_{Ms}\right)tP \qquad\qquad\qquad\qquad (B.18)$$

The cubic expansion coefficient for mercury is

$$\alpha_{Hg} = 1.81 \times 10^{-4} \text{ K}^{-1}$$

and the value for the linear expansion coefficient of the fixed glass scale is

$$\alpha_{Ms} = 0.19 \times 10^{-4} \text{ K}^{-1}$$

$$\Delta P_t = -\left(1.81 \times 10^{-4} - 0.19 \times 10^{-4}\right) \cdot 21 \cdot 1002.6 = -3.4108 \text{ mbar}$$

The corrective value must be subtracted from the barometer reading when the temperature exceeds 0 °C, otherwise it must be added if the temperature is less than 0 °C. Therefore because room temperature is above 0 °C, the reading corrected to 0 °C is

$$P_0 = P - \left|\Delta P_t\right| = 1002.6 - 3.4108 = 999.189 \text{ mbar}$$

Correcting the difference in pressure in mbar as a result of the geographical latitude

$$\Delta P_\rho = -2.56 \times 10^{-3} \cos 2\rho \cdot P_0 \qquad\qquad\qquad\qquad (B.19)$$

The geographical latitude of the observation point (Stellenbosch University), is

$$\rho = 33.92°$$

Substituting into the formula results in

$$\Delta P_\rho = -2.56 \times 10^{-3} \cos\left(2 \cdot 33.92\right) \cdot 999.189 = -0.9648 \text{ mbar}$$

Correcting the pressure due to the effects of gravity in relation to the geographical latitude

$$P_{0\rho} = P_0 + \Delta P_\rho = 999.189 - 0.9648 = 998.2242 \text{ mbar}$$

Correcting the difference in pressure in mbar as a result of the elevation

$$\Delta P_H = -1.96 \times 10^{-7} H P_0 \tag{B.20}$$

The elevation of the observation point (Stellenbosch University) above sea level, is

$$H = 111 \text{ m}$$

Substituting into the formula one obtains

$$\Delta P_H = -1.69 \times 10^{-7} \cdot 111 \cdot 999.189 = -0.0217 \text{ mbar}$$

Correcting the pressure due to the effects of gravity in relation to the elevation of the observation

$$P_{0\rho H} = P_{0\rho} + \Delta P_H = 998.2242 - 0.0217 = 998.202 \text{ mbar} \tag{B.21}$$

Thus, the corrected atmospheric pressure is 998.202 mbar or 99.8202 kPa at a room temperature of 21 °C.

B.4   Sample calculation of the effective thermal contact conductivity

From Holman (1992), it is possible to calculate the effective thermal contact conductivity for the contact area between graphite and air.

The following assumptions are made:

- o The graphite used has a porosity of 20 % (SGL-Carbon-Group, 2006). Therefore, it is assumed that the contact area for the graphite will be 80 % of the total contact area and that the void area will be 20 % of the total contact area.
- o The properties for the contact area will be evaluated at 300 K and it will be assumed that the thermal conductivity stay constant.
- o The compressed length of the contact area remains the same for all the contacts and is taken as 0.075049 mm
- o The contact area diameter will also remain fixed for all contacts, and is taken as 3 mm diameter.

From Holman (1992) the thermal contact resistance can be calculated using the following equation

$$h_c = \frac{1}{L_g}\left(\frac{A_c}{A}\frac{2k_A k_B}{k_A + k_B} + \frac{A_v}{A}k_f\right), \text{W/m}^2\text{K} \qquad (B.22)$$

Where

$L_g =$ Thickness of the void space

$A =$ Total cross-sectional contact area

$A_c =$ Contact area

$A_v =$ Void area

$k_A =$ Thermal conductivity, material A

$k_B =$ Thermal conductivity, material B

$k_f =$ Thermal conductivity, interstitial fluid

Knowing that

$k_A = k_B = 160, \text{W/mK}$

$k_f = 0.02566, \text{W/mK}$

$L_g = 0.075049, \text{m}$

$$A = \pi 0.0015^2 = 7.068583 \times 10^{-6} m^2 \qquad (B.23)$$

$$A_c = 0.8A, \text{m}^2 \qquad (B.24)$$

$$A_v = 0.2A, \text{m}^2 \qquad (B.25)$$

the thermal contact resistance can be calculated.

$$h_c = \frac{1}{L_g}\left(0.8 \cdot 160 + 0.2 \cdot 0.02566\right) = \frac{128.005132}{L_g}, \text{W/m}^2\text{K} \qquad (B.26)$$

The amount of heat flow over the contact area can be written as follow

$\dot{Q} = k_{contact}\dfrac{A}{L_g}\Delta T$ and $\dot{Q} = h_c A \Delta T$. Therefore we can now conclude that

$$k_{contact}\frac{A}{L_g}\Delta T = h_c A \Delta T$$

$$k_{contact}\frac{A}{L_g} = \frac{128.005132}{L_g}A \qquad (B.27)$$

$$k_{contact} = 128.005132 \text{ W/mK}$$

The effective thermal conductivity is less that of graphite. This can be expected, as the thermal conductivity of the entrapped air is much less than that of graphite, causing a thermal resistance.

Appendix C - Calibration data

Calibration data and/or certificate information relating to any equipment that was used is given in the following sub-sections.

C.1   Data logging equipment

To record and log all experimental measurements it was necessary to use a data logging unit. The Agilent Data Acquisition/Switch Unit 34970A and necessary components, such as multiplexer cards were used for this purpose.

All calibration and functional test certificates were supplied by the manufacturer (Agilent, 2009). For reference the calibration and functional test information is listed in table C-1.

Table C-1: Calibration and functional test certificate information for data logging equipment

Description	Data Acquisition/Switch Unit	USB/GPIB Interface USB 2.0	20-Channel Armature Multiplexer
Certificate No	34970AMY44036109	82357BMY48100650	34901AMY41087800
Manufacturer	Agilent Technologies	Agilent Technologies	Agilent Technologies
Serial No	MY44036109	MY48100650	MY41087800
Model No	34970A	82357B	34901A
Date of Calibration /Test	19 MAR 2008	23 MAR 2008	23 MAR 2008
Temperature	(23 +/-5)C	(23 +/-5)C	(23 +/-5)C
Humidity	20 to 50 % RH	40 to 70 % RH	10 to 50 %
Procedure	VM_34970AF/2061 66070472	82357B VERIFICATION	at34901a_902a_908a_ cal.tpa

C.2   Force transducer

A force transducer was used to measure the force that was applied to the two pebbles as explained in section 3.1. A declaration of conformity was supplied with the force transducer. Figure C-1 show a photograph of the force transducer and the specifications are listed in table C-2.
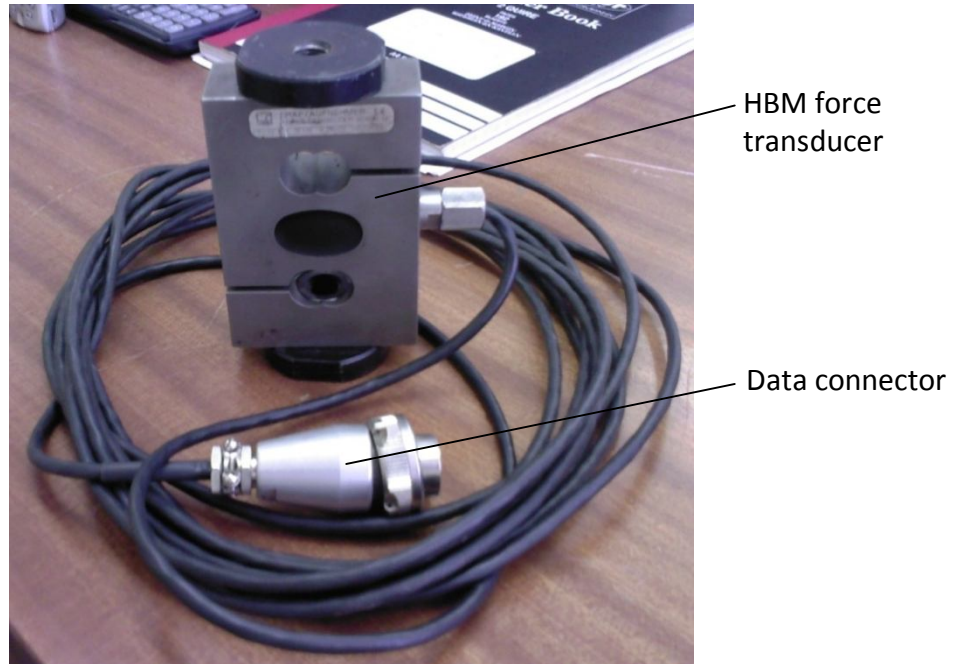
Figure C-1: HBM force transducer

Table C-2: Specifications for the HBM force transducer

Manufacturer	**Hottinger Baldwin Messtechnik (HBM)**
Type	S9
Declaration of Conformity	Document: 101/01.1998
Serial no.	220409A
Nominal force	20 kN
Nominal sensitivity	2 mV/V

C.3 Thermocouples

All the thermocouples that are used in the experiment were calibrated. The thermocouples are calibrated at three different temperatures, 0 °C, room temperature and using hot water (close to boiling). The calibration set was repeated to ensure repeatability. The thermocouples are calibrated against a platinum resistance thermometer. The calibration data for the platinum resistance thermometer is displayed in table C-3.

Table C-3: Calibration information for the platinum resistance thermometer

Manufacturer:	**Isotech**
Model number:	935-14-72
Serial number:	191069
Calibrated by:	CSIR National Metrology Laboratory (NML)
Calibration procedure:	NML-TH/RT-0002
Period of calibration:	25-27 May 2003

The procedure that was used is:

All the thermocouples and resistance thermometer was connected to the data logging equipment. The sensors were then placed inside a hot water urn. Thermal insulation as seen in figure C-2 (b) was wrapped around the urn to improve insulation and to maintain a constant temperature. For each test, either the water was heated, left at room temperature or ice was added to maintain the desired temperature. During each test a stirring device was used to ensure that the water is well mixed and at uniform temperature, except for the ice test. Each test was left to reach a steady state at which there was no more visible change in temperature. Once steady state was reached the readings was taken, after which preparation for the next test started. A schematic of the calibration setup is illustrated in figure C-2 (a).
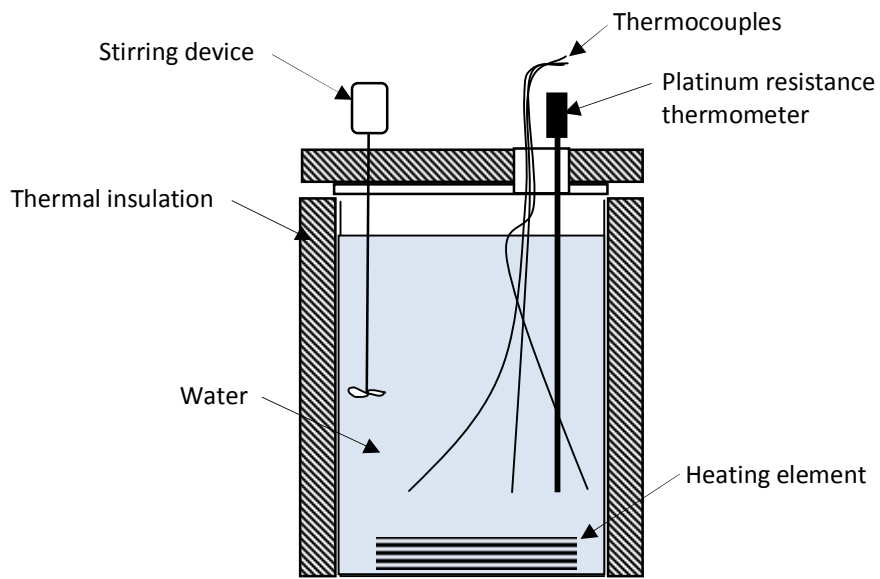
(a)
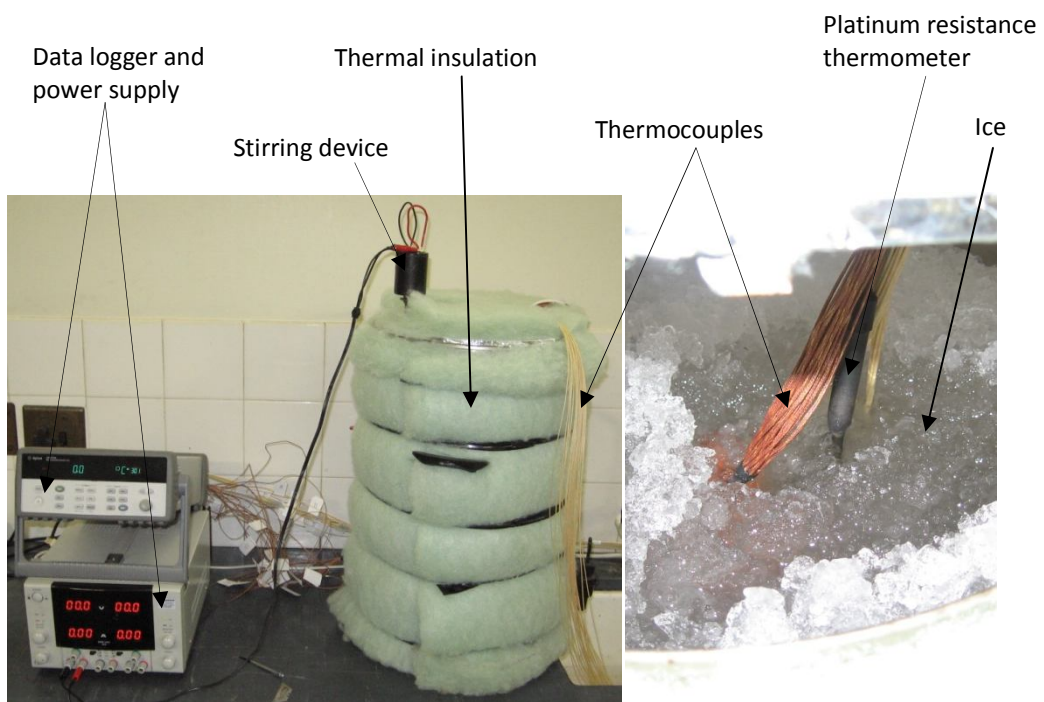
(b)

Figure C-2: (a) Calibration setup, (b) Ice test

The difference between the platinum resistance thermometer and the thermocouple temperature reading is calculated as part of the calibration. Two

calibration tests were conducted to show repeatability and these tests are listed in table C-4 and the maximum calibrated temperature difference per channel is listed in table C-5.

Table C-4: Calibration results for thermocouples

| | | | Calibration Test 1 | | | | | |
Name	Channel	Type	Ice Test (°C)	Difference (°C)	Room Temperature Test (°C)	Difference (°C)	Hot Water Test (°C)	Difference (°C)
T101	101	k-type	-0.2	-0.2	21.3	0.3	89.8	0.4
T102	102	k-type	-0.2	-0.2	21.3	0.3	90.6	1.2
T103	103	k-type	-0.2	-0.2	21.3	0.3	90.0	0.6
T104	104	k-type	-0.2	-0.2	21.3	0.3	90.8	1.4
T105	105	k-type	-0.2	-0.2	21.4	0.4	90.1	0.7
T106	106	k-type	-0.1	-0.1	21.4	0.4	90.4	1.0
T107	107	k-type	-0.1	-0.1	21.4	0.4	90.1	0.7
T108	108	k-type	0.0	0.0	21.4	0.4	90.0	0.6
T109	109	k-type	0.0	0.0	21.4	0.4	90.0	0.6
T110	110	k-type	0.0	0.0	21.4	0.4	90.1	0.7
T111	111	k-type	0.0	0.0	21.4	0.4	90.3	0.9
T112	112	k-type	0.0	0.0	21.4	0.4	90.1	0.7
T113	113	k-type	0.0	0.0	21.4	0.4	90.1	0.7
T114	114	k-type	0.0	0.0	21.4	0.4	90.0	0.6
T115	115	k-type	0.0	0.0	21.4	0.4	90.0	0.6
T116	116	k-type	0.0	0.0	21.4	0.4	90.0	0.6
T117	117	k-type	0.0	0.0	21.4	0.4	90.4	1.0
T118	118	k-type	0.0	0.0	21.5	0.5	90.0	0.6
T119	119	k-type	0.0	0.0	21.5	0.5	90.0	0.6
T120	120	k-type	0.0	0.0	21.6	0.6	90.1	0.7
			Calibration Test 2					
Name	Channel	Type	Ice Test (°C)	Difference (°C)	Room Temperature Test (°C)	Difference (°C)	Hot Water Test (°C)	Difference (°C)
T101	101	k-type	0.4	0.4	17.6	-0.7	92.2	0.0
T102	102	k-type	0.0	0.0	17.6	-0.7	92.7	0.5
T103	103	k-type	0.0	0.0	17.6	-0.7	92.6	0.4
T104	104	k-type	0.0	0.0	17.7	-0.6	92.7	0.5
T105	105	k-type	0.1	0.1	17.7	-0.6	92.8	0.6
T106	106	k-type	0.2	0.2	17.7	-0.6	93.3	1.1
T107	107	k-type	0.2	0.2	17.8	-0.5	92.9	0.7
T108	108	k-type	0.2	0.2	17.8	-0.5	92.8	0.6
T109	109	k-type	0.2	0.2	17.8	-0.5	92.7	0.5
T110	110	k-type	0.2	0.2	17.8	-0.5	92.8	0.6
T111	111	k-type	0.1	0.1	17.8	-0.5	92.7	0.5
T112	112	k-type	0.3	0.3	17.8	-0.5	92.9	0.7
T113	113	k-type	0.2	0.2	17.8	-0.5	92.8	0.6
T114	114	k-type	0.2	0.2	17.8	-0.5	92.7	0.5
T115	115	k-type	0.2	0.2	17.8	-0.5	92.7	0.5
T116	116	k-type	0.1	0.1	17.8	-0.5	92.7	0.5
T117	117	k-type	0.0	0.0	17.8	-0.5	92.7	0.5
T118	118	k-type	0.1	0.1	17.8	-0.5	92.7	0.5

Name	Channel	Type	Ice Test (°C)	Difference (°C)	Room Temperature Test (°C)	Difference (°C)	Hot Water Test (°C)	Difference (°C)
T119	119	k-type	0.0	0.0	17.8	-0.5	92.7	0.5
T120	120	k-type	0.0	0.0	17.9	-0.4	92.6	0.4
			Calibration Test 1					
Name	Channel	Type	Ice Test (°C)	Difference (°C)	Room Temperature Test (°C)	Difference (°C)	Hot Water Test (°C)	Difference (°C)
T201	201	k-type	0.2	0.2	21.9	0.9	90.5	1.1
T202	202	k-type	0.3	0.3	21.8	0.8	90.5	1.1
T203	203	k-type	0.3	0.3	21.8	0.8	90.4	1.0
T204	204	k-type	0.4	0.4	21.7	0.7	90.4	1.0
T205	205	k-type	0.4	0.4	21.7	0.7	90.4	1.0
T206	206	k-type	0.5	0.5	21.8	0.8	90.4	1.0
T207	207	k-type	0.4	0.4	21.7	0.7	90.3	0.9
T208	208	k-type	0.4	0.4	21.7	0.7	90.3	0.9
T209	209	k-type	0.5	0.5	21.7	0.7	90.4	1.0
T210	210	k-type	0.4	0.4	21.7	0.7	90.4	1.0
T211	211	k-type	0.4	0.4	21.7	0.7	90.3	0.9
T212	212	k-type	0.5	0.5	21.7	0.7	90.3	0.9
T213	213	k-type	0.5	0.5	21.7	0.7	90.3	0.9
T214	214	k-type	0.5	0.5	21.7	0.7	90.3	0.9
T215	215	k-type	0.5	0.5	21.7	0.7	90.3	0.9
T216	216	k-type	0.5	0.5	21.7	0.7	90.2	0.8
T217	217	k-type	0.4	0.4	21.7	0.7	90.2	0.8
T218	218	k-type	0.4	0.4	21.8	0.8	90.3	0.9
T219	219	k-type	0.5	0.5	21.8	0.8	90.4	1.0
T220	220	k-type	0.5	0.5	21.9	0.9	90.4	1.0
			Calibration Test 2					
Name	Channel	Type	Ice Test (°C)	Difference (°C)	Room Temperature Test (°C)	Difference (°C)	Hot Water Test (°C)	Difference (°C)
T201	201	k-type	0.3	0.3	18.2	-0.1	92.8	0.6
T202	202	k-type	0.4	0.4	18.2	-0.1	92.9	0.7
T203	203	k-type	0.3	0.3	18.2	-0.1	92.8	0.6
T204	204	k-type	0.4	0.4	18.2	-0.1	92.8	0.6
T205	205	k-type	0.4	0.4	18.3	0.0	92.9	0.7
T206	206	k-type	0.5	0.5	18.3	0.0	92.9	0.7
T207	207	k-type	0.4	0.4	18.3	0.0	92.9	0.7
T208	208	k-type	0.4	0.4	18.3	0.0	92.9	0.7
T209	209	k-type	0.4	0.4	18.3	0.0	93.0	0.8
T210	210	k-type	0.4	0.4	18.3	0.0	93.0	0.8
T211	211	k-type	0.3	0.3	18.3	0.0	92.9	0.7
T212	212	k-type	0.4	0.4	18.3	0.0	92.9	0.7
T213	213	k-type	0.4	0.4	18.3	0.0	92.9	0.7
T214	214	k-type	0.4	0.4	18.4	0.1	92.9	0.7
T215	215	k-type	0.4	0.4	18.4	0.1	92.8	0.6
T216	216	k-type	0.4	0.4	18.4	0.1	92.7	0.5
T217	217	k-type	0.3	0.3	18.4	0.1	92.7	0.5
T218	218	k-type	0.3	0.3	18.4	0.1	92.6	0.4
T219	219	k-type	0.3	0.3	18.4	0.1	92.7	0.5
T220	220	k-type	0.4	0.4	18.3	0.0	92.7	0.5
			Calibration Test 1					
Name	Channel	Type	Ice Test (°C)	Difference (°C)	Room Temperature Test (°C)	Difference (°C)	Hot Water Test (°C)	Difference (°C)
T301	301	PT-100	0.0	0.0	21.0	0.0	89.4	0.0

Name	Channel	Type	Ice Test (°C)	Difference (°C)	Room Temperature Test (°C)	Difference (°C)	Hot Water Test (°C)	Difference (°C)
T302	302	k-type	0.0	0.0	21.1	0.1	90.1	0.7
T303	303	k-type	0.2	0.2	21.3	0.3	90.3	0.9
T304	304	k-type	0.2	0.2	21.2	0.2	90.5	1.1
T305	305	k-type	0.3	0.3	21.3	0.3	90.7	1.3
T306	306	k-type	0.4	0.4	21.4	0.4	90.7	1.3
T307	307	k-type	0.4	0.4	21.4	0.4	90.6	1.2
T308	308	k-type	0.4	0.4	21.4	0.4	90.5	1.1
T309	309	k-type	0.4	0.4	21.3	0.3	90.5	1.1
			Calibration Test 2					
Name	Channel	Type	Ice Test (°C)	Difference (°C)	Room Temperature Test (°C)	Difference (°C)	Hot Water Test (°C)	Difference (°C)
T301	301	PT-100	0.0	0.0	18.3	0.0	92.2	0.0
T302	302	k-type	0.0	0.0	18.2	-0.1	92.5	0.3
T303	303	k-type	0.2	0.2	18.3	0.0	92.6	0.4
T304	304	k-type	0.0	0.0	18.4	0.1	92.9	0.7
T305	305	k-type	0.1	0.1	18.5	0.2	93.1	0.9
T306	306	k-type	0.2	0.2	18.6	0.3	93.2	1.0
T307	307	k-type	0.2	0.2	18.6	0.3	93.1	0.9
T308	308	k-type	0.2	0.2	18.6	0.3	93.1	0.9
T309	309	k-type	0.2	0.2	18.6	0.3	93.1	0.9

Table C-5: Maximum calibrated temperature difference per channel

Name	Channel	Type	Max Uncertainty (°C)	Name	Channel	Type	Max Uncertainty (°C)	Name	Channel	Type	Max Uncertainty (°C)
T101	101	k-type	0.7	T201	201	k-type	1.1	T301	301	PT-100	0.0
T102	102	k-type	1.2	T202	202	k-type	1.1	T302	302	k-type	0.7
T103	103	k-type	0.7	T203	203	k-type	1.0	T303	303	k-type	0.9
T104	104	k-type	1.4	T204	204	k-type	1.0	T304	304	k-type	1.1
T105	105	k-type	0.7	T205	205	k-type	1.0	T305	305	k-type	1.3
T106	106	k-type	1.1	T206	206	k-type	1.0	T306	306	k-type	1.3
T107	107	k-type	0.7	T207	207	k-type	0.9	T307	307	k-type	1.2
T108	108	k-type	0.6	T208	208	k-type	0.9	T308	308	k-type	1.1
T109	109	k-type	0.6	T209	209	k-type	1.0	T309	309	k-type	1.1
T110	110	k-type	0.7	T210	210	k-type	1.0				
T111	111	k-type	0.9	T211	211	k-type	0.9				
T112	112	k-type	0.7	T212	212	k-type	0.9				
T113	113	k-type	0.7	T213	213	k-type	0.9				
T114	114	k-type	0.6	T214	214	k-type	0.9				
T115	115	k-type	0.6	T215	215	k-type	0.9				
T116	116	k-type	0.6	T216	216	k-type	0.8				
T117	117	k-type	1.0	T217	217	k-type	0.8				
T118	118	k-type	0.6	T218	218	k-type	0.9				
T119	119	k-type	0.6	T219	219	k-type	1.0				
T120	120	k-type	0.7	T220	220	k-type	1.0				

An uncertainty analysis was done to determine the experimental uncertainty associated with each thermocouple. Using equation C.1 the statistical variance $u\left(x_{i,statistical}\right)$, for each thermocouple was calculated:

$$u\left(x_{i,statistical}\right) = \sqrt{\frac{\sum_{i=1}^{N}\left(x_i - \overline{x}\right)^2}{N}}$$ (C.1)

where x_i is the measured temperature value and $\overline{x}$ the average of the N sample points. The uncertainty for the data logger that was used, $u\left(x_{i,instrument}\right)$ was ± 1 °C. To combine the uncertainties of both the thermocouples and the data logger equation C.2 is used, which calculates the measured experimental uncertainty $u\left(x_{i,exp}\right)$. The results of the two equations can be found in table C-6.

$$u\left(x_{i,exp}\right) = \sqrt{\left[u\left(x_{i,statistical}\right)\right]^2 + \left[u\left(x_{i,instrument}\right)\right]^2}$$ (C.2)

Table C-6: Statistical results for thermocouples

Name	Channel	Type	$u\left(x_{i,statistical}\right)$	$u\left(x_{i,exp}\right)$
T101	101	k-type	0.5	1.1
T102	102	k-type	0.7	1.2
T103	103	k-type	0.5	1.1
T104	104	k-type	0.7	1.2
T105	105	k-type	0.5	1.1
T106	106	k-type	0.6	1.2
T107	107	k-type	0.5	1.1
T108	108	k-type	0.4	1.1
T109	109	k-type	0.4	1.1
T110	110	k-type	0.4	1.1
T111	111	k-type	0.5	1.1
T112	112	k-type	0.5	1.1
T113	113	k-type	0.4	1.1
T114	114	k-type	0.4	1.1
T115	115	k-type	0.4	1.1
T116	116	k-type	0.4	1.1
T117	117	k-type	0.5	1.1
T118	118	k-type	0.4	1.1
T119	119	k-type	0.4	1.1
T120	120	k-type	0.4	1.1
Name	Channel	Type	$u\left(x_{i,statistical}\right)$	$u\left(x_{i,exp}\right)$
T201	201	k-type	0.4	1.1

Name	Channel	Type	$u(x_{i,statistical})$	$u(x_{i,exp})$
T202	202	k-type	0.4	1.1
T203	203	k-type	0.4	1.1
T204	204	k-type	0.3	1.1
T205	205	k-type	0.3	1.0
T206	206	k-type	0.3	1.0
T207	207	k-type	0.3	1.0
T208	208	k-type	0.3	1.0
T209	209	k-type	0.3	1.0
T210	210	k-type	0.3	1.1
T211	211	k-type	0.3	1.0
T212	212	k-type	0.3	1.0
T213	213	k-type	0.3	1.0
T214	214	k-type	0.3	1.0
T215	215	k-type	0.2	1.0
T216	216	k-type	0.2	1.0
T217	217	k-type	0.2	1.0
T218	218	k-type	0.3	1.0
T219	219	k-type	0.3	1.0
T220	220	k-type	0.3	1.1
Name	**Channel**	**Type**	$u(x_{i,statistical})$	$u(x_{i,exp})$
T301	301	PT-100	0.0	1.0
T302	302	k-type	0.3	1.0
T303	303	k-type	0.3	1.0
T304	304	k-type	0.4	1.1
T305	305	k-type	0.4	1.1
T306	306	k-type	0.4	1.1
T307	307	k-type	0.4	1.1
T308	308	k-type	0.3	1.1
T309	309	k-type	0.3	1.1

Average= **1.1**

C.4   Differential pressure transducer

To measure the differential pressures over the bell mouth, packed pebble bed, manifolds and total pressure a differential pressure transducer was used. The transducer was calibrated against a Betz micro manometer. Calibration was carried out twice to show repeatability and in both instances, the transducer achieved good consistent results. The ambient temperatures was 18 °C and 17.5 °C, with the atmospheric pressures at 100.3769 kPa and 1010.5 kPa. Figure C-3 show the calibration setup for calibrating the pressure transducers.
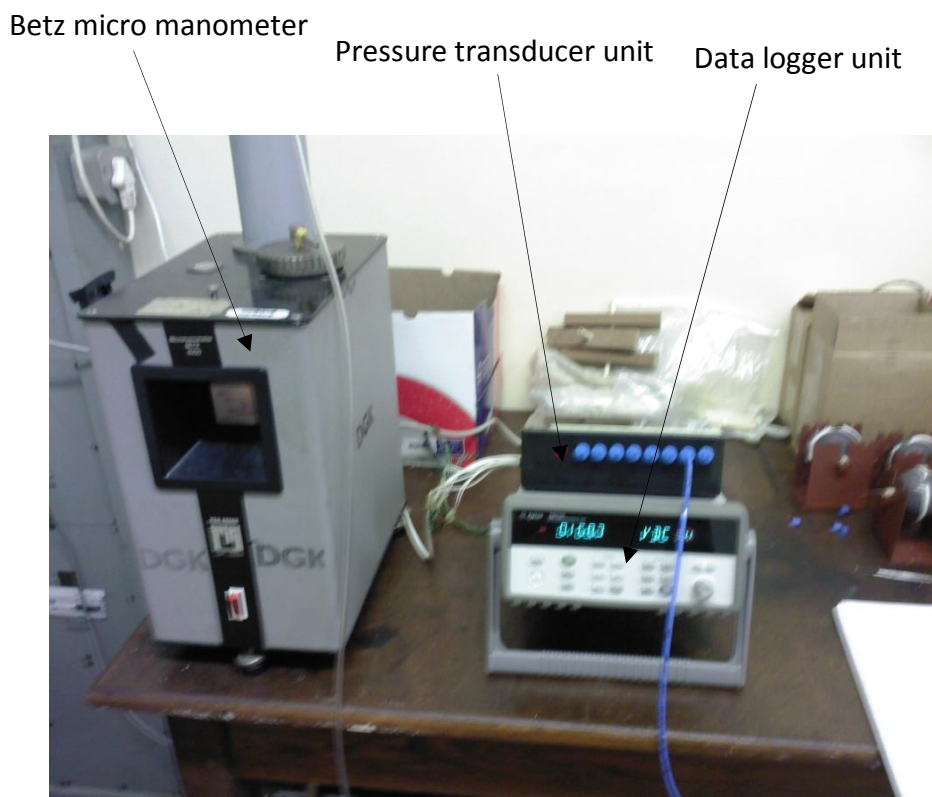
Figure C-3: Calibration setup for pressure transducers

By drawing a vacuum simultaneously in the Betz and the transducer, the voltage was recorded for the specific pressure. Pressure readings were taken at every 1 kPa. This data is available in table C-6.

Table C-7: Calibration data for the differential pressure transducers

Name	Channel	Type	Calibration Set 1					
			Betz (Pa)					
			0.0	1000.0	2000.0	3000.0	4000.0	5000.0
dP1	312	Transducer	0.205 V	0.959 V	1.720 V	2.482 V	3.242 V	4.003 V
dP2	313	Transducer	0.131 V	0.845 V	1.608 V	2.371 V	3.135 V	3.898 V
dP3	310	Transducer	0.171 V	0.918 V	1.680 V	2.442 V	3.204 V	3.967 V
dP4	311	Transducer	0.166 V	0.909 V	1.669 V	2.430 V	3.190 V	3.951 V

Name	Channel	Type	Calibration Set 2					
			Betz (Pa)					
			0.0	1000.0	2000.0	3000.0	4000.0	5000.0
dP1	312	Transducer	0.207 V	0.963 V	1.723 V	2.484 V	3.244 V	4.006 V
dP2	313	Transducer	0.131 V	0.850 V	1.612 V	2.375 V	3.137 V	3.901 V
dP3	310	Transducer	0.172 V	0.920 V	1.682 V	2.444 V	3.206 V	3.969 V
dP4	311	Transducer	0.167 V	0.911 V	1.672 V	2.432 V	3.193 V	3.954 V

Name	Channel	Type	Difference between calibration sets					
			0 Pa	1000 Pa	2000 Pa	3000 Pa	4000 Pa	5000 Pa
dP1	312	Transducer	-0.002 V	-0.004 V	-0.003 V	-0.002 V	-0.002 V	-0.003 V
dP2	313	Transducer	0.000 V	-0.005 V	-0.004 V	-0.004 V	-0.002 V	-0.003 V
dP3	310	Transducer	-0.001 V	-0.002 V	-0.002 V	-0.002 V	-0.002 V	-0.002 V
dP4	311	Transducer	-0.001 V	-0.002 V	-0.003 V	-0.002 V	-0.003 V	-0.003 V

A linear equation was fitted through the data in order to calculate the pressure (Pascal) for any given voltage (Volt). The equations are

$$dp_1 = 1315.8 \times V_1 - 267.32 \tag{C.3}$$

$$dp_2 = 1322.1 \times V_2 - 143.32 \tag{C.4}$$

$$dp_3 = 1315.7 \times V_3 - 216.27 \tag{C.5}$$

$$dp_4 = 1319 \times V_4 - 208.77 \qquad\qquad (C.6)$$

The above equations are then plotted as seen in figure C-4.
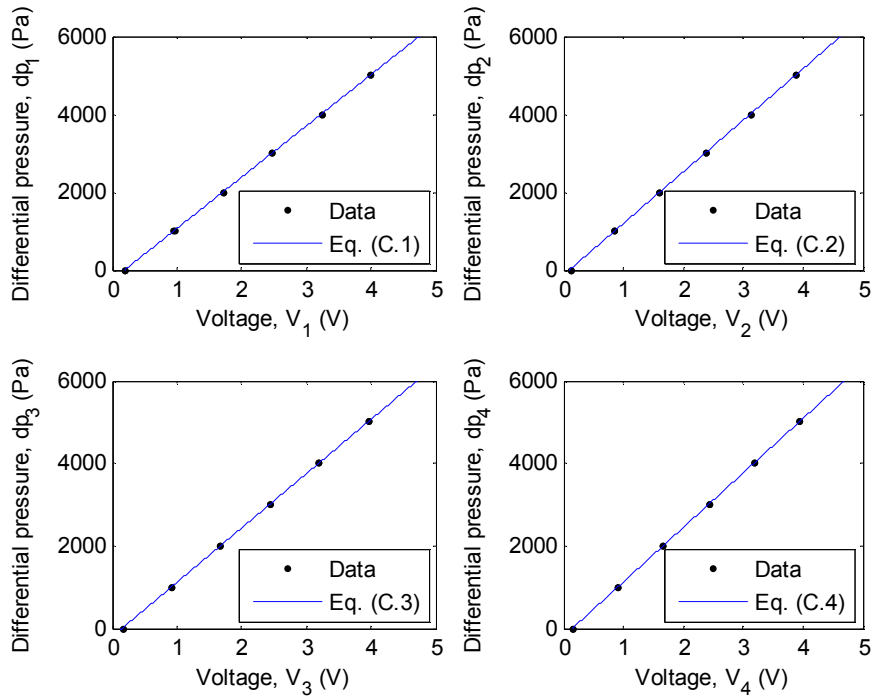
Figure C-4: Linear equations fitted to pressure transducer data

C.5   Bell mouth flow meter

The air mass flow rate that was calculated using the bell mouth flow meter was compared to the air mass flow rate using a pitot tube. There was 5.87 % difference between the two measurements. Throughout the whole project only the bell mouth measurement was used.

Appendix D - Collected data

Data that was taken by means of measurement or logging is given in the following sub-sections.

D.1   Pebble contact area experimental data

In order to determine the contact area between the graphite pebbles, two pebbles was placed on top of each other and pressed until the required force was applied. An imprint of the contact area was recorded on a piece of paper inserted between the pebbles before the experiment. The diameters were measure using a vernier caliper and entered adjacent to the corresponding force used. This data can be seen in table D-1.

Table D-1: Contact area data with applied force between two graphite pebbles

	Applied Force (N)	Contact Diameter (mm)
Data Set 1	205	3.56
	195	3.52
	196	3.38
	205	3.6
	200	3.44
Data Set 2	508	4.6
	491	4.42
	478	4.22
	493	4.42
	455	4.38
Data Set 3	1038	5.2
	1065	5.22
	1055	5.64
	1040	5.48
	1000	5.24
Data Set 4	1450	6.82
	1450	6.48
	1486	6.26
	1365	6.2
	1463	6.24
Data Set 5	2320	7.22
	2368	7.38

	2220	7.46
	2280	7.5
	2300	7.46
Data Set 6	3080	8.48
	2980	8.22
	3100	8.24
	2820	8.1
	2980	8.5
Data Set 7	3980	9.22
	3965	9
	3880	9.16
	3880	9.02
	4090	8.98

The data is displayed in figure D-1. A second order polynomial was also fitted to the data to extrapolate contact diameters at different contact forces. The following equation is obtained:

$$d = -2.57 \times 10^{-7} F^2 + 0.0025117F + 3.1201 \qquad \text{(D.1)}$$
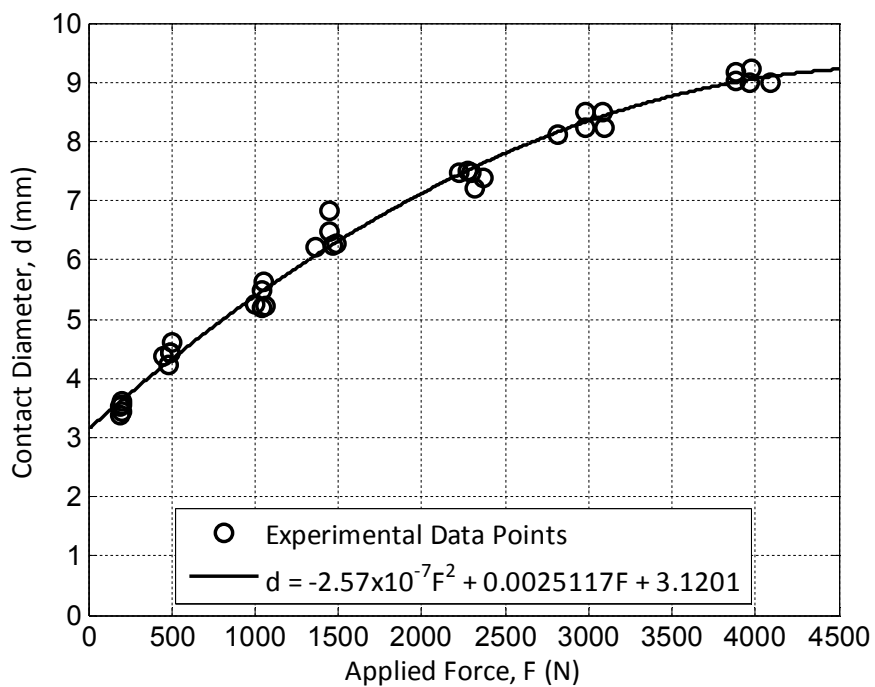
Figure D-1: Applied force and contact diameter data

D.2 Pebble electrical resistances

The pebble electrical resistances were measured to ensure that they are equivalent. A standard bench multimeter was used to measure the resistances. There is a significant improvement between the two sets of pebbles when the variance of the resistance wire is compared. This means that the power dissipated between the pebbles is quite uniform and could be assumed that each pebble dissipates a fraction of the total power consumption. The pebble resistances are listed in table D-2. The variances and averages of the pebbles are listed in table D-3.

Table D-2: Pebble resistances for both sets

PEBBLE RESISTANCES

Pebble set #1	Wire resistance (Ω)	Pebble set #2	Wire resistance (Ω)	Resistance between wire and graphite shell (Ω)	Resistance between wire and thermocouple (Ω)	Resistance between thermocouple and graphite shell (Ω)	Resistance between wire and thermocouple (Ω)	Resistance between thermocouple and graphite shell (Ω)
P1	21.61	P1	33.60	58800.00				
P2	18.45	P2T	31.90	61000.00	90000.00	22600.00		
P3	21.74	P3T	31.30	82200.00	1020000.00	411000.00		
P4	22.22	P4T	30.80	45800.00	50400.00	3100.00		
P5	21.58	P5T	32.20	34200.00	152600.00	66800.00		
P6	18.45	P6T	33.10	40400.00	70900.00	50500.00		
P7	21.49	P7T	32.80	90300.00	1230000.00	4580.00		
P8	18.80	P8T	31.30	29400.00	66900.00	31400.00		
P9	19.13	P9T	33.00	32700.00	150000.00	66500.00		
P10	22.52	P10	33.00	45000.00				
P11	21.99	P11T	32.40	84100.00	1300000.00	1340.00		
P12	21.74	P12	32.30	52200.00				
P13	12.19	P13	31.70	80100.00				
P14	22.12	P14	33.40	106300.00				
P15	21.80	P15	30.30	36800.00				
P16	20.75	P16	31.90	57600.00				
P17	22.12	P17	32.90	115700.00				
P18	21.83	P18T	32.10	41600.00	185800.00	73800.00		
P19	18.63	P19T	33.10	29500.00	141900.00	66800.00		
P20	21.61	P20T	33.70	38000.00	138600.00	57500.00		
P21	6.38	P21TT	31.30	65700.00	169000.00	54500.00	159000.00	51200.00
P22	22.22	P22TT	33.00	38000.00	165000.00	70400.00	171000.00	72000.00
P23	21.74	P23TT	32.70	44500.00	179800.00	67700.00	175800.00	64600.00
P24	22.73	P24TT	32.40	39600.00	132000.00	61600.00	146000.00	63500.00
P25T	19.13	P25	31.80	100800.00				
P26T	18.25	P26	33.10	44700.00				

P27T	18.27	P27	33.00	56700.00
P28T	24.12	P28	32.20	63000.00
P29T	18.23	P29	32.60	17000000.00
P30T	21.80	P30	32.60	19000000.00
P31T	22.59	P31	32.70	78800.00
P32T	21.65	P32	32.80	3600000.00
P33T	22.76	P33	34.30	15000000.00
P34T	20.13	P34	33.00	95800.00
P35T	21.90	P35	33.30	14000000.00
P36T	21.65	P36	32.00	∞
P37T	18.96	P37	32.20	130300.00
P38T	21.43	P38	31.70	111600.00
P39T	22.22	P39	32.70	12600000.00
P40T	22.12	P40	32.00	144700.00
P41T	22.46	P41	33.40	1760000.00
P42T	21.31	P42	32.10	462000.00
P43T	21.87	P43	33.00	∞
P44	18.75	P44	33.90	703000.00
P45	18.52	P45	32.30	59400.00
P46	21.68	P46	32.40	9000000.00
P47	22.49	P47	32.00	105000.00
P48	18.70	P48	33.00	6700000.00
P49	22.90	P49	31.90	3080000.00
P50	22.26	P50	32.40	700000.00
P51	22.03	P51	33.10	2310000.00
P52	21.68	P52	31.90	16000000.00
P53	14.26	P53	33.00	24800.00
P54	15.81	P54	33.00	6000000.00
P55	22.06	P55	32.10	73800.00
P56	22.06	P56	32.20	1490000.00
P57	22.35	P57	32.60	7200000.00
P58	14.68	P58	31.80	13000000.00
P59	22.19	P59	30.80	4800000.00
P60	17.38	P60	31.40	53800.00
P61	22.32	P61	33.80	11000000.00
P62	22.29	P62	29.00	2360000.00
P63	18.38	P63	33.10	1110000.00
P64	21.74	P64	32.20	15000000.00
P65	17.90	P65	31.30	1120000.00
P66	22.16	P66	32.80	8700000.00
P67	21.74	P67	33.60	∞
P68	21.99	P68	32.20	1600000.00
P69	20.49	P69	31.70	7600000.00
P70	20.83	P70	32.10	585000.00
P71	22.35	P71	32.20	12000000.00
P72	21.83	P72	31.80	∞
P73	19.11	P73	33.00	11600000.00
P74	21.87	P74	34.00	10200000.00
P75	21.90	P75	31.50	∞
P76	22.62	P76	33.40	∞
P77	22.19	P77	32.80	8300000.00
P78	21.31	P78	32.40	430000.00
P79	21.80	P79	32.10	13000000.00
P80	21.74	P80	31.90	11500000.00
P81	18.25	P81	31.50	∞
P82	21.77	P82	33.20	10000000.00
P83	17.90	P83	32.20	82000.00
P84	18.68	P84	31.90	11000000.00
P85	22.06	P85	34.60	1870000.00
P86	18.75	P86	32.60	2550000.00
P87	22.22	P87	33.30	5910000.00
P88	22.26	P88	32.20	10800000.00
P89	22.39	P89	32.10	16000000.00
P90	19.40	P90	34.30	9000000.00
P91	22.46	P91	32.70	6500000.00

P92	22.56	P92	35.00	6850000.00
P93	22.03	P93	31.60	2190000.00
P94	19.38	P94	34.60	11300000.00
P95	21.74	P95	34.00	∞
P96	22.06	P96	32.70	4200000.00
P97	21.74	P97	31.00	6800000.00
P98	19.08	P98	31.90	5860000.00
P99	21.31	P99	31.50	5000000.00
P100	22.19	P100	32.70	6200000.00
P101	21.80	P101	32.30	3000000.00
P102	21.87	P102	34.60	∞
P103	18.75	P103	32.00	1200000.00
P104	21.07	P104	33.40	8900000.00
P105	21.68	P105	34.80	∞
P106	21.65	P106	32.50	11300000.00
P107	21.58	P107	32.60	10500000.00
P108	21.19	P108	30.20	8100000.00
P109	22.42	P109	33.10	12300000.00
P110	21.68	P110	35.00	6710000.00
P111	22.03	P111	33.20	9500000.00
P112	21.25	P112	31.80	13600000.00
P113	21.83	P113	32.30	6300000.00
P114	22.09	P114	32.10	10500000.00
P115T	23.70	P115	32.00	13300000.00
P116T	22.73	P116	32.40	2680000.00
P117	22.09	P117	34.00	13000000.00
P118	22.39	P118	32.90	14800000.00
P119	21.65	P119	32.70	∞
P120	21.93	P120	30.10	∞
P121	21.34	P121	32.70	8300000.00
P122	21.19			
P123	22.49			
P124	21.71			
P125	21.46			
P126	21.96			
P127T	15.02			
P128	21.96			
P129	22.03			
P130T	21.19			
P131T	11.63			
P132	0.00			
P133	22.06			
P134	22.52			
P135	22.49			
P136	18.56			
P137	22.69			
P138	22.35			
P139	21.40			
P140	22.06			
P141	21.83			
P142	21.40			
P143	18.75			
P144	17.71			
P145	22.26			
P146	∞			
P147	18.84			

The pebbles still showed signs of earth leakage. The resistance to earth was however larger than in the first set and did not interfere with the pebbles heating performance.

Table D-3: Pebble characteristics of both pebble sets

	Pebble set #1	Pebble set #2
Average wire resistance (Ω)	20.70	32.53
Variance from average wire resistance (%)	42.01	3.07

Appendix E - Codes

The text code or MATLAB (Mathworks, 2009) code that was written to either produce graphs or calculations are given in the following sub-sections.

E.1   Text code used for thermophysical properties

```
;;;;;;;;;;;;;;;;;;;;;;;;;;;;;;;;;;;;;;;;;;;;;;;;;;;;;;;;;;;;;;;;;;;;;;;;;;;
;;;                                                          ;;;
;;;        FLUENT USER DEFINED MATERIAL DATABASE      ;;;
;;;                                                          ;;;
;;; (name type[fluid/solid] (chemical-formula . formula)      ;;;
;;;        (prop1 (method1a . data1a) (method1b . data1b))  ;;;
;;;        (prop2 (method2a . data2a) (method2b . data2b)))  ;;;
;;;                                                          ;;;
;;;;;;;;;;;;;;;;;;;;;;;;;;;;;;;;;;;;;;;;;;;;;;;;;;;;;;;;;;;;;;;;;;;;;;;;;;;

(
        (mixture-template mixture
                (chemical-formula . #f)
                (species (names h2o o2 n2))
                (reactions (finite-rate ("reaction-1" () () ((o2 0 1) (h2o 0 1) (n2 0 1)) (stoichiometry "  ") (arrhenius
1e+15 1e+08 0) (mixing-rate 4 0.5) (specified-rate-exponents? . #t) (use-third-body-efficiencies? . #f))) (finite-rate/eddy-
dissipation ("reaction-1" () () ((o2 0 1) (h2o 0 1) (n2 0 1)) (stoichiometry "  ") (arrhenius 1e+15 100 0) (mixing-rate 4 0.5)
(specified-rate-exponents? . #t) (use-third-body-efficiencies? . #f))) (eddy-dissipation ("reaction-1" () () (o2 0 1) (h2o 0 1)
(n2 0 1)) (stoichiometry "  ") (arrhenius 1e+15 100 0) (mixing-rate 4 0.5) (specified-rate-exponents? . #t) (use-third-body-
efficiencies? . #f))))
        )

        (ceramic solid
                (chemical-formula . #f)
                (density (constant . 1900))
                (specific-heat (constant . 900))
                (thermal-conductivity (constant . 1.8))
                (formation-entropy (constant . 0))
                (electric-conductivity (constant . 0))
                (magnetic-permeability (constant . 0))
                (absorption-coefficient (constant . 0))
                (scattering-coefficient (constant . 0))
                (scattering-phase-function (isotropic . #f))
                (refractive-index (constant . 1))
        )

        (contact solid
                (chemical-formula . #f)
                (density (constant . 1720))
                (specific-heat  (polynomial piecewise-polynomial (300 3200 1576.3 0.79939997 -0.00099312002
6.7985002e-07 -2.5933999e-10 5.1742e-14 -4.2034002e-18)))
                (thermal-conductivity (constant . 128.00513))
                (molecular-weight (constant . 0))
                (absorption-coefficient (constant . 0))
                (scattering-coefficient (constant . 0))
                (scattering-phase-function (isotropic . #f))
                (refractive-index (constant . 1))
        )

        (air fluid
                (chemical-formula . #f)
                (density (ideal-gas . #f) (constant . 1.225))
```

```
                (specific-heat (polynomial piecewise-polynomial (273.14999 2273.1499 1142.9 -1.0841 0.0028762 -
3.0673e-06 1.6993e-09 -4.8170002e-13 5.5202001e-17)) (constant . 1006.43))
                (thermal-conductivity (polynomial piecewise-polynomial (273.14999 2273.1499 0.0010021999
9.0440997e-05 -2.9023999e-08 4.6409998e-12)) (constant . 0.0242))
                (viscosity (polynomial piecewise-polynomial (273.14999 2273.1499 4.2943002e-06 5.3168002e-08 -
1.8708e-11 3.2306e-15)) (constant . 1.7894001e-05) (sutherland 1.716e-05 273.11 110.56) (power-law 1.716e-05 273.11
0.666))
                    (molecular-weight (constant . 28.966))
                    (lennard-jones-length (constant . 3.711))
                    (lennard-jones-energy (constant . 78.6))
                    (thermal-accom-coefficient (constant . 0.9137))
                    (velocity-accom-coefficient (constant . 0.9137))
                    (formation-entropy (constant . 194336))
                    (reference-temperature (constant . 298.15))
                    (critical-pressure (constant . 3758000))
                    (critical-temperature (constant . 132.3))
                    (acentric-factor (constant . 0.033))
                    (critical-volume (constant . 0.002857))
                    (therm-exp-coeff (constant . 0))
                    (speed-of-sound (none . #f))
                    (absorption-coefficient (constant . 0))
                    (scattering-coefficient (constant . 0))
                    (scattering-phase-function (isotropic . #f))
                    (refractive-index (constant . 1))
            )

        (graphite solid
                (chemical-formula . c)
                (density (constant . 1720))
                (specific-heat  (polynomial  piecewise-polynomial  (300  3200  1576.3  0.79939997  -0.00099312002
6.7985002e-07 -2.5933999e-10 5.1742e-14 -4.2034002e-18)) (constant . 1760))
                    (thermal-conductivity (constant . 160))
                    (formation-entropy (constant . 0))
                    (electric-conductivity (constant . 0))
                    (magnetic-permeability (constant . 0))
                    (absorption-coefficient (constant . 0))
                    (scattering-coefficient (constant . 0))
                    (scattering-phase-function (isotropic . #f))
                    (refractive-index (constant . 1))
            )

)
```

E.2   MATLAB Code used for contact area data with applied force between two graphite pebbles

```
% Elbrecht Oswald %
% contact area data with applied force between two graphite pebbles %
% contact diameter versus applied force %
close all;
clear all;
clc;

dataset1 = [0 3.56 3.52 3.38 3.6 3.44;
            0 205 195 196 205 200];
 dataset2 = [4.6 4.42 4.22 4.42 4.38;
             508 491 478 493 455];
 dataset3 = [5.2 5.22 5.64 5.48 5.24;
             1038 1065 1055 1040 1000];
 dataset4 = [6.82 6.48 6.26 6.2 6.24;
```

```matlab
              1450 1450 1486 1365 1463];
dataset5 = [7.22 7.38 7.46 7.5 7.46;
            2320 2368 2220 2280 2300];
dataset6 = [8.48 8.22 8.24 8.1 8.5;
            3080 2980 3100 2820 2980];
dataset7 = [9.22 9 9.16 9.02 8.98;
            3980 3965 3880 3880 4090];
curvedata = [ 3.56 3.52 3.38 3.6 3.44 4.6 4.42 4.22 4.42 4.38 5.2 5.22 5.64 5.48 5.24 6.82 6.48 6.26 6.2 6.24 7.22 7.38 7.46
7.5 7.46 8.48 8.22 8.24 8.1 8.5 9.22 9 9.16 9.02 8.98
              205 195 196 205 200 508 491 478 493 455 1038 1065 1055 1040 1000 1450 1450 1486 1365 1463 2320 2368
2220 2280 2300 3080 2980 3100 2820 2980  3980 3965 3880 3880 4090];
xcurve = 0:1:4500;
curvecoef = polyfit(curvedata(2,:),curvedata(1,:),2);
ycurve = polyval(curvecoef,xcurve);

% % Hertz contact mechanics (wikipedia)
% R1 = 30; %mm
% R2 = 30; %mm
% E1 = 0.12e3; %N/mm^2 % Only properties that can be changed
% E2 = 0.12e3; %N/mm^2 % Only properties that can be changed
% v1 = 0.13; % Only properties that can be changed
% v2 = 0.13; % Only properties that can be changed
% F = 0:1:4500; %N
% R = (1/R1+1/R2)^(-1);
% E_star = ((1-v1^2)/E1+(1-v2^2)/E2)^(-1);
% d = (F/(4/3*E_star*R^(0.5))).^(2/3);
% a_hertz = (R*d).^(0.5);

figure(1)
axes('FontName','calibri','fontsize',12)
plot(curvedata(2,:),curvedata(1,:),'ko','markersize',8,'linewidth',1.5);
hold on;
grid on;
box on;

plot(xcurve,ycurve,'k-','markersize',8,'linewidth',1.5);

%plot(dataset1(2,:),dataset1(1,:),'ko','markersize',8,'linewidth',2);
% plot(dataset2(2,:),dataset2(1,:),'ko','markersize',8,'linewidth',2);
% plot(dataset3(2,:),dataset3(1,:),'ko','markersize',8,'linewidth',2);
% plot(dataset4(2,:),dataset4(1,:),'ko','markersize',8,'linewidth',2);
% plot(dataset5(2,:),dataset5(1,:),'ko','markersize',8,'linewidth',2);
% plot(dataset6(2,:),dataset6(1,:),'ko','markersize',8,'linewidth',2);
% plot(dataset7(2,:),dataset7(1,:),'ko','markersize',8,'linewidth',2);

%a = plot(F,a_hertz,'k-')%

zz = legend('Experimental Data Points','d = -2.57x10^-^7F^2 + 0.0025117F + 3.1201','location','best');
axis([0 4500 0 10]);
aa = ylabel('Contact Diameter, d (mm)');
bb = xlabel('Applied Force, F (N)');
set([zz aa bb],'FontName','calibri','fontsize',12);
```

E.3   MATLAB Code used for mass flow rate calculation for elliptical nozzle

```matlab
% Elbrecht Oswald %
% mass flow rate calculation for elliptical nozzle %
% mass flow rate versus differential pressure %
% Filename: "Mass_Flow_Rate_Elliptical_Nozzle.m"
clear all;
close all;
clc;
```

```matlab
%Dimensional properties of the elliptical nozzle
d = 0.1%m
%Calculate the minimum cross-sectional area of the nozzle
A_n =pi/4*d^2%m^2
%The area upstream of the nozzle is infinitely large, due to it being not enclosed in a wind tunnel
A_tus = inf%m^2
%Measure the atmospheric pressure with the Thies Clima Mercury Station Barometer
p_up = 100709%Pa
%Measure the room temperature with the Thies Clima Mercury Station Barometer
T_rm = 15+273.15%K
%Measure the differential pressure over the nozzle and atmosphere
dp_n = 269%Pa
%Measure the temperature of the air after the nozzle
T_air = 19+273.15%K
%The gas constant for air is
R_air = 287.08%J/kgK
%For air
cp_cv = 1.4
%Knowing the air temperature, the density and dynamic viscosity can be calculated
rho_air = (p_up+dp_n)/(R_air*T_air)%kg/m^3
mu_air = 2.287973e-6 + 6.259793e-8* T_air - 3.131956e-11*T_air^2 + 8.15038e-15*T_air^3%kg/ms
%Calculate the approach velocity factor
Y = 1 + 0.5*(A_n/A_tus)^2 + 2*(A_n/A_tus)^2*dp_n/(p_up*cp_cv)
%Calculate the gas expansion
phi_g = 1 - 3*dp_n/(4*p_up*cp_cv)

%Initial guess for the mass flow rate
m_dot = 0.08
for iterations = 1:6,
    %The Reynolds number can now be calculated
    Re_n =(4*m_dot)/(pi*d*mu_air)
    %The nozzle coefficient of discharge can now be calculated using the Reynolds number
    if 30000 < Re_n < 100000
      C_n = 0.954803 + 6.37817e-7*Re_n - 4.65394e-12*Re_n^2 + 1.33514e-17*Re_n^3
    end
    if 100000 < Re_n < 350000
      C_n = 0.9758 + 1.08e-7*Re_n - 1.6e-13*Re_n^2
    end
    if Re_n > 350000
      C_n = 0.994
    end
    %Revised mass flow rate is
    m_dot = C_n*phi_g*Y*A_n*(2*rho_air*dp_n)^0.5 %kg/s
end

figure(1)
plot(dp_n,m_dot,'rd','markersize',7,'linewidth',2)
axis([0 300 0 0.25])
ylabel('Mass Flow Rate of Air, (kg/s)')
xlabel('Differential Pressure Over Elliptical Nozzle, (Pa)')
title('Mass Flow Rate of Air versus Differential Pressure Over Elliptical Nozzle')
Tstr = num2str(T_air);
str1(1,1) = {'Air Temperature        = '};
str1(1,2) = {Tstr};
str1(1,3) = {'K'};
dpstr = num2str(dp_n);
str1(4,1) = {'Differential Pressure   = '};
str1(4,2) = {dpstr};
str1(4,3) = {'Pa'};
Trmstr = num2str(T_rm);
str1(2,1) = {'Room Temparature      = '};
str1(2,2) = {Trmstr};
str1(2,3) = {'K'};
pastr = num2str(p_up);
```

```
str1(3,1) = {'Atmospheric Pressure = '};
str1(3,2) = {pastr};
str1(3,3) = {'Pa'};
mdotstr = num2str(m_dot);
str1(5,1) = {'Mass Flow Rate of Air = '};
str1(5,2) = {mdotstr};
str1(5,3) = {'kg/s'};
text(10,0.21,str1(:,1))
text(110,0.21,str1(:,2))
text(150,0.21,str1(:,3))
hold on
%Calculating curve
dp_n = 0:1:300;%Pa
for iterations = 1:6,
    %The Reynolds number can now be calculated
    Re_n =(4*m_dot)/(pi*d*mu_air);
    %The nozzle coefficient of discharge can now be calculated using the Reynolds number
    if 30000 < Re_n < 100000
       C_n = 0.954803 + 6.37817e-7*Re_n - 4.65394e-12*Re_n.^2 + 1.33514e-17*Re_n.^3;
    end
    if 100000 < Re_n < 350000
       C_n = 0.9758 + 1.08e-7*Re_n - 1.6e-13*Re_n.^2;
    end
    if Re_n > 350000
       C_n = 0.994;
    end
    %Revised mass flow rate is
    m_dot = C_n.*phi_g.*Y.*A_n.*(2.*rho_air.*dp_n).^0.5; %kg/s
end
plot(dp_n,m_dot)
legend('Working point',4)
```

E.4   MATLAB Code used for differential pressure calculation for packed bed

```
% Elbrecht Oswald %
% pressure drop calculation for packed bed %
% pressure drop versus mass flow rate %
close all;
clear all;
clc;

% atmospheric pressure correction and room temperature %
t = 26; %degC
P = 1005.6; %hPa = mbar
    %Corrections Calculations
    %Cubic expansion coefficient of the mercury
    alfa_Hg = 1.81e-04; %K^-1
    %Linear expansion coefficient of the fixed scale
    alfa_Ms = 0.19e-04; %K^-1
    %Difference in pressure in mbar through influence of temperature
    dP_t = -(alfa_Hg - alfa_Ms)*t*P;
    %The barometer reading corrected to 0 deg in hPa
    if t >= 0
       P_0 = P - abs(dP_t);
    elseif t < 0
       P_0 = P + abs(dP_t);
    end
    %Geographical latitude of the observation point in deg
    rho = -33.92;%deg stellenbosch
    %Difference in pressure hPa as a result of geographical latitude
    dP_rho = -2.56e-03*cosd(2*rho)*P_0;
    %The 0 deg corrected atmospheric pressure corrected to latitude
```

```
        P_0L = P_0 + dP_rho;
        %Elevation above normal zero
        H = 111; %m
        %Difference in pressure in hPa as a result of elevation
        dP_H = -1.96e-07*H*P_0;
        %The 0 deg, latitude corrected atmospheric pressure corrected to elevation
        P_0LE = (P_0L + dP_H)*0.1;
% air temperature flowing out of bellmouth %
T_air_in = 26; %°C
% zero pressure reading %
P_zero = 1.005577; %volt
% system pressure %
PSys = [];
% differential pressure drop over pebbles, [5 10 15 20 25 30 35 40 45 50]% Hz%
dPPeb_Top = [1.005577 1.012415 1.029268 1.062225 1.111137 1.175148 1.255594 1.350207 1.461054
1.586132  1.725527]; %volt
dPPeb_Bot = [1.005577 1.012479 1.029621 1.062857 1.111608 1.176207 1.258194 1.352005 1.465334
1.591964  1.731487]; %volt
% differential pressure drop over bellmouth, [5 10 15 20 25 30 35 40 45 50] Hz%
dPBell = [1.005577 1.006989 1.011184 1.019637 1.032927 1.050744 1.073857 1.101871 1.133897 1.171381
1.211358]; %volt
        % change to pressures %
        % zero correction %
        dPPeb_Top = dPPeb_Top-P_zero+1;
        dPPeb_Bot = dPPeb_Bot-P_zero+1;
        dPBell = dPBell-P_zero+1;
        dPPeb_Top = (1-dPPeb_Top)/(1-2.791)*(0-4980)*-1; % Pa
        dPPeb_Bot = (1-dPPeb_Bot)/(1-2.791)*(0-4980)*-1; % Pa
        dPBell = (1-dPBell)/(1-2.791)*(0-4980)*-1; % Pa
%massflowrate calculation
        %Dimensional properties of the elliptical nozzle
        d = 0.1;%m
        %Calculate the minimum cross-sectional area of the nozzle
        A_n =pi/4*d^2;%m^2
        %The area upstream of the nozzle is infinitely large, due to it being not enclosed in a wind tunnel
        A_tus = inf;%m^2
        %Measure the atmospheric pressure with a Betz manometer
        p_up = P_0LE*1000;%Pa
        %Measure the differential pressure over the nozzle and atmosphere
        dp_n = dPBell;%Pa
        %Measure the temperature of the air after the nozzle
        T_air = T_air_in+273.15;%K
        %The gas constant for air is
        R_air = 287.08;%J/kgK
        %For air
        cp_cv = 1.4;
        %Knowing the air temperature, the density and dynamic viscosity can be calculated
        rho_air = (p_up+dp_n)/(R_air*T_air);%kg/m^3
        mu_air = 2.287973e-6 + 6.259793e-8* T_air - 3.131956e-11*T_air^2 + 8.15038e-15*T_air^3;%kg/ms
        %Calculate the approach velocity factor
        Y = 1 + 0.5*(A_n/A_tus)^2 + 2*(A_n/A_tus)^2*dp_n/(p_up*cp_cv);
        %Calculate the gas expansion
        phi_g = 1 - 3*dp_n/(4*p_up*cp_cv);

        %Initial guess for the mass flow rate
        m_dot = 0.08  ;
        for iterations = 1:5,
            %The Reynolds number can now be calculated
            Re_n =(4*m_dot)/(pi*d*mu_air);
            %The nozzle coefficient of discharge can now be calculated using the Reynolds number
            if 30000 < Re_n < 100000
                C_n = 0.954803 + 6.37817e-7.*Re_n - 4.65394e-12.*Re_n.^2 + 1.33514e-17.*Re_n.^3 ;
            end
            if 100000 < Re_n < 350000
                C_n = 0.9758 + 1.08e-7.*Re_n - 1.6e-13.*Re_n.^2;
```

```matlab
        end
        if Re_n > 350000
            C_n = 0.994;
        end
        %Revised mass flow rate is
        m_dot = C_n.*phi_g.*Y.*A_n.*(2.*rho_air.*dp_n).^0.5; %kg/s
    end;

%Packed bed differential calculations
%Calculated mass flow rate from differential pressure over elliptical nozzle
rho_air = (p_up)/(R_air*T_air);%kg/m^3

m_dot_pb = 0:0.001:0.3;%kg/s
%Bed volume
vol_b = 0.356711*0.315*0.1875%m^3
%Packing volume
vol_p = 0.00001983811*32 + 0.000113097336*112%m^3
%Void fraction
epsilon_v =(vol_b-vol_p)/vol_b
%Specific surface area
a_pb = (0.003015928947*32 + 0.011309733553*112)/vol_b%m^-1
%Cross-sectional area of the bed
A_c = 0.315*0.1875%m^2
%Transfer perimeter
P_pb =  a_pb*A_c;
%Spherical partical diameter
d_p = 6*(1-epsilon_v)/a_pb%m
%Characteristic Velocity
V = m_dot_pb/(rho_air*A_c*epsilon_v)%m/s
%Characteristic Length
L = (d_p*epsilon_v)/(1-epsilon_v)%m
%The Reynolds number can now be calculated
Re_pb = (V*L*rho_air)/mu_air
%Ergun Equation only valid for certain range of Re
if Re_pb <= 10e4
    %Pressure drop across fcc packed bed per length, Ergun
    dp_dx = (150*mu_air*V)/(L.^2) +  (1.75*rho_air*V.^2)/(L)%Pa/m
end
%Length of packed bed
l_pb =0.29755%m
%Pressure drop across fcc packed bed
dp_pb = dp_dx*l_pb%Pa


figure(1)
grid on;
plot(m_dot_pb,dp_pb/1000,'k');

tstr = num2str(t);
str1(1,1) = {'Room Temperature     = '};
str1(1,2) = {tstr};
str1(1,3) = {'°C'};
Pstr = num2str(P_0LE);
str1(2,1) = {'Atmospheric Pressure = '};
str1(2,2) = {Pstr};
str1(2,3) = {'kPa'};
T_air_instr = num2str(T_air_in);
str1(3,1) = {'Inlet Air Temperature   = '};
str1(3,2) = {T_air_instr};
str1(3,3) = {'°C'};
text(0.0045,2.7,str1(:,1))
text(0.105,2.7,str1(:,2))
text(0.145,2.7,str1(:,3))
```

```
axis([0 0.3 0 3])
ylabel('Pressure Drop Across FCC Packed Bed, (kPa)')
xlabel('Mass Flow Rate of Air, (kg/s)')
legend('Ergun Equation, Mills')
```

E.5   MATLAB Code used for correction calculations for Thies Clima Mercury Station Barometer

```
% Elbrecht Oswald %
% correction calculations for Thies Clima Mercury Station Barometer %
% corrected atmosperic pressure and room temperature readings %
% Filename: "Atmospheric_Pressure_Room_Temperature_Corrections.m"
clear all;
close all;
clc;
disp('Room Temperature Reading (°C)= ')
t = 21; %degC
disp(t)
disp('Atmospheric Pressure Reading (bar)= ')
P = 1002.6; %hPa = mbar
disp(P/1000)
%Corrections Calculations
%Cubic expansion coefficient of the mercury
alfa_Hg = 1.81e-04; %K^-1
%Linear expansion coeffiecient of the fixed scale
alfa_Ms = 0.19e-04; %K^-1
%Difference in pressure in mbar through influence of temperature
dP_t = -(alfa_Hg - alfa_Ms)*t*P;
%The barometer reading corrected to 0 deg in hPa
if t >= 0
   P_0 = P - abs(dP_t);
elseif t < 0
   P_0 = P + abs(dP_t);
end
%Geographical latitude of the observation point in deg
rho = -33.92;%deg stellenbosch
%Difference in pressure hPa as a result of geographical latitude
dP_rho = -2.56e-03*cosd(2*rho)*P_0;
%The 0 deg corrected atmospheric pressure corrected to latitude
P_0L = P_0 + dP_rho;
%Elevation above normal zero
H = 111; %m
%Difference in pressure in hPa as a result of elevation
dP_H = -1.96e-07*H*P_0L;
%The 0 deg, latitude corrected atmospheric pressure corrected to elevation
P_0LE = P_0L + dP_H;
%Display corrected atmospheric pressure and room temperature
disp('Atmospheric Pressure Corrected (kPa)= ')
disp(P_0LE*0.1)
```

E.6   MATLAB Code used for calibration and linear fitting of pressure transducers

```
% Elbrecht Oswald %
% calibration and line fitting  for pressure transducers%
% Filename: "Calibration_Pressure_Transducers.m"
```

```matlab
clear all;
close all;
clc;
ddp=[0.0   1000.0 2000.0 3000.0 4000.0 5000.0 0.0 1000.0 2000.0 3000.0 4000.0 5000.0];
dv1=[0.205 0.959  1.720  2.482  3.242  4.003   0.207 0.963  1.723  2.484  3.244  4.006 ];
dv2 = [0.131  0.845  1.608  2.371  3.135  3.898 0.131  0.850  1.612  2.375  3.137  3.901 ];
dv3 =[0.171   0.918  1.680  2.442  3.204  3.967 0.172  0.920  1.682  2.444  3.206  3.969 ];
dv4 =[0.166   0.909  1.669  2.430  3.190  3.951 0.167  0.911  1.672  2.432  3.193  3.954 ];
V1 = 0:0.001:5;
V2 = 0:0.001:5;
V3 = 0:0.001:5;
V4 = 0:0.001:5;
dp1 = 1315.8*V1-267.32
dp2 = 1322.1*V2-143.32
dp3 = 1315.7*V3-216.27
dp4 = 1319.0*V4-208.77
figure(1)
subplot(2,2,1)
plot(dv1,ddp,'k.');
hold on;
plot(V1,dp1,'b-')
legend('Data','Eq. (C.1)',4);
xlabel('Voltage, V_1 (V)');
ylabel('Differential pressure, dp_1 (Pa)');
axis([0 5 0 6000]);
 subplot(2,2,2)
plot(dv2,ddp,'k.');
hold on;
plot(V2,dp2,'b-')
legend('Data','Eq. (C.2)',4);
xlabel('Voltage, V_2 (V)');
ylabel('Differential pressure, dp_2 (Pa)');
axis([0 5 0 6000]);
subplot(2,2,3)
plot(dv3,ddp,'k.');
hold on;
plot(V3,dp3,'b-')
legend('Data','Eq. (C.3)',4);
xlabel('Voltage, V_3 (V)');
ylabel('Differential pressure, dp_3 (Pa)');
 axis([0 5 0 6000]);
subplot(2,2,4)
plot(dv4,ddp,'k.');
hold on;
plot(V4,dp4,'b-')
legend('Data','Eq. (C.4)',4);
xlabel('Voltage, V_4 (V)');
ylabel('Differential pressure, dp_4 (Pa)');
axis([0 5 0 6000]);
```

Appendix F - Operational test procedures

Operational test procedures for the pebble thermal contact area experiment and the pebble bed experiment are given in the next two sub-sections.

F.1   Pebble thermal contact area experiment

A test procedure that was used to form and measure the imprints left by pressing two graphite spheres into each other as explained in section 3.1 is listed below:

- o Insert two graphite pebbles into the wooden box.
- o Place the paper between the two pebbles, ensuring that the pebbles do not leave an indentation on the paper. The pebbles are also rotated between tests so that the force isn't applied to the same area twice.
- o Apply a force and release.
- o Remove the paper from between the two pebbles. The applied force was written on the sample for post processing.
- o Repeat this process for various forces, starting from the smallest force and increasing each time.
- o Measure the area diameter with a micrometer.

F.2   Pebble bed experiment

The start-up, running and shut-down procedures that was used to conduct repeatable and safe experiments as dicussed in section 3.7 is listed below:

Start-up of the experiment:

- o Safety shoes and ear protection must be worn while conducting an experiment.

- Unwind the electrical three phase and single phase leads. Plug them into a wall socket closest to the pebble experiment, and into test apparatus and inverter unit. Make sure that the wall sockets are switched off. Ensure that the leads are lying in a open environment.
- Plug the USB cable running from the Agilent Data Acquisition/Switch Unit, into a Laptop or PC. Be sure to check that the Laptop or PC has the BenchLink Data Logger 3 Program software installed.
- Switch on the single phase lead, thus providing power to the Agilent Data Acquisition/Switch Unit and the pressure transducers. Switch on the Agilent Data Acquisition/Switch Unit, if not already on.
- Open the BenchLink Data Logger 3 Program and run the pebble experiment configuration.
- Make sure that the blower is connected to the inverter unit.
- Switch on the inverter unit at the wall socket.
- Turn the frequency dial to zero and the rotational direction switched to forward. The blower is now ready for use. The frequency can now be selected by turning the speed knob, and monitoring the display. Do not increase the frequency higher than 50 Hz.
- Check that the shut-off valve mounted on top of the pebble experiment is open, to allow air to flow through it.
- Check that the exhaust of the pebble experiment is connected to the specially provided window outlet.
- Close all the doors and windows of the laboratory.
- Open the electrical box on the pebble experiment and make sure that the trip switch (PEBBLE) is switched off (DOWN).
- Switch on the last wall socket, thus switching on the pebble experiment.
- Switch on the GEFRAN 600 CONTROLLER. Check that the power percentage displayed in the lower line of the display is zero.
- Switch the trip switch (PEBBLE) on.

- Wear ear protection.
- Turn the Speed dial on the inverter unit so that the blower runs at 25 Hz.
- Increase the power percentage on the GEFRAN 600 CONTROLLER at a rate of 0.5 %/min until it runs at 100 %.

Running the experiment:

- Start to log the data with the BenchLink Data Logger 3 by pressing play button on the screen.
- Set the power level to the required setting.
- Set the required frequency for the blower.
- Wait for steady state and complete the data form. This can take up to three to four hours.
- Stop logging data and save the data file.
- Start to log the data with the BenchLink Data Logger 3 by pressing play and repeat for different power setting or frequency settings.

A "shut down" procedure is necessary to ensure that the electrically heated graphite pebble's temperature is lowered to a temperature below 50 °C. This procedure will also ensure that the experiment is safely switched off and that the pebbles cool down at a slow and steady rate.

Shut down of the experiment:

- Set the GEFRAN 600 CONTROLLER to supply 0 % power.
- Turn the frequency knob on the frequency inverter unit so that the blower runs at 10 Hz.
- Switch the wall socket of the single phase plugs off, thus turning the Agilent Data Acquisition/Switch Unit and the pressure transducers off.
- Switch the GEFRAN 600 CONTROLLER off.

o When the temperature displayed on the GEFRAN 600 CONTROLLER has reached 50 °C, turn the frequency to zero. Switch off all the wall sockets.

o Wind up all leads and hang then on the pebble experiment, or inverter unit.